The Dissertation Committee for Mukul Bhattacharya certifies that this is the approved version of the following dissertation:

Source properties and population distributions of Fast radio bursts

Committee:

Sonia Paban, Supervisor

Pawan Kumar, Co-Supervisor

Can Kilic

Aaron Zimmerman

Source properties and population distributions of Fast radio bursts

by

Mukul Bhattacharya

DISSERTATION

Presented to the Faculty of the Graduate School of

The University of Texas at Austin

in Partial Fulfillment

of the Requirements

for the Degree of

DOCTOR OF PHILOSOPHY

THE UNIVERSITY OF TEXAS AT AUSTIN

August 2020

Dedicated to my parents and my brother.

Acknowledgments

I would like to thank my advisor, Pawan Kumar, for his invaluable guidance and patience over the past five years. His deep physical insights and amazing ability to simplify seemingly complicated problems into basic physical concepts had a strong impact on my overall development as a graduate student. I am particularly grateful that he provided an open environment within his research group encouraging us to analyse scientific issues critically while always being available to answer our questions. I would thank my co-advisor, Sonia Paban, who has been very supportive and receptive to all my inquiries throughout my graduate studies.

I gratefully acknowledge the time and effort of my research committee members, Can Kilic and Aaron Zimmerman, for giving me valuable feedback on this thesis. I really appreciate their kindness and consideration for understanding the challenging situation at the time of writing this thesis. I would thank Milos Milosavljevic for generously providing all computational resources that were necessary for my research. I would like to extend my gratitude to my undergraduate mentor at the Indian Institute of Science, Banibrata Mukhopadhyay, for always being very kind, supportive and for continuing to believe in me.

I would also like to thank Pawan's former graduate students: Rongfeng Shen, Rodolfo Santana and Patrick Crumley, for their support and advice. My officemates: Aaron Smith, Benny Tsang, Wenbin Lu and Maddie Lucey, have all been very encouraging of my research and provided a lot of scientific insight over the

years. In particular, Benny and Aaron have been really supportive and have always guided me patiently through critical situations. They have often provided me invaluable advice for questions related to Astronomy research, graduate school, postdoctoral applications and everyday life in general.

I am thankful to my fellow Physics classmates: Daniyar Saparov, Jihang Zhu, Avik Roy, Ryota Takaki and Woojoo Lee, who were great to hangout with and discuss about life in graduate school. I would also like to thank my friends at UT who made my PhD experience much more enjoyable: Ashish Gangshettiwar, Ajesh Kumar, Sajal Sen, Harish Potti, Gaurav Chaudhary, Aditya Aravind and Abhranil Das. They were also among my best friends in Austin and were a constant source of support and encouragement. I would like to thank the Astronomy graduate coordinators: Susy Graves, Sandra Catlett, Abby Black and Kalyn Williams, Physics graduate advisor John Keto and graduate coordinator Matthew Ervin for always being there to help and making it easier to navigate through graduate school.

I gratefully acknowledge funding by the Graduate Continuing Fellowship at UT. Finally, and most importantly, I would extend my gratitude to my parents and my elder brother for being unbelievably supportive and encouraging. I cannot thank them enough for their unwavering love, confidence and support throughout this journey. They have been more than understanding of both crisis and celebration during this period. To them, I owe my greatest appreciation and a significant part of my success, however big or small.

Source properties and population distributions of Fast radio bursts

Mukul Bhattacharya, Ph.D.
The University of Texas at Austin, 2020

Supervisors: Sonia Paban & Pawan Kumar

Fast radio bursts (FRBs) are bright millisecond duration transients that are primarily detected from high Galactic latitudes with large dispersion measures which indicates their cosmological origin. Although their observed population has grown rapidly over the past few years, the physical nature of these bursts still remains largely unknown due to the sparse arcminute localisations from current radio transient surveys that hinders their host galaxy identification. Characterising underlying distributions will not just help optimize future searches, but also potentially identify observational sub-classes and provide valuable insights regarding their progenitors, source environment and host galaxy properties.

In this thesis, we investigate the physical properties of FRB sources and further study the binary population classes of these events. First, we discuss a general formalism that we have developed in order to estimate the source properties of FRB progenitors directly from the radio observations. We consider dispersion measure contributions from a Milky Way-type spiral host galaxy, temporal broadening models for pulse propagation through turbulent plasma and a relatively flat FRB energy density spectrum. We then present the results from our Monte Carlo population synthesis code that allows us to directly constrain the properties of

the FRB source, its host galaxy and scattering in the intervening plasma from the current observations. We show that the repeating FRB 121102 is likely to be representative of the entire FRB population based on its energy distribution function and the published FRB follow-up observations at present.

We further extend our analysis to constrain the spatial density of these energetic bursts from their observed flux density distributions. We show that these events most likely originate from a relatively young stellar population which is consistent with the theoretical predictions of the coherent curvature radiation model. Lastly, we discuss the astrophysical implications of future FRB detections including a unified emission mechanism for both non-repeating and repeating FRB population classes, empirical constraints on the source intrinsic variability timescales from observed light curves and the wide-ranging applications of localised FRB sources as cosmological probes and independent distance measures in the near future.

Table of Contents

List of Tables

List of Figures

Chapter 1

Introduction

Fast radio bursts (FRBs) are astrophysical transients with millisecond duration and Jy-level brightness that have been detected in the frequency range ∼0.4-8 GHz (Lorimer et al., 2007; Thornton et al., 2013; Petroff et al., 2016). The physical origin of these bursts is still unknown, primarily due to their short durations and the low angular resolutions of the current radio surveys. The frequency dependence of the arrival time delay ($\propto \nu^{-2}$) and the pulse width evolution ($\propto \nu^{-4}$) of FRBs are both consistent with propagation through cold, turbulent plasma suggesting their astrophysical origin. Currently, about 120 FRB events have already been published (Petroff et al., 2016), with the majority of them not been observed to repeat. There are about 20 FRBs that have been observed to repeat sporadically, with FRB 121102 (Scholz et al., 2016; Spitler et al., 2016) and FRB 180814.J0422+73 (CHIME/FRB Collaboration 2019) being the first two repeating events in that sample.

The cosmological origin of FRBs is strongly suggested by their large dispersion measures (integrated electron column density along the line of sight, DM = $\int n_e dl \sim 10^3$ pc cm^{-3}), which typically exceeds the expected Galactic interstellar medium (ISM) contribution by almost an order of magnitude (Cordes & Lazio 2002). Assuming that most of the excess DM is due to the ionized intergalactic medium (IGM) contribution (Ioka 2003; Inoue 2004), the inferred redshifts are

in the range $z \sim 0.2 - 2$ with a considerably large isotropic energy release of $\sim 10^{38} - 10^{40}$ erg (Thornton et al., 2013; Keane & Petroff 2015; Champion et al., 2016).

The localization of the repeating FRB 121102 within a star-forming region in a dwarf galaxy at redshift z = 0.19273 confirmed the cosmological origin of this particular source (Chatterjee et al., 2017; Marcote et al., 2017; Tendulkar et al., 2017). As more FRB sources get localized in the near future with the upcoming radio surveys, FRBs can be potentially utilised as cosmological probes to study the baryonic distribution within the IGM as well as to constrain the cosmological parameters in our Universe (Gao et al., 2014; Zheng et al., 2014). The ∼ms pulse duration constrains the FRB source size, thereby implying high radio brightness temperatures and coherent emission. Here we provide a brief theoretical introduction of these radio transients.

1.1 Observed FRB properties

The observed FRB population spans a considerably large range in pulse duration, peak flux density and dispersion measure, with the known population of ∼120 independent sources detected by about ∼10 telescopes around the world. Similar to the gamma-ray bursts naming convention, FRBs are also identified with the date when the signal was first recorded as "FRB YYMMDD". FRB 010724, also known as the Lorimer burst, is considered to be the first FRB discovered and was reported from single-pulse searches in the Parkes telescope archival data (Lorimer et al., 2007). The Lorimer burst still remains one of the brightest FRBs to be detected and was estimated to have a peak flux density of 30 Jy and a fluence

of 200 Jy ms (see Figure 1). The large dispersive delay of the pulse is estimated to be about eight times greater than what can be produced by the free electrons within the Milky Way, strongly indicating the extragalactic origin of these bright radio pulses.

The discovery of Thornton bursts at distances as large as 6 Gpc ($z \approx 1$) and with peak flux densities of $\sim$1 Jy implied an isotropic energy output of 10^{39} erg within a few milliseconds (Thornton et al., 2013). Furthermore, these high energy outputs were within a few orders of magnitude of those from GRB prompt emission and supernova explosions, leading to theories of cataclysmic progenitors. Similar to the Lorimer burst, the Thornton bursts also exhibit a clear frequency dependence for the arrival time delay due to dispersion and pulse width broadening due to scattering (see Figure 1). The pulse temporal broadening is found to be consistent with predictions for turbulence in the interstellar medium (ISM) and intergalactic medium (IGM).

Since the first FRB discovery in 2013, the discovery rate has increased every year with the known population almost doubling in the last one year itself (Shannon et al., 2018; CHIME/FRB Collaboration et al., 2019). This has been primarily due to increased searches with the Arecibo Observatory (Spitler et al., 2014), Green Bank Telescope (Masui et al., 2015), Upgraded Molonglo Synthesis Telescope (UTMOST, Caleb et al., 2016), Australian Square Kilometre Array Pathfinder (ASKAP, Bannister et al., 2017; Shannon et al., 2018), and the Canadian Hydrogen Intensity Mapping Experiment (CHIME, CHIME/FRB Collaboration 2019).

The all-sky population of FRBs observed with these highly sensitive telescopes

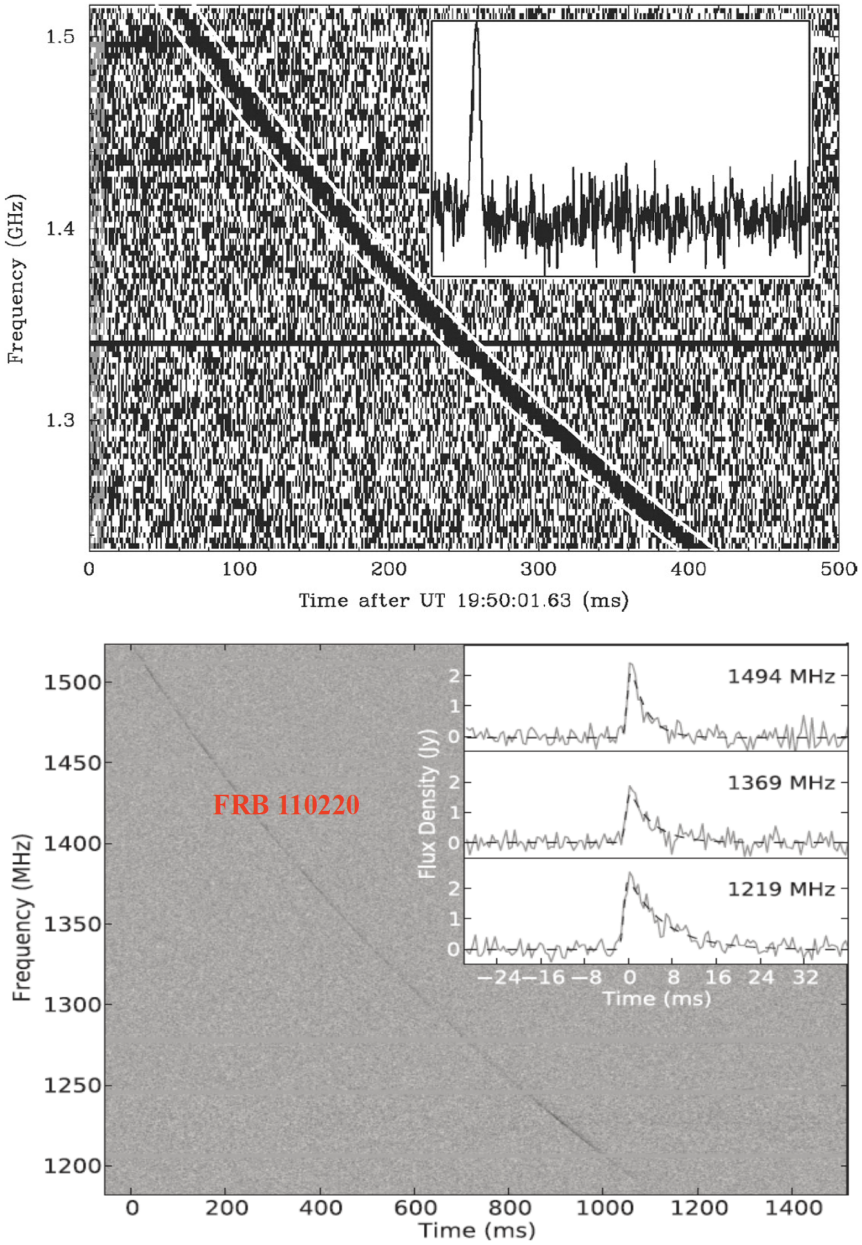

Figure 1.1: *Frequency-time structure of initially detected FRBs 010724 and 110220. Top Panel:* Lorimer FRB 010724 burst sweep due to dispersive time delay in the intervening ionised medium between source and observer. The inset represents pulse profile after correcting for the dispersive delay. Obtained from Lorimer et al. (2007). *Bottom Panel:* The dynamic spectrum of FRB 110220 and its dispersive sweep. The inset shows how the burst becomes asymmetrically broadened towards lower radio frequencies. Obtained from Thornton et al. (2013).

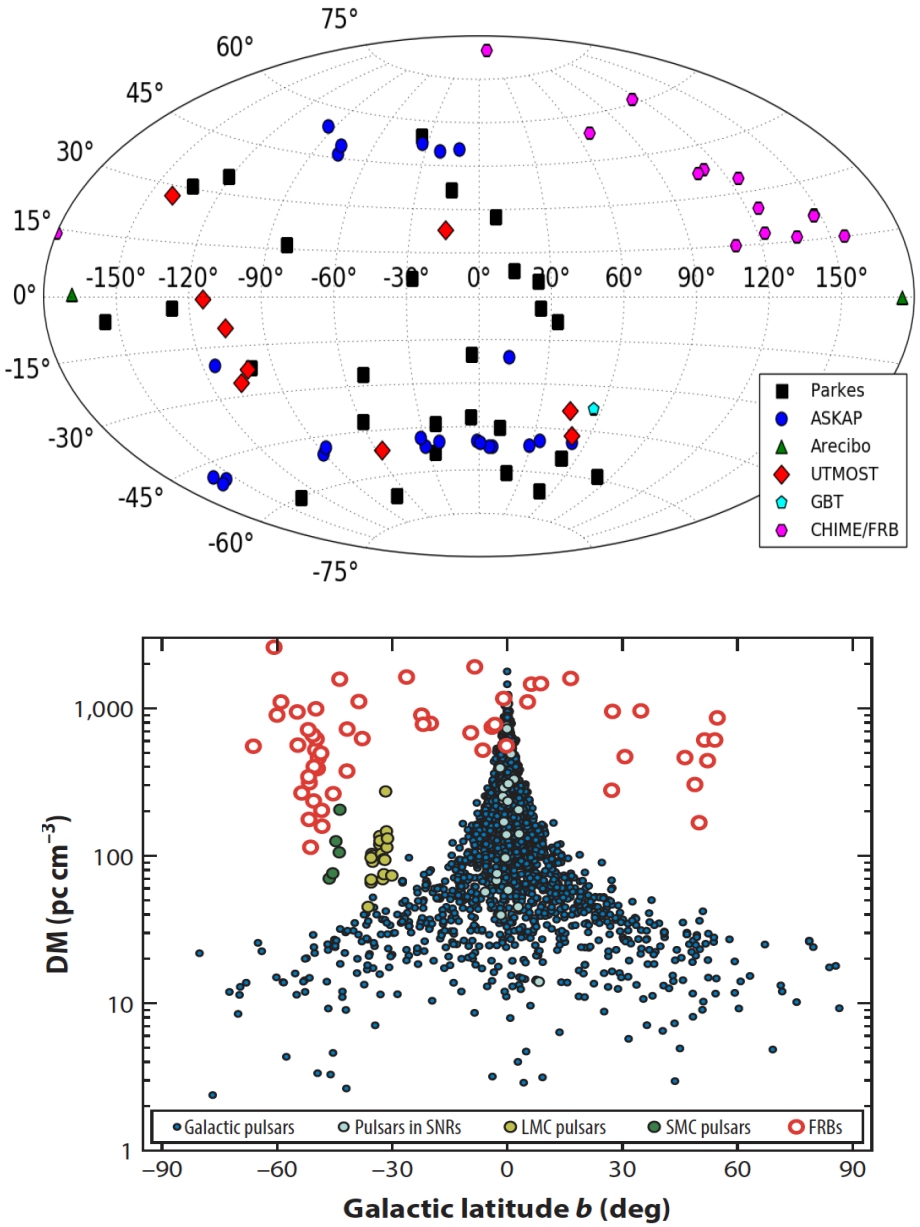

Figure 1.2: *Plot of FRB sky positions and DM as function of Galactic coordinates. Top Panel:* An Aitoff projection map of the sky positions of all published FRBs as a function of Galactic longitude and latitude. As suggested by the figure, there is no preferred line-of-sight in order to detect FRBs. Obtained from Petroff et al (2016). *Bottom Panel:* Dispersion measures plotted against Galactic latitude for pulsars and FRBs. Different symbols are used for Galactic pulsars, Galactic pulsars associated with SNRs, pulsars in the LMC and SMC. Obtained from Cordes et al. (2016).

across the world is found to be fairly isotropic and the observed DM is largely independent of the galactic latitude as opposed to the pulsar populations in the Small Magellanic Cloud, Large Magellanic Cloud and the Milky Way (see Figure 2). This further indicates that these sources are distributed isotropically outside the Milky Way.

1.2 Propagation effects

The observed properties of detected FRBs are directly affected by the propagation effects in the intervening material between the FRB source and observer. The extragalactic FRB signal propagates through (ionised/magnetised/clumpy) material in the direct vicinity of the source, the ISM of its host galaxy, the IGM, and finally through the ISM of our own galaxy before reaching the radio telescopes. As a result, the radio pulses can be absorbed, diffracted, refracted and their polarisation state can also be changed by the intervening material along the line-of-sight.

As with radio pulsars, FRB pulses can also show various propagation effects such as dispersive delay, scattering, scintillation, plasma lensing, Faraday rotation, HI and free-free absorption. Each of these effects carry important information about the local environment of the sources and the galactic hosts of FRBs. Here we focus on the two major propagation effects on the FRB observed pulse which are dispersion and scattering.

As the group velocity of radio waves is frequency dependent in dispersive media such as the ionised ISM and IGM, the higher frequency pulses arrive earlier at the telescope as compared to their lower frequency counterparts. This dispersive

smearing of the observed FRB pulse can be seen as the sweep in the frequency versus time plot (see Figure 1). For a typical FRB $DM = 500$ pc cm^{-3} and observing frequency of 1.4 GHz, this delays the signal by approximately one second compared to infinite frequency.

The ionised intervening medium is also turbulent resulting in temporal broadening of the pulse due to scattering. As the waves get scattered, they take longer path lengths and arrive at a delay to the observer relative to the signal that arrives directly along the line-of-sight. The temporal broadening due to multi-path propagation is seen as an exponential tail scaling strongly with frequency as $\nu^{-4.0}$ in the pulse profiles and can give information about the intervening medium (Figure 1). The pulse scatter broadening in FRBs can be used to study turbulence in the Galactic ISM, IGM, host ISM, and intervening galaxy or galaxy clusters.

1.3 Repeating FRBs & follow-up observations

Although the all-sky isotropic event rate for FRBs above fluence threshold $\sim$1 Jy ms is relatively high $\sim 10^3 - 10^4$ day^{-1} (Thornton et al., 2013; Champion et al., 2016; Rane et al., 2016; Lawrence et al., 2017), most of the previously detected FRBs except FRB 121102 (Scholz et al., 2016; Spitler et al., 2016) and FRB 180814.J0422+73 (CHIME/FRB Collaboration 2019) had not been observed to repeat despite dedicated follow-up searches (Petroff et al., 2015; Ravi et al., 2015; Shannon et al., 2018). This lack of repetition might be due to one of the two possible reasons:

1. two different classes of FRB progenitors (non-repeating and repeating bursts) as suggested by Keane et al. (2016), or

2. observational bias due to the finer localization and higher sensitivity of Arecibo and CHIME telescopes relative to Parkes.

Here we briefly discuss the observed properties of the localised repeating FRBs 121102 and 180814.J0422+73.

FRB 121102: This repeating burst was the first FRB to be detected with a telescope other than Parkes and was reported in a single-pulse search of archival data from the Arecibo PALFA Galactic plane survey (Spitler et al., 2014; Spitler et al., 2016). FRB 121102 is in the Galactic anti-center and has $DM = 557$ pc cm^{-3} which is three times larger than that predicted by the NE2001 model along its line-of-sight (Cordes & Lazio, 2002). The detection of repetition from this source directly signifies that it cannot originate from a cataclysmic event and the phenomena producing these bursts must be able to sustain its activity at least for a period of 8 years, since its discovery in 2012.

The repeating signals made it possible to precisely localise the source using a radio interferometer and study it in greater detail using multi-wavelength measurements (see Figure 3). The FRB 121102 source has been localised to within ~ 0.1 arcsec resolution with the Jansky VLA (Chatterjee et al., 2017) and is found to be associated to a low-metallicity dwarf star-forming host galaxy at z=0.19273 (Tendulkar et al., 2017) with a steady radio source at a separation of $\lesssim 0.01$ arcsec determined with the European VLBI Network (Marcote et al., 2017). As these galaxies are already known to be common hosts of long gamma-ray bursts and superluminous supernovae, it has opened up a possible link between these extreme astrophysical transients and FRBs (Metzger et al., 2017).

FRB 180814.J0422+73: In January 2019, the CHIME/FRB collaboration

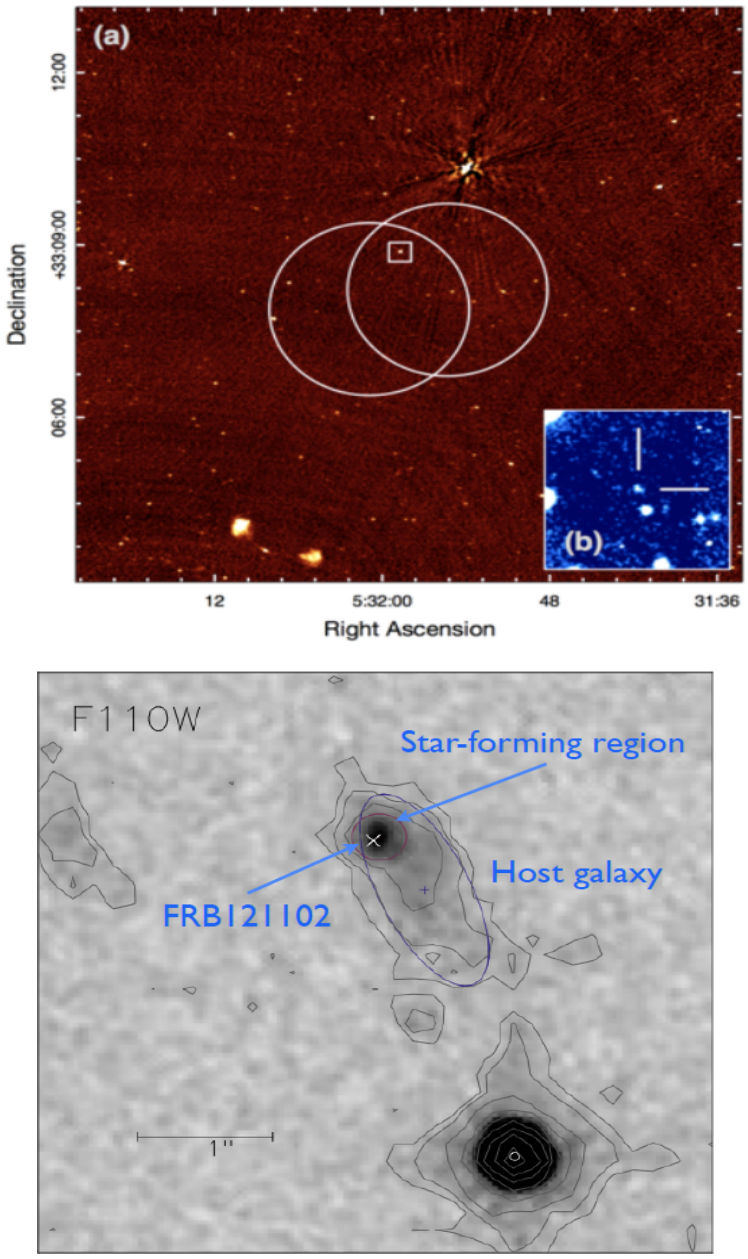

Figure 1.3: *Observations of the dwarf star-forming host galaxy of FRB 121102. Top Panel:* Very Large Array radio image of the field of FRB 121102 where the host galaxy is indicated with a white square and shown at optical wavelengths in the inset. White circles indicate the positional uncertainties of previous Arecibo detections. Obtained from Chatterjee et al. (2017). *Bottom Panel:* Optical image of the FRB 121102 host galaxy obtained with the Hubble Space Telescope. The galaxy is encompassed by a black ellipse and contours show flux levels. The other source visible is a reference star, with its position indicated with a white circle. Obtained from Bassa et al. (2017).

reported the detection of the second repeating FRB. The dispersion measure $DM = 189$ pc cm^{-3} for this repeating burst source, FRB 180814.J0422+73, was found to be significantly lower as compared to the previously detected repeating FRB 121102. Interestingly, many pulses from the FRB 180814.J0422+73 source show multiple sub-bursts with a complex time-frequency structure as seen in the pulses from FRB 121102 (Hessels et al., 2018). The similar time-frequency sub-structures found in some pulses from both repeaters may indicate an origin that is intrinsic to the emission mechanism rather than an extrinsic propagation effect.

While some FRBs have already been followed up for 100-1000 hours since their discovery, others have little to no follow-up observations published in the literature (Shannon et al., 2018). With much fewer repeating FRBs in the observed sample, there is still debate about the potential for repetition from other FRBs. While it has been shown that the repetition rate of FRB 121102 is highly non-Poissonian in nature with periods of high and low activity alternatively (Oppermann et al., 2018), FRB 180814.J0422+73 has not yet been follow-up sufficiently in order to constrain its repetition rate over time.

It is known that FRB 121102 is capable of emitting pulses at a significantly high rate, sometimes $\sim$ few 10s per hour, suggesting that it is clearly more active compared to the other detected sources. While repeating bursts show complex frequency-time substructures, it is possible that similar features might also be present in non-repeating FRBs which can be detected with sufficient temporal and spectral resolution (Farah et al., 2018). The rapid detection of larger number of repeating FRBs with the high-resolution CHIME telescope will make it more clear whether the repeating FRBs come from a different source class or progenitor

channel as compared to the non-repeating events.

1.4 Progenitor models

Even though dozens of published progenitor theories exist, FRBs have not yet been linked to any specific progenitor class (see Platts et al., 2018). In order to differentiate between the proposed progenitor theories, a significantly larger observed sample of FRBs with well characterised burst properties and robustly identified hosts are required. It is important to explore the properties of FRB sources across a broad range of radio frequencies and to continue dedicated searches for multi-wavelength counterparts.

The repeating FRBs provide a practical advantage with regard to detailed characterisation using follow-up observations. Once ASKAP and other high-precision telescopes detect a larger population of FRBs with unambiguous host galaxy associations, the local environment as well as host galaxy features can be probed in more detail and there can be deep searches for associated persistent emission from radio to high-energies.

Several progenitor models, including both cataclysmic and non-cataclysmic scenarios, have been proposed in the FRB literature: collapsing supermassive neutron stars (NSs; Falcke & Rezzolla 2014; Zhang 2014), compact binary mergers (Piro 2012; Kashiyama 2013; Totani 2013), galactic flaring stars (Loeb et al., 2014), radio emission from pulsar companions (Mottez & Zarka 2014), magnetar giant flares (Popov & Postnov 2010; Kulkarni et al., 2014; Lyubarsky 2014; Katz 2016), supergiant pulses from young pulsars (Connor et al., 2016; Cordes & Wasserman 2016; Lyutikov et al., 2016), young rapidly spinning magnetars

(Kashiyama & Murase 2017; Metzger et al., 2017) and plasma stream interacting with NS magnetosphere (Zhang 2017).

The FRB progenitor model should explain the large DMs, ∼ms timescales, ∼Jy brightness and also the very high all-sky events rates. While the discovery of repeating FRBs rules out cataclysmic models for this subset of FRBs, it is possible that repeaters belong to a population of sources that are at a different evolution phase compared to other FRBs. The ∼ms duration pulses constrain the emission region size to be ∼100 km which is similar to neutron stars that can generate coherent emission from small emission regions and also produce large energy outputs similar to observed FRBs.

1.5 Thesis outline

The outline of this thesis is as follows. In Chapter 2, we discuss a general formalism to predict the source properties of non-repeating and repeating FRBs from observables. We estimate the FRB distances and intrinsic widths using appropriate models for IGM/ISM properties, and evaluate the energies and luminosities of these bursts. For our analysis, we have considered a host galaxy DM contribution similar to Milky Way type spiral galaxy, two distinct scattering models to understand pulse temporal broadening and a FRB energy density spectrum which is relatively flat. In Chapter 3, we describe the structure of our Monte Carlo population synthesis code which we use to constrain the properties of the FRB source and its host galaxy. We present the results from simulations that are performed based on specific model distributions of the true properties to study the scattering properties of the intervening IGM and ISM, FRB spatial density as a function of

z, host galaxy DM and the spectral index of the assumed power-law FRB energy density. In Chapter 4, we discuss whether the repeating FRB 121102 is likely to be representative of the entire FRB population based on its repeating behaviour, energy distribution function and the published FRB follow-up data. In Chapter 5, we present our analysis to investigate the spatial density of FRB sources from their observed flux density distributions. Finally, in Chapter 6, we summarise our results and discuss the scope for future work.

Chapter 2

Extracting FRB source properties from observables

In this Chapter, we first estimate the distances to the observed FRBs from their total dispersion measure ($DM_{\rm tot}$) by assuming a fixed DM contribution from the FRB host galaxy ($DM_{\rm host}$). Throughout this analysis, we only consider FRBs with $DM_{\rm tot}$ values exceeding 500 pc cm^{-3} in order to minimize the error in the FRB properties that are based on the FRB distance estimates. The inferred FRB distances are determined by the assumptions about the host galaxy properties and the precise source location inside it, with the error in z expected to be larger for a larger contribution from the relatively uncertain $DM_{\rm host}$ to $DM_{\rm tot}$.

While the $DM_{\rm host}$ contribution to $DM_{\rm tot}$ is generally stochastic with more variability for nearby FRBs, the contributions from the free electrons in the galactic halo to $DM_{\rm host}$ and density inhomogeneities (such as cosmic voids and strong filaments) to $DM_{\rm IGM}$ are both expected to be small. We then obtain the intrinsic pulse widths ($w_{\rm int}$) from the observed FRB widths ($w_{\rm obs}$) using scattering models for the pulse temporal broadening due to the multipath propagation through the ionized ISM and IGM. The burst luminosities and energies are calculated for a flat energy spectrum from the peak flux density, distance and the frequency range for FRB radio emission. We also estimate the error in the inferred parameters due to the various assumptions involved in our models.

Table 2.1: Observed and inferred parameters for non-repeating FRBs published until February 2019 that have total DM in excess of 500 pc cm^{-3}. We use a DM cutoff to minimize the error in the estimation of inferred FRB parameters due to the host galaxy DM assumption. For each reported FRB, we select the observation with largest signal-to-noise ratio from Petroff et al. (2016). We also exclude the FRBs with unresolved intrinsic widths from our analysis (see equation 2.3). The definitions of all burst parameters are discussed in the text.

FRB	Telescope	$S_{\rm peak,obs}$ (Jy)	$DM_{\rm tot}$ (pc cm^{-3})	z	$L_{\rm int1/2}$ (10^{44} erg/s)	$w_{\rm obs}$ (ms)	$w_{\rm int1/2}$ (ms)
010125	Parkes	0.54	790.3	0.82	2.00/2.00	10.6	4.06/4.05
010621	Parkes	0.53	748.0	0.20	0.11/0.11	8.0	2.93/2.93
090625	Parkes	1.14	899.55	1.06	7.17/7.31	1.92	0.73/0.71
110220	Parkes	1.11	944.38	1.12	6.35/6.35	6.59	3.06/3.05
110523	GBT	0.60	623.30	0.69	1.34/2.70	1.73	0.77/0.38
110626	Parkes	0.63	723.0	0.81	2.16/2.21	1.41	0.58/0.56
110703	Parkes	0.45	1103.6	1.33	4.20/4.23	3.90	1.55/1.53
120127	Parkes	0.62	553.3	0.61	0.97/0.98	1.21	0.60/0.60
121002	Parkes	0.43	1629.18	2.00	11.19/11.23	5.44	1.66/1.61
130626	Parkes	0.74	952.4	1.09	5.01/5.11	1.98	0.74/0.71
130729	Parkes	0.22	861	1.01	0.97/0.97	15.61	7.73/7.73
131104	Parkes	1.16	779	0.85	3.70/3.72	2.37	1.15/1.15
140514	Parkes	0.47	562.7	0.62	0.63/0.63	2.82	1.68/1.68
150215	Parkes	0.70	1105.6	0.82	2.08/2.09	2.88	1.37/1.37
151230	Parkes	0.42	960.4	1.13	2.63/2.64	4.4	1.98/1.97
160317	UTMOST	3.0	1165	1.03	14.58/14.65	21.0	9.82/9.76
160608	UTMOST	4.3	682	0.51	3.79/3.80	9.0	5.40/5.39
170107	ASKAP	22.3	609.5	0.68	163.88/171.71	2.6	0.34/0.33
170416	ASKAP	19.4	523.2	0.56	22.06/22.07	5.0	2.86/2.86
170428	ASKAP	7.7	991.7	1.17	96.79/98.14	4.4	1.02/1.00
171116	ASKAP	19.6	618.5	0.69	60.58/60.93	3.2	1.04/1.04
180110	ASKAP	128.1	715.7	0.82	964.88/988.45	3.2	0.61/0.60
180131	ASKAP	22.2	657.7	0.74	56.54/56.64	4.5	2.03/2.02

2.1 Distance estimate

The total DM for any FRB has contributions from the IGM ($DM_{\rm IGM}$), the Milky Way (MW) ISM ($DM_{\rm MW}$) and the host galaxy ISM. Including the cosmological expansion factor for the host galaxy contribution gives

$$DM_{\rm tot} = DM_{\rm IGM} + DM_{\rm MW} + \frac{DM_{\rm host}}{(1+z)}. \tag{2.1}$$

The IGM contribution increases with the source redshift as (Ioka 2003; Inoue 2004; Deng & Zhang 2014)

$$\begin{aligned} DM_{\rm IGM} &= \frac{c}{H_0}\int_0^z \frac{f_{\rm IGM} n_{\rm e}(z') x(z') dz'}{(1+z')^2[\Omega_{\rm m}(1+z')^3+\Omega_\Lambda]^{0.5}} \\ &= (1294.9 \text{ pc cm}^{-3}) \int_0^z \frac{(1+z')dz'}{\sqrt{(1+z')^3+2.7}} \end{aligned} \tag{2.2}$$

where $f_{\rm IGM} = 0.83$ is the fraction of baryon mass in the IGM, $n_e(z) = 2.1 \times 10^{-7}(1+z)^3$ cm^{-3} is the number density of free electrons, $x(z) \approx 7/8$ is the ionization fraction with cosmological parameters as $H_0 = 68$ km s^{-1}Mpc^{-1}, $\Omega_{\rm m} = 0.27$ and $\Omega_\Lambda = 0.73$ (Planck Collaboration et al., 2014).

The DM contribution from the Galactic ISM along the FRB source line of sight is obtained from the NE2001 model (Cordes & Lazio 2002). The host galaxy DM contribution depends on the type of the galaxy, location of the FRB source within the galaxy as well as our viewing angle relative to the galaxy. Although the host galaxy for the repeating FRB 121102 has been identified to be a dwarf star-forming galaxy (Tendulkar et al. 2017), there is still no information about the host galaxies for the other sources.

Due to the uncertainties associated with the host galaxy properties and the FRB source location inside them, here we assume that the host galaxy has a free

electron density distribution similar to that of the MW with a typical contribution of $DM_{\rm host} \approx 100$ pc cm^{-3}. With the values of $DM_{\rm tot}$, $DM_{\rm MW}$ and $DM_{\rm host}$ known, we solve for the redshifts of the non-repeating bursts from equation (5.1). As the host galaxy for the repeating FRB 121102 is localized at z=0.19273 (Tendulkar et al. 2017), the $DM_{\rm IGM}$ value is precisely known and equation (5.1) further gives $DM_{\rm host} \approx 281$ pc cm^{-3}. Once z is estimated, the comoving distance to the source is obtained as $D(z) = (8.49\ {\rm Gpc}) \int_0^z [(1+z')^3+2.7]^{-0.5} dz'$ with a luminosity distance $D_L(z) = (1+z)D(z)$.

2.2 Intrinsic width estimate

The intrinsic width of a cosmological FRB source is broadened due to both propagation and telescope effects. Excluding the pulse broadening components from the observed width gives

$$w_{\rm int}^2 = \frac{w_{\rm obs}^2 - (w_{\rm DM}^2 + w_{\rm samp}^2 + w_{\rm IGM}^2 + w_{\rm ISM,MW}^2)}{(1+z)^2} - w_{\rm ISM,host}^2 \qquad (2.3)$$

where, $w_{\rm DM} = 8.3 \times 10^6 (DM_{\rm tot}\, \Delta\nu/\nu_0^3)$ ms, is the dispersive smearing across single frequency channels with $\Delta\nu$ and ν_0 being the channel bandwidth and the central frequency of observation in MHz, respectively. While $w_{\rm samp}$ is the sampling time of the observation, $w_{\rm IGM}/w_{\rm ISM,MW}/w_{\rm ISM,host}$ denotes the pulse temporal broadening due to scattering in the IGM/MW ISM/host galaxy ISM and $(1+z)$ is the cosmic expansion factor.

It should be noted that the distribution of the pulse observed/intrinsic width $w_{\rm obs/int}$ is directly affected by the temporal resolution of the telescope/survey used. While most of the non-repeating FRBs listed in Table 6.1 were detected with Parkes at a fine resolution of ~ 0.1 ms, the other events detected by GBT,

UTMOST and ASKAP were at a coarse temporal resolution of ~ 1.0 ms. In our analysis here, we include the instrument time resolution $\sim w_{\rm samp}$ for each burst while computing $w_{\rm int}$ from $w_{\rm obs}$ using equation (2.3) and discuss the associated bias $\Delta w_{\rm int}$ later in this section. While a telescope with a coarse time resolution is less likely to detect a pulse with a relatively small $w_{\rm obs}$ due to the associated instrumental noise, there will also be an effective observing bias against the events with fairly large $w_{\rm obs}$ as the sensitivity reduces gradually. While Shannon et al. (2018) have shown that the luminosity distributions for the Parkes FRBs at finer resolution and ASKAP FRBs at coarser resolution are fairly similar, the observing bias tends to select more events at relatively smaller distances.

As the radio pulses propagate through the ionised plasma in the intervening IGM and ISM, they are scattered due to the inhomogeneities in the electron density along the line of sight resulting in multipath propagation and thereby scatter broadening. The reported scattering timescales are significantly larger compared to the scattering timescales expected from the Galactic turbulence along such lines of sight and it is expected that most of the scattering is predominantly due to the IGM (Williamson 1972; Macquart & Koay 2013).

Due to the absence of sufficient information on the FRB scattering timescales, we consider two separate models to evaluate the ISM and IGM scattering broadening timescales for each FRB as discussed below.

1. *Scattering model 1:* We assume that the temporal broadening $w_{\rm ISM,host/MW}$ due to scattering in the host galaxy/MW ISM is related to $DM_{\rm host/MW}$ as

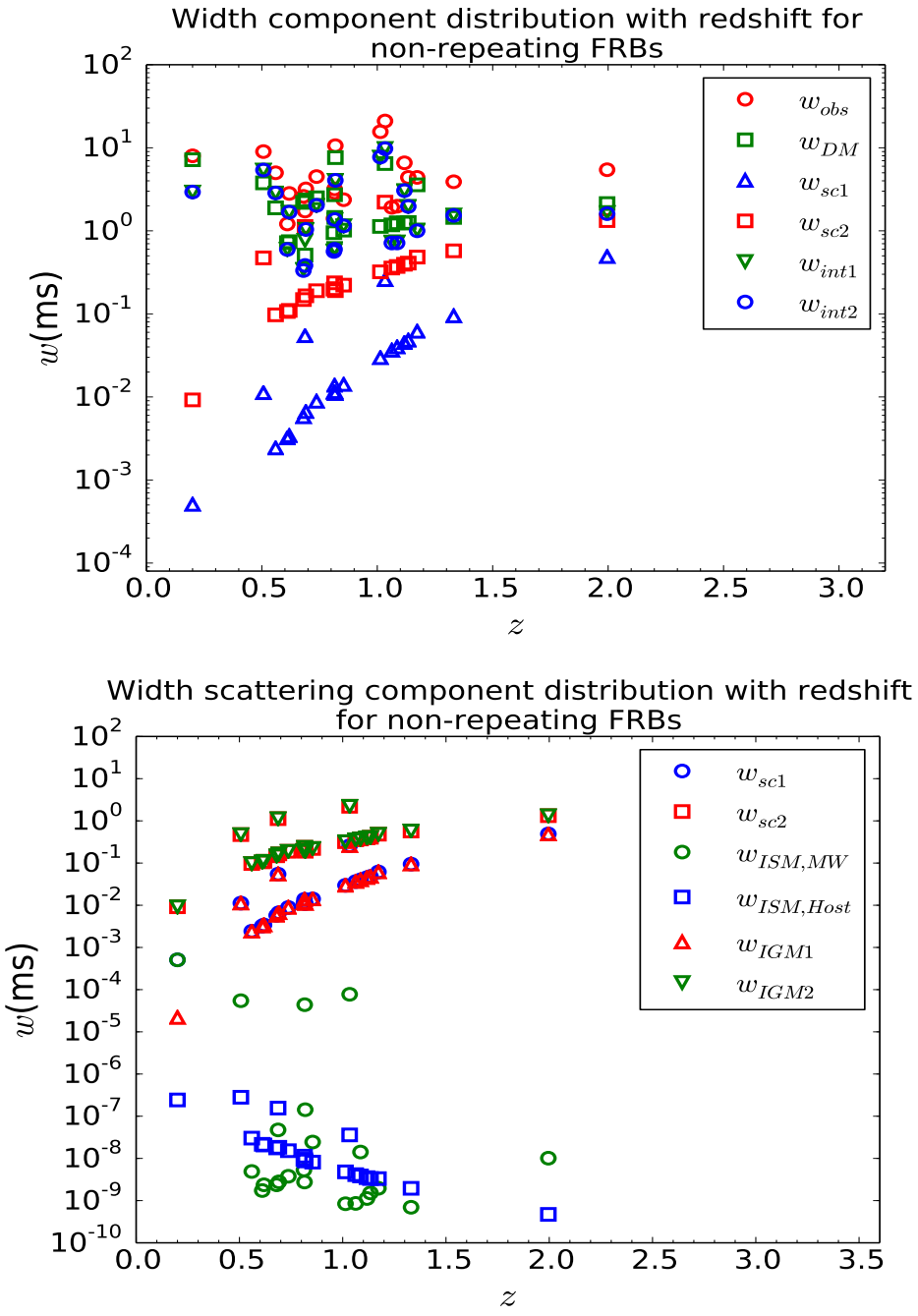

Figure 2.1: *Variation of pulse width components for non-repeating FRBs: Top panel:* Variation of observed width $w_{\rm obs}$ components: $w_{\rm DM}$, $w_{\rm sc}$ and $w_{\rm int}$, with distance for non-repeating FRBs, *Bottom panel:* Variation of scattering width $w_{\rm sc}$ components: $w_{\rm ISM,host}$, $w_{\rm ISM,MW}$ and $w_{\rm IGM}$, with distance for non-repeating FRBs.

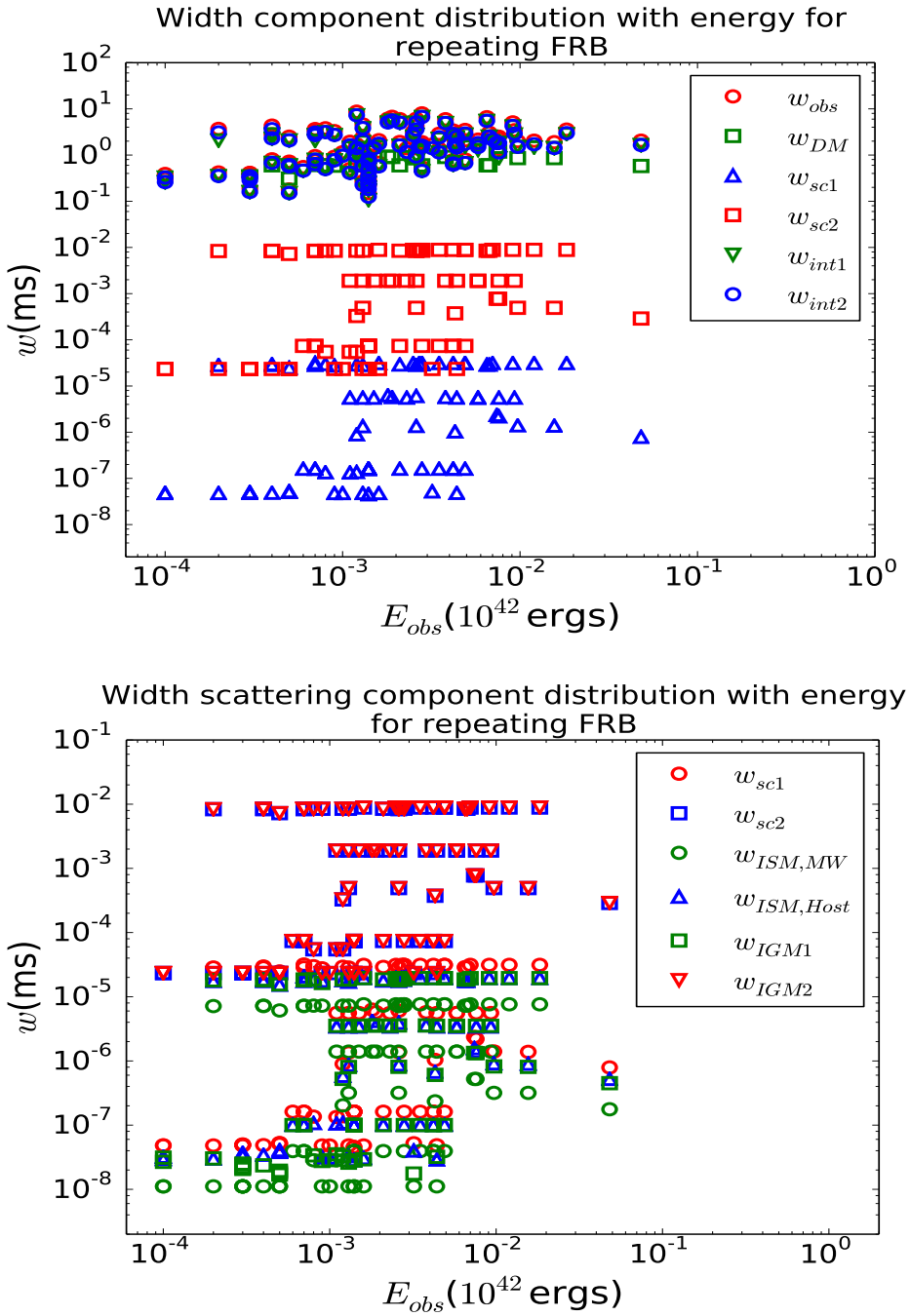

Figure 2.2: *Variation of pulse width components for repeating FRB 121102: Top panel:* Variation of observed width $w_{\rm obs}$ components with burst energy for FRB 121102 sub-bursts, *Bottom panel:* Variation of scattering width $w_{\rm sc}$ components with burst energy for FRB 121102 sub-bursts.

given by the empirical fit obtained by Krishnakumar et al. (2014),

$$w_{\rm ISM,host/MW} = (41\ {\rm ns})\ 4f(1-f)(1.00 + 1.94\times10^{-3} DM^{2.0}_{\rm host/MW})\frac{DM^{2.2}_{\rm host/MW}}{\nu^{4.4}_{0,\rm GHz}} \quad (2.4)$$

where $\nu_{0,\rm GHz} = \nu_0/10^3$ is the central frequency in GHz and $4f(1-f)$ is the lever-arm factor by which $w_{\rm ISM,host/MW}$ is suppressed. We use $f = 25$ kpc$/D_L$, where D_L is the luminosity distance (in kpc) from the source to the observer and 25 kpc is the typical extent of a MW-like galaxy. Although most of the scattering material is present in the ISM of the host galaxy or the MW, their contribution to scatter broadening is expected to be significantly suppressed by a factor $4f(1-f) \sim 10^{-4}$ due to the asymmetric placement of the scattering screens relative to the source and the observer (Williamson 1972; Vandenberg 1976; Lorimer et al., 2013).

As the average electron density fluctuations in the IGM are expected to be less significant compared to the ISM, we assume that the scatter broadening due to IGM can be obtained by rescaling the ISM contribution by three orders of magnitude (Lorimer et al., 2013; Caleb et al., 2016),

$$w_{\rm IGM} = (4.1\times10^{-11}\ {\rm ms})\ (1.00 + 1.94\times10^{-3} DM^{2.0}_{\rm IGM})\frac{DM^{2.2}_{\rm IGM}}{\nu^{4.4}_{0,\rm GHz}}. \quad (2.5)$$

As opposed to the host galaxy/MW ISM scattering, IGM scattering is unaffected by geometrical effects such as the lever-arm effect.

2. *Scattering model 2:* In this model, we assume that the ISM scatter broadening contribution from the host galaxy and the MW are still given by the $w_{\rm ISM} - DM$ relation in equation (5.2). However, instead of rescaling

$w_{\rm ISM,host/MW}$ to obtain $w_{\rm IGM}$, we use the theoretical temporal smearing expression for IGM turbulence as obtained by (Macquart & Koay 2013),

$$w_{\rm IGM}(z) = \frac{k_{\rm IGM}}{\nu_{0,\rm GHz}^4 Z_L} \int_0^z \frac{dz'}{\left[\Omega_m(1+z')^3+\Omega_\Lambda\right]^{0.5}} \int_0^z \frac{(1+z')^3}{\left[\Omega_m(1+z')^3+\Omega_\Lambda\right]^{0.5}} dz \quad (2.6)$$

where $Z_L = 1 + (1/2)z$ and $k_{\rm IGM}$ is the normalisation factor (see Appendix A for a detailed derivation of equation 5.3). We fix the value of $k_{\rm IGM} = 7.35 \times 10^{11}$ ms MHz^4 from equation (2.3) such that

$$w_{\rm int} \leq \sqrt{w_{\rm obs}^2 - (w_{\rm DM}^2 + w_{\rm samp}^2 + w_{\rm IGM}^2)}/(1+z),$$

is a real quantity for all the resolved FRBs in Table 6.1.

While $w_{\rm IGM}$ from model 1 is based on the assumption that the nature of IGM turbulence is similar to that of the Galactic ISM and can be estimated with an observationally established empirical fit, $w_{\rm IGM}$ from model 2 is based on a completely theoretical model for IGM turbulence which has not been observationally verified. Previous FRB population studies (Bera et al., 2016; Caleb et al., 2016) have used $w_{\rm ISM} - DM$ relation for pulsars in the MW ISM from Bhat et al. (2004) in order to estimate the IGM and ISM scatter broadening widths. However, it has already been shown by (Hassall et al., 2013; Lorimer et al., 2013) that the scatter broadening of known FRBs is significantly smaller compared to that estimated from the Bhat et al. (2004) model.

The pulse scattering width estimated from the Bhat et al. (2004) model increases considerably beyond $z \sim 0.5$ (see Figure 1 of Bera et al., 2016) and typically exceeds the observed pulse widths for the known FRBs at high redshifts (see Table 6.1). For $DM_{\rm host/MW} \lesssim 100$ pc cm$^{-3} \ll DM_{\rm IGM}$, $w_{\rm ISM,host/MW}$ obtained

from equation (5.2) is considerably smaller compared to $w_{\rm IGM}$ and other width components in equation (2.3). The values of all the observed burst and telescope parameters in equations (5.1-5.3) are obtained from Petroff et al. (2016).

The modelled scatter broadening width for a given FRB source can be written as, $w_{\rm sc} = [w^2_{\rm ISM,MW} + w^2_{\rm ISM,host}(1+z)^2 + w^2_{\rm IGM}]^{0.5}$. For non-repeating FRBs, we show the variation of the observed width components $w_{\rm DM}$, $w_{\rm sc}$ and $w_{\rm int}$ with distance in the top panel of Figure 2.1, while the variation of the scattering width components $w_{\rm ISM,host}$, $w_{\rm ISM,MW}$ and $w_{\rm IGM}$ with distance are shown in the bottom panel of Figure 2.1. The ISM broadening contributions obtained from the scattering models are found to be very small with $w_{\rm ISM,MW} \lesssim 10^{-3}$ ms and $w_{\rm ISM,host} \lesssim 10^{-6}$ ms, which is expected as the ISM contribution is suppressed relative to the IGM contribution by the geometrical factor $4f(1-f) \sim 10^{-4}$. While the width broadening due to IGM turbulence is larger at least by an order of magnitude for scattering model 2 at smaller redshifts $z \lesssim 1$, the IGM contributions for both scattering models are roughly equal for $z \gtrsim 2$ as $w_{\rm IGM}$ increases faster with distance for model 1.

The dispersive smearing $w_{\rm DM}$ is approximately of the same order of magnitude as $w_{\rm obs}$ and $w_{\rm int}$ for a given FRB, with 10^{-1} ms $\lesssim w_{\rm DM} \lesssim 10^{1}$ ms for all bursts. The smallest contribution to the pulse width broadening is from scattering with $w_{\rm sc} \lesssim 1$ ms for almost all bursts. As $w_{\rm obs} \sim w_{\rm DM} \gg w_{\rm sc}$ for most FRBs, $w_{\rm DM}$ is the dominant contribution to the temporal broadening. Even though the intrinsic pulse width varies considerably with 10^{-1} ms $\lesssim w_{\rm int} \lesssim 10$ ms, the two scattering models are essentially indistinguishable due to the small scatter broadening contributions with $w_{\rm int,1} \approx w_{\rm int,2}$.

The top panel of Figure 2.2 shows the variation of $w_{\rm obs}$ components with

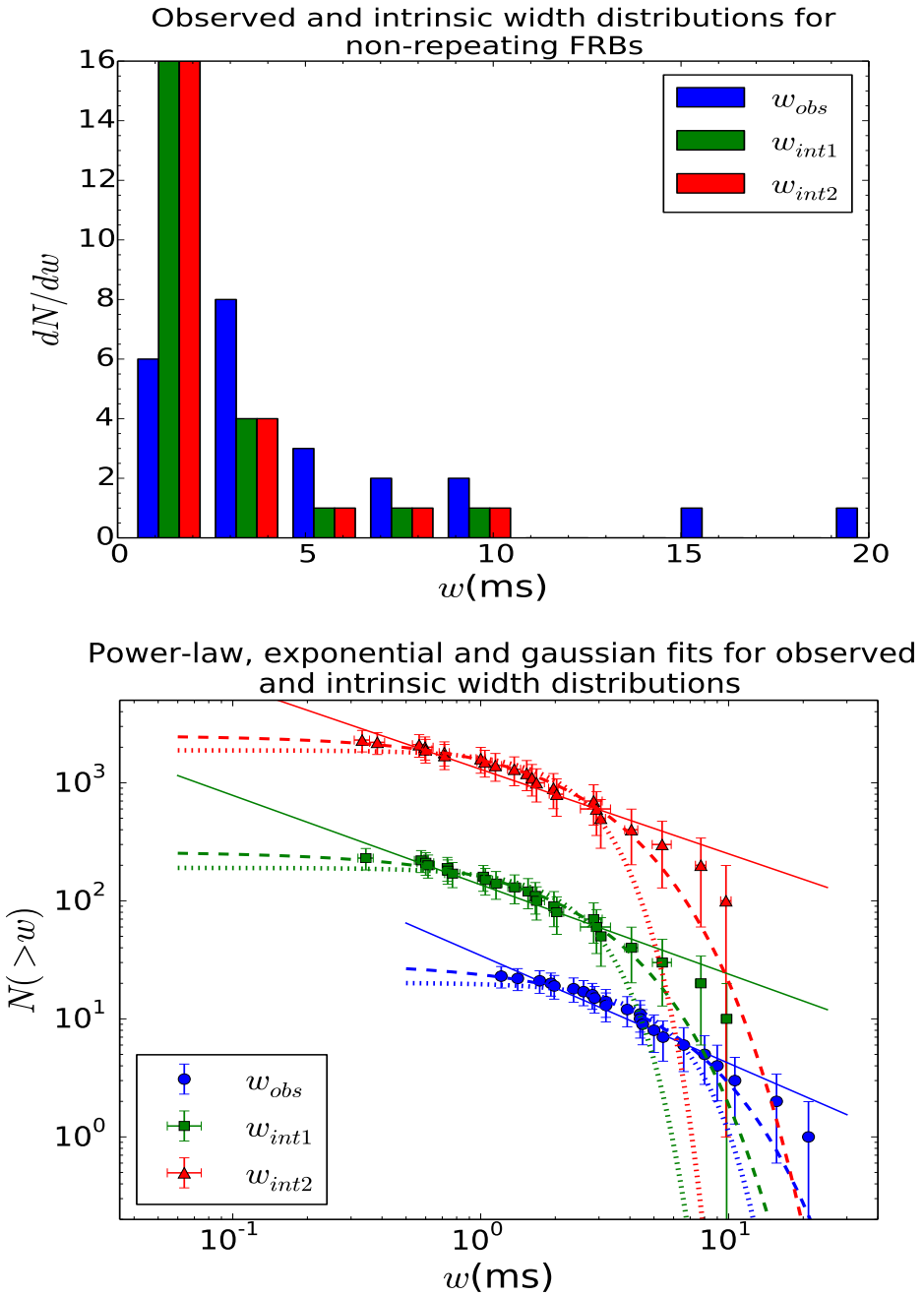

Figure 2.3: *Pulse width distribution for non-repeating bursts: Top panel:* Histograms for widths $w_{\rm obs}$, $w_{\rm int1}$ and $w_{\rm int2}$, *Bottom panel:* Chi-squared fits for cumulative distributions of $w_{\rm obs}$, $w_{\rm int1}$ and $w_{\rm int2}$. The index 1/2 for the burst parameters denotes scattering model 1/2. The functional forms used for the chi-squared fits of the cumulative width distributions are power-law, exponential and gaussian (see Table B.1).

$E_{\rm obs}$, while the bottom panel shows the variation of $w_{\rm sc}$ components with the emitted energy for the sub-bursts of FRB 121102. It should be noted that many intrinsically shorter FRB 121102 sub-bursts have been detected due to high time-resolution systems such as the Breakthrough Listen observations at 4-8 GHz with GBT (Gajjar et al. 2018). Similar to the non-repeating FRBs, the sub-bursts of FRB 121102 were also detected by instruments with time-resolution varying over a wide range: ~ 0.1 ms for Arecibo and Effelsberg to ~ 1.0 ms for GBT. This affects the distributions of the true properties for FRB 121102 sub-bursts such as $w_{\rm int}$ and $L_{\rm int}$. We compute $w_{\rm int}$ for sub-bursts from a given survey by including the associated time resolution $\sim w_{\rm samp}$ along with the uncertainty. However, we do not consider the effect of different sensitivity thresholds for different searches of FRB 121102 in our simplistic study here.

We find that the modelled ISM broadening contributions from both host galaxy and MW are very small with $w_{\rm ISM,host/MW} \lesssim 10^{-4}$ ms for all sub-bursts. As the redshift $z \approx 0.19273$ is relatively small for FRB 121102, the width broadening due to IGM turbulence is much more significant for scattering model 2 relative to model 1. The dispersive smearing is found to be smaller compared to most non-repeating FRBs with 10^{-1} ms $\lesssim w_{\rm DM} \lesssim 1$ ms. While $w_{\rm obs}$ and $w_{\rm int}$ are approximately of the same order of magnitude, $w_{\rm DM}$ is about one order of magnitude smaller. We find that scatter broadening $w_{\rm sc} \lesssim 2 \times 10^{-2}$ ms is the smallest contribution to the width broadening.

Even though $w_{\rm DM}$ is the dominant contribution to the pulse broadening with $w_{\rm obs} > w_{\rm DM} \gg w_{\rm sc}$, $w_{\rm DM}$ for FRB 121102 sub-bursts are considerably smaller compared to that for the non-repeating FRBs due to the relatively small $DM_{\rm tot}$ for

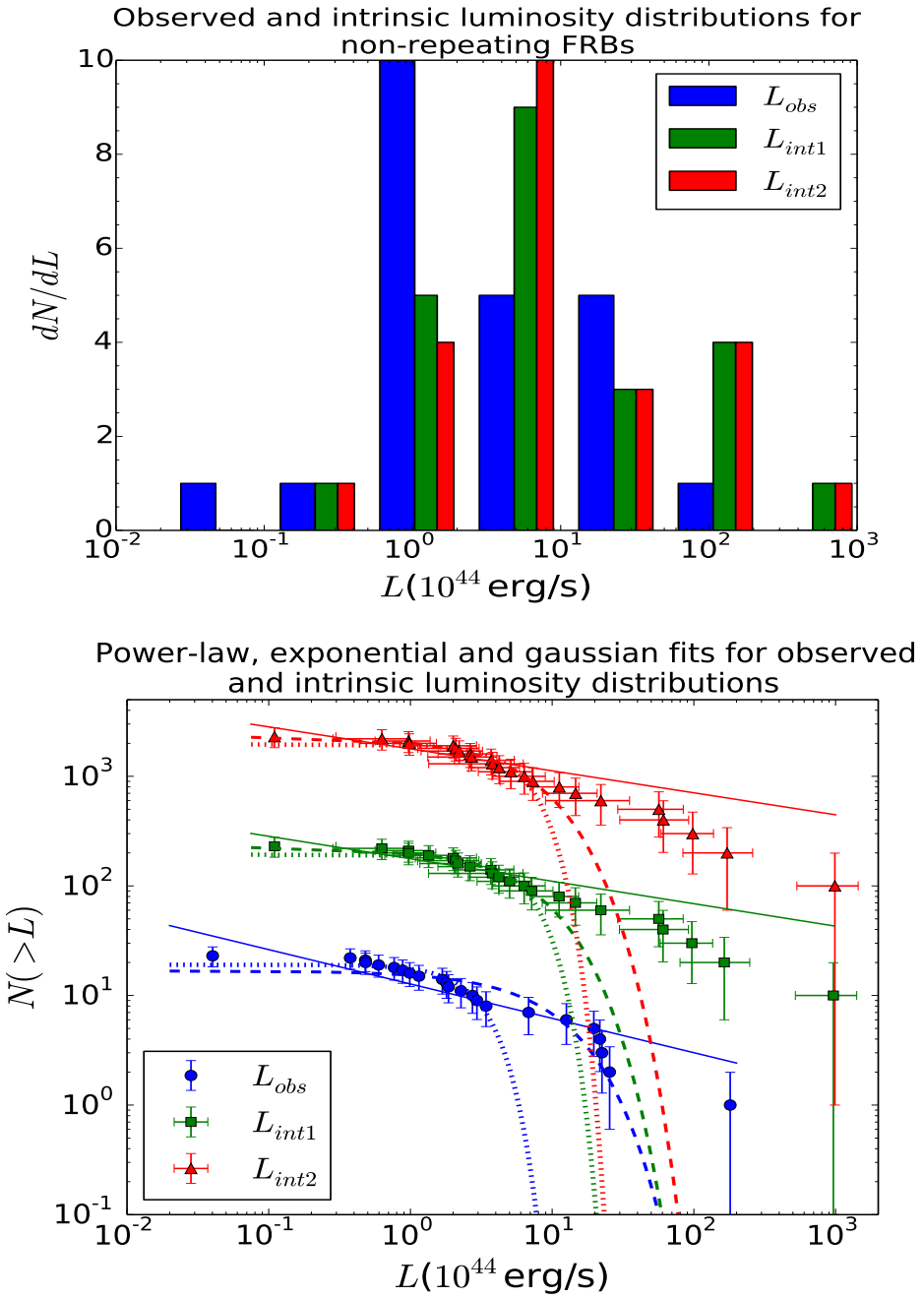

Figure 2.4: *Luminosity distributions for non-repeating bursts: Top panel:* Histograms of luminosities $L_{\rm obs}$, $L_{\rm int1}$ and $L_{\rm int2}$, *Bottom panel:* Chi-squared fits for cumulative distributions of $L_{\rm obs}$, $L_{\rm int1}$ and $L_{\rm int2}$. The index 1/2 for the burst parameters denotes scattering model 1/2. The functional forms used for the chi-squared fits of the cumulative luminosity distributions are power-law, exponential and gaussian (see Table B.1).

FRB 121102. The intrinsic width varies considerably within 1 ms $\lesssim w_{\rm int} \lesssim$ 10 ms with $w_{\rm int} \approx w_{\rm obs}$, implying that a considerable fraction of $w_{\rm obs}$ for FRB 121102 is from $w_{\rm int}$ and not due to the dispersive smearing or scatter broadening of the pulse. Although $w_{\rm sc1} \ll w_{\rm sc2}$, the scattering models are still indistinguishable with $w_{\rm int,1} \approx w_{\rm int,2}$ due to the minimal IGM and ISM scatter broadening contributions.

For both non-repeating bursts and FRB 121102, we find that most of the pulse temporal broadening is due to dispersive smearing and not IGM or ISM scattering. The contribution from $w_{\rm DM}$ to the width broadening is found to be considerably larger for the non-repeating FRBs in comparison to the FRB 121102 sub-bursts, which is expected due to the larger $DM_{\rm tot}$ values for the non-repeating FRBs. While the variation in $w_{\rm DM}$ for a given z is only due to a combination of different observation frequencies $\Delta\nu$ and ν_0 across various telescopes for the repeating FRB 121102 (top panel of Figure 2.2), different galactic contributions $DM_{\rm host/MW}$ also play a major role in determining the magnitude of $w_{\rm DM}$ for the non-repeating FRBs (top panel of Figure 2.1). The IGM pulse broadening obtained from scattering models is the dominant contribution to $w_{\rm sc}$ for both classes of FRBs while the $w_{\rm ISM}$ contributions are significantly smaller due to the geometrical lever-arm effect.

The intrinsic width for both FRB classes is found to be largely scattering model-independent. Moreover, there is a considerable spread in the $w_{\rm int}$ values within a range of $\sim$ 10 ms/$\sim$ 8 ms for the non-repeating/repeating bursts with most FRBs having $w_{\rm int} \lesssim$ 5 ms/$w_{\rm int} \lesssim$ 3 ms. We estimate the average relative broadening of the intrinsic width, $\Delta w_{\rm int}/w_{\rm int} = (w_{\rm obs} - w_{\rm int})/w_{\rm int}$, to be $\sim 150\%/\sim 20\%$ for the non-repeating/repeating FRBs. It should be noted that larger $w_{\rm obs}$ corresponds to a lower instrument sensitivity, thereby resulting in a observing bias

against bursts that are smeared over longer duration and/or have larger intrinsic width.

2.3 Luminosity and energy estimates

As the width of a radio pulse gets broadened by scattering in the turbulent plasma, the pulse is smeared across a longer time interval, thereby reducing its peak flux density. The fluence $\mathcal{F}_{\rm obs}$, proportional to the total emitted energy of the pulse, is assumed to be unaffected by the scatter broadening for each burst. Once $w_{\rm int}$ for a given FRB is obtained from equation (2.3), the corresponding intrinsic peak flux density can be estimated from the fluence as $S_{\rm peak,int} = \mathcal{F}_{\rm obs}/w_{\rm int}$. For a power-law energy distribution of the FRB source, the bolometric luminosity and energy for the burst are given by Lorimer et al. (2013),

$$L = \frac{4\pi D^2(z)(\nu'^{\alpha+1}_{\rm max} - \nu'^{\alpha+1}_{\rm min})(\nu_2 - \nu_1)}{(1+z)^{\alpha-1}(\nu_2^{\alpha+1} - \nu_1^{\alpha+1})} S_{\rm peak}$$
$$E = \frac{4\pi D^2(z)(\nu'^{\alpha+1}_{\rm max} - \nu'^{\alpha+1}_{\rm min})(\nu_2 - \nu_1)}{(1+z)^{\alpha-1}(\nu_2^{\alpha+1} - \nu_1^{\alpha+1})} \mathcal{F}_{\rm obs} \qquad (2.7)$$

where $\nu'_{\rm min/max}$ is the minimum/maximum source emission frequency in the FRB comoving frame, α is the spectral index and $\nu_{1/2}$ is the lowest/highest frequency in the observing band of the telescope. In order to evaluate the intrinsic luminosity and energy distributions for the observed bursts, we assume a flat energy spectrum ($\alpha \approx 0$) to obtain: $L_{\rm int} = 4\pi S_{\rm peak,int} D^2(z)(\nu'_{\rm max} - \nu'_{\rm min})(1+z)$ and $E_{\rm obs} = 4\pi \mathcal{F}_{\rm obs} D^2(z)(\nu'_{\rm max} - \nu'_{\rm min})(1+z)$. Here we use $\nu'_{\rm min} = 600$ MHz and $\nu'_{\rm max} = 8$ GHz that are consistent with the current observed FRB population (Petroff et al., 2016). The assumption of a flat energy spectrum is reasonable as the FRB emission spectrum is poorly constrained at present with the spectral indices varying within a wide range.

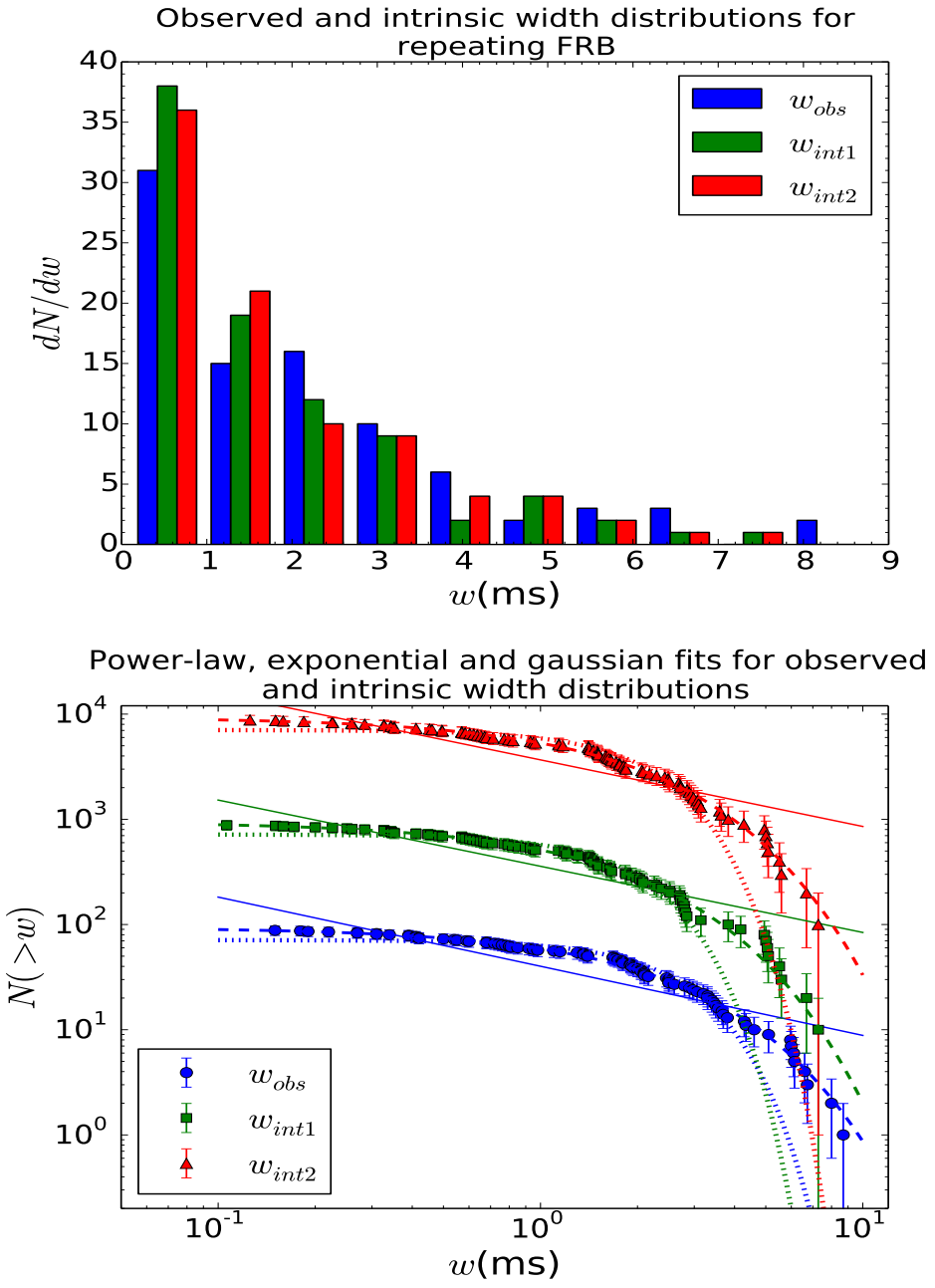

Figure 2.5: *Pulse width distributions for repeating bursts: Top panel:* Histograms for widths $w_{\rm obs}$, $w_{\rm int1}$ and $w_{\rm int2}$, *Bottom panel:* Chi-squared fits for cumulative distributions of $w_{\rm obs}$, $w_{\rm int1}$ and $w_{\rm int2}$. The index 1/2 for the burst parameters denotes scattering model 1/2. The functional forms used for the chi-squared fits of the cumulative width distributions are power-law, exponential and gaussian (see Table B.2).

The top panels in Figures 2.3 and 2.4 show the histograms for the distributions of pulse width and luminosity of the 23 non-repeating bursts from Table 6.1, while the bottom panels show three functional fits for the cumulative distributions of the corresponding quantities. We obtain chi-squared fits for the cumulative distributions of the non-repeating burst parameters using three different functional forms: power-law, exponential and gaussian with zero mean, where the error for each data point is quantified with Poisson fluctuations (see Table B.1 in Appendix B for the parameter details). We find that $w_{\rm int}$ for most bursts is a factor of $\sim 2-3$ smaller compared to $w_{\rm obs}$ and is within a relatively broad range of $\sim 0.3-10$ ms. While most of the bursts have $w_{\rm int} \lesssim 5$ ms, there is considerable spread in the width values suggesting that they are not peaked around $w_{\rm int} \approx 1$ ms as assumed for previous MC simulations (Bera et al., 2016); Caleb et al., 2016).

We find that the cumulative distribution of $w_{\rm int}$ for non-repeating bursts is best fitted with an exponential distribution, with a cutoff around $w_{\rm int} \sim 2$ ms that is about half of the $w_{\rm obs}$ exponential cutoff. $L_{\rm int}$ varies by almost four orders of magnitude from $\sim 10^{43}$ erg/s to $\sim 10^{47}$ erg/s with a peak luminosity around $\sim 4 \times 10^{44}$ erg/s. As the inferred $L_{\rm int}$ values of the observed non-repeating bursts vary within a wide range, FRBs are significantly unlikely to be standard candles. We find that the cumulative distribution of $L_{\rm int}$ is best fitted with an exponential distribution for the non-repeating bursts, with a $L_{\rm int}$ cutoff around $\sim 8 \times 10^{44}$ erg/s. Furthermore, there is no significant difference in the width and luminosity distribution fit parameters obtained by changing the scattering models.

The top panels in Figures 2.5 and 2.6 show the histograms for the width and luminosity distributions of the repeating FRB 121102 sub-bursts obtained

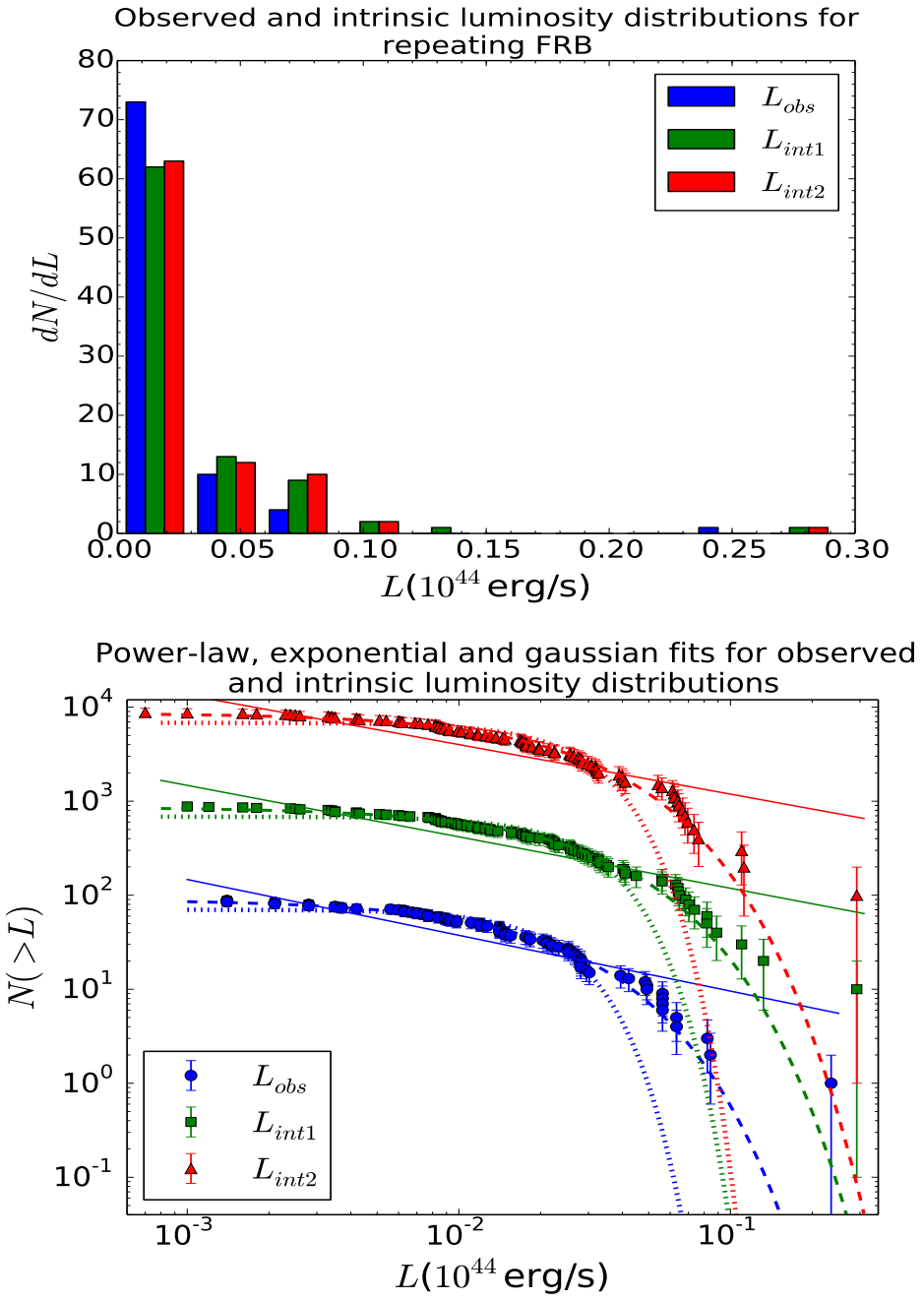

Figure 2.6: *Luminosity distributions for repeating bursts: Top panel:* Histograms of luminosities $L_{\rm obs}$, $L_{\rm int1}$ and $L_{\rm int2}$, *Bottom panel:* Chi-squared fits for cumulative distributions of $L_{\rm obs}$, $L_{\rm int1}$ and $L_{\rm int2}$. The index 1/2 for the burst parameters denotes scattering model 1/2. The functional forms used for the chi-squared fits of the cumulative luminosity distributions are power-law, exponential and gaussian (see Table B.2).

from Spitler et al. (2016), Scholz et al. (2016), Scholz et al. (2017), Law et al. (2017), Hardy et al. (2017), Michilli et al. (2018), Gajjar et al. (2018) and Spitler et al. (2018). The bottom panels show the chi-squared fits (with the same functional forms as the non-repeating bursts) for the cumulative width and luminosity distributions, with the parameter details listed in Table B.2 of Appendix B.

Even though the average $w_{\rm int}$ for repeating burst is smaller compared to that for the non-repeating bursts, it still varies by almost two orders of magnitude from $\sim 0.1 - 8$ ms with most bursts having $w_{\rm int} \lesssim 3$ ms. The fractional pulse broadening $\Delta w_{\rm int}/w_{\rm int} = (w_{\rm obs} - w_{\rm int})/w_{\rm int}$ for the repeater is also found to be smaller compared to the non-repeating bursts, which is expected due to its smaller distance, and thereby lesser scatter and dispersion broadening.

The cumulative $w_{\rm int}$ distribution is best fitted with an exponential distribution with a cutoff $w_{\rm int} \sim 1.6$ ms that is slightly smaller than the corresponding cutoff for $w_{\rm obs} \sim 2.1$ ms. The luminosity varies in a considerably smaller range, $L_{\rm int} \sim 10^{41} - 10^{43}$ erg/s, compared to the non-repeater bursts. We find that the cumulative $L_{\rm int}$ distribution is best fitted with an exponential distribution, with a cutoff $L_{\rm int} \sim 2.7 \times 10^{42}$ erg/s that is slightly larger compared to the $L_{\rm obs}$ cutoff. Similar to the non-repeating bursts, the difference between the scattering models is almost negligible and can be ignored.

2.4 Parameter correlation for FRB sources

Once the burst parameters are estimated from the FRB observables, we can study the correlation between different parameters and the burst distance/energy

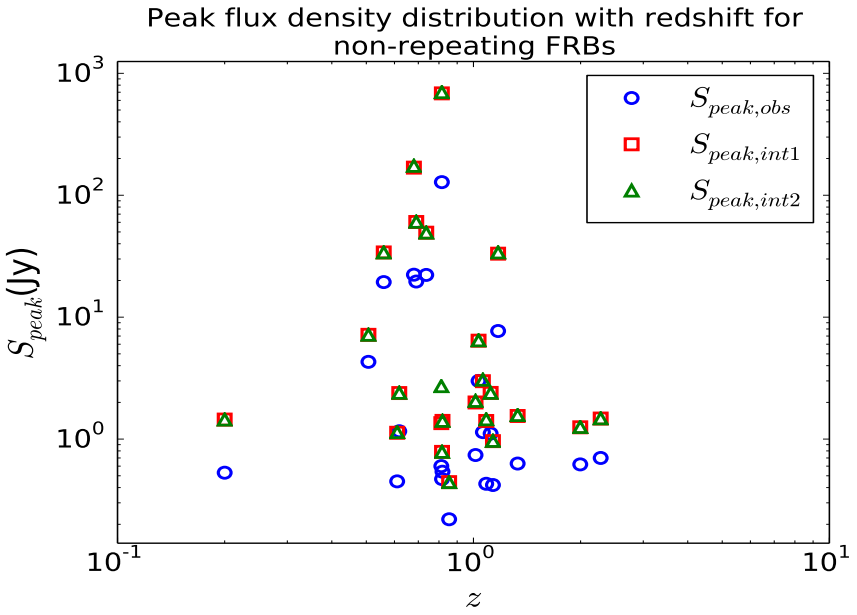

Figure 2.7: Plot of peak flux densities $S_{\rm peak}$ with distance for non-repeating FRBs.

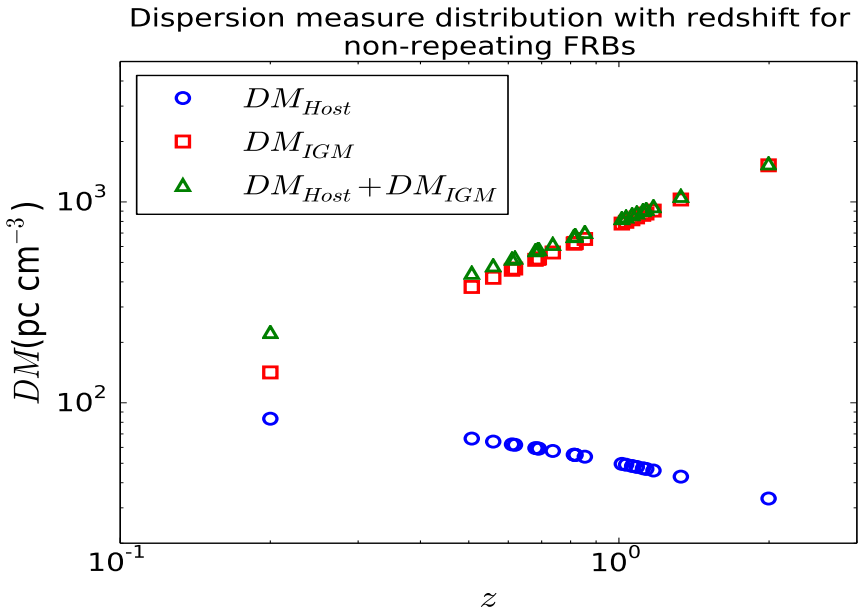

Figure 2.8: Plot of dispersion measure $DM_{\rm tot}$ with distance for non-repeating FRBs.

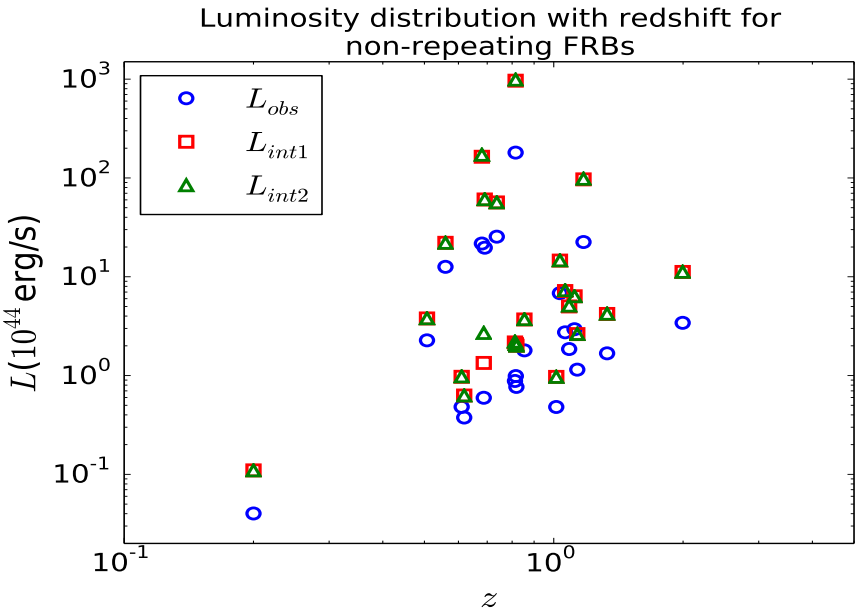

Figure 2.9: Plot of inferred luminosities L with distance for non-repeating FRBs.

for the non-repeating/repeating FRBs. We show the dependence of $S_{\rm peak}$, DM and L on z for the non-repeating bursts in Figures 2.7, 2.8 and 2.9. We find that both the observed and intrinsic $S_{\rm peak}$ of these events have no apparent correlation with the inferred distances. However, the relative scatter in the flux values for a given distance is considerably larger for intermediate $z \sim 1$. While the IGM contribution to the DM is found to be comparable to the host galaxy contribution for small $z \approx 0.2$, $DM_{\rm IGM}/DM_{\rm host} \gtrsim 10$ for larger $z \gtrsim 0.6$.

As most of the currently detected bursts have $z \gtrsim 0.6$, small variations in $DM_{\rm host}$ are not expected to significantly affect $DM_{\rm Ex} = DM_{\rm host} + DM_{\rm IGM}$, provided that the typical host galaxy properties are not very different from that of the MW. The burst luminosities increase on an average with an increase in the burst distance, which is expected as $S_{\rm peak}$ for FRBs is almost independent of z. Moreover, the bursts with higher $L_{\rm int}$ are easier to detect from larger distances

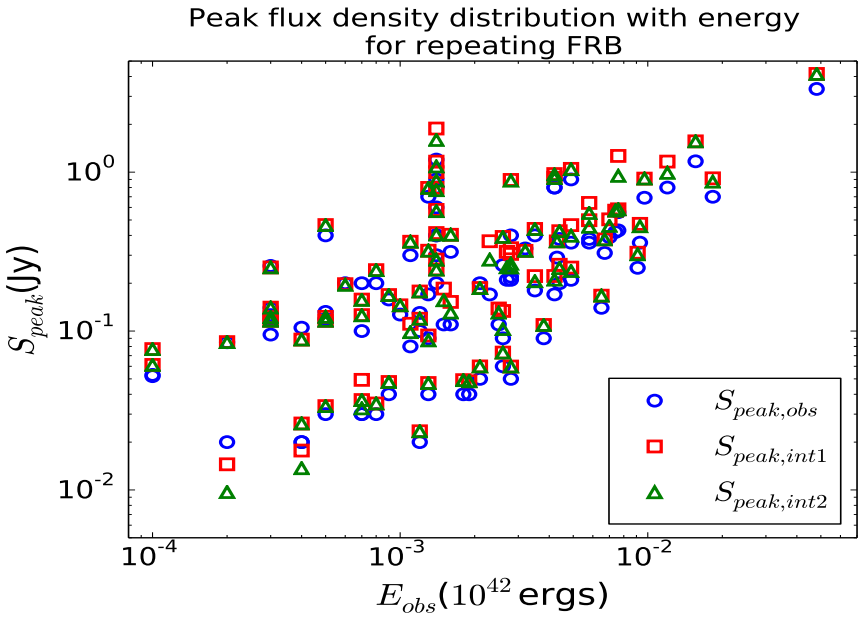

Figure 2.10: Plot of peak flux densities $S_{\rm peak}$ with burst energy for repeating FRB 121102.

compared to dimmer FRBs, for a given telescope sensitivity. In Figure 2.10, the dependence of $S_{\rm peak}$ on $E_{\rm obs}$ is shown for the reported sub-bursts of repeating FRB 121102. We find that the more energetic sub-bursts have a larger value of $S_{\rm peak}$ on average, which is reasonable as brighter bursts detected from a given distance are expected to emit more energy.

2.5 Error estimates for inferred parameters

We estimated the FRB distances from the observed $DM_{\rm tot}$ values by assigning $DM_{\rm host} \approx 100$ pc cm^{-3} as the fixed DM contribution from the host galaxy. However, the actual value of $DM_{\rm host}$ can vary over a significantly broader range depending on the type of the host galaxy and the location of the FRB source within it, thereby affecting our estimate for the inferred z. We also used two scat-

tering models for the pulse temporal broadening in the turbulent ISM and IGM in order to compute $w_{\rm int}$ from the observable $w_{\rm obs}$. The assumptions used in the scattering models considered can affect the intrinsic width obtained.

Furthermore, in addition to the pulse temporal broadening from propagation across turbulent plasma, the peak flux density $S_{\rm peak,int}$ is also reduced due to the finite size of the telescope beams. The inferred burst luminosities and energies are then directly affected by these modified $S_{\rm peak,int}$ values as well as the assumptions about the FRB energy density spectrum which we assume to be a power-law distribution in this work. Below we provide some rough estimates for each of these uncertainties in the inferred parameters.

1. *Error in the z estimate from $DM_{\rm host}$ contribution:* We previously assumed that the host galaxy has a free electron density structure that is similar to the MW and it provides a typical contribution of $DM_{\rm host} \approx 100$ pc cm^{-3} to $DM_{\rm tot}$. As the values for $DM_{\rm tot}$ and $DM_{\rm MW}$ are known for a given FRB line of sight, the estimate for the burst distance is primarily based on the assumption about the host galaxy DM contribution. In general, $DM_{\rm host}$ can have considerable spread $\Delta DM_{\rm host} \sim 100$ pc cm^{-3} due to the unknown location of the FRB source and our viewing angle relative to the galaxy. With $DM_{\rm IGM} \approx 750z$ pc cm^{-3} for the FRBs listed in Table 1, we have $DM_{\rm Ex} \approx DM_{\rm host}/(1+z) + 750z$ from equation (5.1). Substituting $\Delta DM_{\rm host} \sim DM_{\rm host} \approx 100$ pc cm^{-3} gives the redshift error to be $\Delta z \approx 0.2/(1+z)$ assuming $\Delta z \sim z \sim 1$ for most FRBs. The value for Δz gradually decreases with increasing distance which is expected as the relative contribution from the uncertain $DM_{\rm host}$ to $DM_{\rm tot}$ decreases.

2. *Error in the estimate for $w_{\rm int}$:* We find that the ISM broadening contributions from both scattering models are suppressed significantly due to the geometrical lever-arm factor of $\sim 10^{-4}$ and are very small with $w_{\rm ISM,MW/host} \lesssim 10^{-3}$ ms for all reported FRBs. Even though $w_{\rm IGM} \sim 10^{-2} - 10^{-1}$ ms is considerably larger, the modelled IGM temporal broadening contributions are still typically smaller by at least an order of magnitude compared to the dispersive smearing. Using equation (2.3), the intrinsic width can therefore be approximately written as $w_{\rm int}^2 \approx (w_{\rm obs}^2 - w_{\rm DM}^2)/(1+z)^2$ for all reported bursts. As $w_{\rm obs}$ and $w_{\rm DM} \propto DM_{\rm tot}$ are directly determined from the observations, the relative error in the intrinsic width is primarily due to Δz and is given as $\Delta w_{\rm int}/w_{\rm int} = 0.2/(1+z)^2$.

   For scattering model 1, the IGM/ISM pulse width broadening is based on the DM contribution with $w_{\rm IGM/ISM} \propto DM_{\rm IGM/ISM}^{4.2}$ for sufficiently large values of DM. Although density fluctuations in the ISM/IGM can increase $DM_{\rm ISM/IGM}$ by the factor of a few which can then increase $w_{\rm IGM/ISM}$ by almost two orders of magnitude, the corresponding change in $w_{\rm int}$ is found to be negligible due to the modelled scatter broadening widths being very small (see Figure **??**). In case of scattering model 2, the IGM pulse broadening is determined by both z and $k_{\rm IGM}$. From equation (5.3), $w_{\rm IGM}$ increases by almost an order of magnitude for the z range of FRBs in Table 6.1 with the error in $w_{\rm IGM}$ due to Δz being smaller for larger z. The value of the normalization constant $k_{\rm IGM}$ is fixed using the width parameters of a single FRB and can vary by a factor of few in general. However, as $w_{\rm IGM} \lesssim 10^{-2}\ w_{\rm obs}$ for most FRBs that we consider in our study, the dependence of $w_{\rm int}$ on the specific value of $k_{\rm IGM}$ is relatively weak.

3. *Effect of beam shape on $S_{\rm peak}$:* While the intrinsic peak flux density $S_{\rm peak,int}$ is diminished due to the pulse broadening from multipath propagation, the actual observed flux can be even smaller due to the finite size of the telescope beam used for detection. For a typical Gaussian beam profile, the observed flux density can be written as $S_{\rm peak,obs} \approx S_{\rm peak,int}\ \exp(-r'^2/r_{\rm beam}^2)$, where $r_{\rm beam}$ is the beam radius and r' is the radial distance from the beam center. The flux density averaged over an entire beam area is then $\langle S_{\rm peak,obs}\rangle = (S_{\rm peak,int}/\pi r_{\rm beam}^2)\int_0^{r_{\rm beam}} \exp(-r'^2/r_{\rm beam}^2) 2\pi r' dr' = S_{\rm peak}(1-e^{-1})$. Therefore, the relative uncertainty in the $S_{\rm peak,int}$ values from telescope and propagation effects can be combined to be written as
$\Delta S_{\rm peak,int}/S_{\rm peak,int} = \sqrt{(1/e)^2 + (\Delta w_{\rm int}/w_{\rm int})^2} = \sqrt{(1/e)^2 + 0.04/(1+z)^4} \approx 1/e$.

4. *Effect on the inferred luminosity and energy:* The inferred bolometric luminosity and energy are obtained using equation (5.4) from $S_{\rm peak}$ and $\mathcal{F}_{\rm obs}$, respectively, for a given burst. The measured values for $\mathcal{F}_{\rm obs}$ and $S_{\rm peak}$ are affected by the finite telescope beam size and $\Delta w_{\rm int}$. For our calculations, we assume the simple case of a flat FRB energy spectrum with $\alpha \approx 0$ for coherent source emission from 600 MHz to 8 GHz and a telescope detection bandwidth $\nu_{\rm bw} = \nu_2 - \nu_1$. However, the value of α is highly uncertain from the current observations. As $D(z) \propto z$, in terms of the inferred parameters we have $L \propto S_{\rm peak} f(\alpha) z^2$ and $E \propto \mathcal{F}_{\rm obs} f(\alpha) z^2$, where $f(\alpha) = (1+z)^{1-\alpha}(\nu'^{\alpha+1}_{max} - \nu'^{\alpha+1}_{min})/(\nu_2^{\alpha+1} - \nu_1^{\alpha+1})$. For Parkes $\nu_{\rm bw} = 0.34$ GHz and a typical FRB $z \sim 1$, the difference in the values of $f(\alpha)$ for $\alpha = 0$ and Kolmogorov spectral index $\alpha = -1.4$ is found to be very small $\lesssim 1/15$ and hence $\Delta f(\alpha)/f(\alpha) \ll 1$.

The relative uncertainty in the inferred luminosity and energy values are then obtained with $\Delta L/L = \sqrt{(\Delta S_{\rm peak}/S_{\rm peak})^2 + 4(\Delta z/z)^2}$ and $\Delta E/E = \sqrt{(\Delta \mathcal{F}_{\rm obs}/\mathcal{F}_{\rm obs})^2 + 4(\Delta z/z)^2} \approx 1/e$.

We have included these uncertainties in the inferred parameters z, $w_{\rm int}$, L and E to obtain the chi-squared fits for the cumulative distributions shown in Figures 2.3, 2.4, 2.5 and 2.6.

Chapter 3

Monte Carlo population synthesis code & simulation results

In the previous Chapter, we presented a method in order to estimate the true properties of the FRBs such as $w_{\rm int}$, $S_{\rm peak,int}$, $L_{\rm int}$ and $E_{\rm obs}$, from the observables for both non-repeating and repeating bursts. Here we describe our Monte Carlo (MC) population synthesis code with which we constrain the various properties of the FRB source, its host galaxy and the intervening turbulent plasma from the observed properties of the reported FRBs. We first discuss the initial parameters and distributions used in the MC code. Next, we briefly describe the algorithm of our MC code. Then we discuss in detail the simulation results and the associated constraints on the FRB source properties imposed from statistical analysis.

3.1 FRB input parameters

The input parameters used for our MC simulations are:

- *Burst type:* We categorise all FRBs into two different classes of bursts: non-repeating and repeating FRBs. We model the population of the non-repeating/ repeating FRBs found at the Parkes MB/Arecibo ALFA (see Table 3.1 for the system parameters of these surveys). Parkes MB/Arecibo ALFA has 13/7 beams with different beam center gains $G_{\rm beam}$ and beam radii $r_{\rm beam}$.

Table 3.1: System parameters for the Parkes multibeam (MB) receiver are obtained from Staveley-Smith et al. (1996) and those for the Arecibo L-band feed array (ALFA) are obtained from http://www.naic.edu/alfa/.

Parameter	Parkes MB	Arecibo ALFA
Digitization factor (δ)	1.07	1.16
System temperature ($T_{\rm sys}$)	30	30
Central frequency in MHz (ν_0)	1352	1375
Frequency bandwidth in MHz ($\nu_{\rm bw}$)	338	323
Channel bandwidth in MHz ($\Delta\nu_0$)	0.390	0.336
Sampling width in ms ($w_{\rm samp}$)	0.0640	0.0655

For Parkes MB, $r_{\rm beam} = 7.0'$ ($7.05'$) [$7.25'$] and $G_{\rm beam} = 0.731$ (0.690) [0.581] K Jy^{-1} for beam 1 (2-7) [8-13], while Arecibo ALFA has $r_{\rm beam} = 3.35'$ ($3.35'$) and $G_{\rm beam} = 10.4$ (8.2) K Jy^{-1} for beam 1 (2-7).

- *Scattering model:* As the distributions of the true properties derived from the current observations are found to be practically similar for both scattering models (see Section 2.1), here we only consider model 2 to determine the scatter broadening of the intrinsic pulse width for each FRB due to propagation through the turbulent ISM and IGM.

- *FRB intrinsic width and luminosity distributions:* We consider two separate model distributions for both $w_{\rm int}$ and $L_{\rm int}$ in our MC simulations. As the observed pulse widths for non-repeating/repeating FRBs vary within a broad range of $\sim 0.6 - 21.0$ ms/$\sim 0.15 - 8.70$ ms and are peaked around

~ 3.0 ms/~ 1.8 ms, we use two different model distributions for the intrinsic width $w_{\rm int}$ which are:

(a) *Intrinsic width model W1:* lognormal distribution with mean $\mu_1 = 0$ and standard deviation $\sigma_1 = 0.25$, and

(b) *Intrinsic width model W2:* lognormal distribution with mean $\mu_2 = 0$ and standard deviation $\sigma_2 = 0.50$.

For the known $w_{\rm obs}$ distribution, the W1/W2 intrinsic width distribution physically corresponds to larger/smaller pulse temporal broadening due to scattering in the intervening plasma.

The inferred luminosities for the non-repeating/repeating FRBs vary within a wide range with fewer bursts detected at larger luminosities. Here we assume power-law (PL) intrinsic luminosities for both classes of FRBs with:

(a) *Inferred luminosity model L1:* PL distribution with index $\alpha_{L_{\rm int}} = -1.3$, and

(b) *Inferred luminosity model L2:* PL distribution with index $\alpha_{L_{\rm int}} = -1.8$.

We use $L_{\rm min} = 10^{43}$ erg/s and $L_{\rm max} = 10^{45}$ erg/s for non-repeating FRBs whereas the corresponding quantities are 10^{41} erg/s and 10^{43} erg/s for repeating FRBs. Here the broader luminosity distribution L1 physically corresponds to larger pulse scatter broadening due to multipath propagation.

- *FRB source spatial density $n(z)$:* In order to estimate the number of FRB sources in a given comoving volume, we consider three different spatial density distributions:

1. *Non-evolving (NE) population:* The number of FRB progenitors increases linearly with the comoving volume for a non-evolving population. From Table 6.1, we know that the maximum inferred redshift value for the reported FRBs is $z \approx 2.3$.

   We generate FRBs up to a maximum redshift $z_{\rm max} = 3.0$, corresponding to a maximum comoving volume $V_{\rm c,max} \approx 1286$ Gpc^3 for typical cosmological parameters. The comoving distances to the FRBs are obtained as $D_c = (3\zeta_1 V_{\rm c,max}/4\pi)^{1/3}$, where ζ_1 is a uniform random number between 0 and 1. The associated z is then obtained by inverting $D(z) = (8.49 \text{ Gpc}) \int_0^z [(1+z')^3 + 2.7]^{-0.5} dz'$.

2. *Tracking cosmic star formation history (SFH):* As the majority of the FRB progenitor models suggested (including both cataclysmic and non-cataclysmic scenarios) involve young neutron stars, the spatial distribution of FRBs is expected to track the cosmic SFH. Furthermore, few reported FRBs have inferred distances exceeding $z \approx 2.0$, in which case the FRB spatial density can be significantly different compared to a NE population. We consider the cosmic SFH functional fit suggested by Madau & Dickinson (2014),

$$\psi(z) = (0.015 \text{ M}_\odot \text{yr}^{-1} \text{Mpc}^{-3}) \frac{(1+z)^{2.7}}{1 + [(1+z)/2.9]^{5.6}}. \qquad (3.1)$$

   The FRB redshifts are generated by inverting $\zeta_2 = \int_0^z \psi(z')dz' / \int_0^3 \psi(z')dz'$, where ζ_2 is a uniform random number between 0 and 1. We then obtain $z = 12.05\zeta_2 - 57.16\zeta_2^2 + 167.97\zeta_2^3 - 259.28\zeta_2^4 + 199.04\zeta_2^5 - 59.63\zeta_2^6$.

3. *Power-law distribution:* We also consider a broken power-law FRB

spatial density given by,

$$n(z) = n_0 \begin{cases} (1+z)^{\alpha_l}, & z_{\rm min} \leq z < z_{\rm crit} \\ (1+z)^{\alpha_u}, & z_{\rm crit} \leq z \leq z_{\rm max} \end{cases} \tag{3.2}$$

where n_0 is a constant, α_l/α_u is the lower/upper power-law index, $z_{\rm min}/z_{\rm max}$ is the minimum/maximum redshift and $z_{\rm crit}$ is the redshift at which $n(z)$ peaks. We try to constrain the distribution parameters α_l, α_u and $z_{\rm crit}$ from the observed FRB population. From the cosmic SFH fit (equation 3.1), we have $\alpha_l \approx 2.7$ at low z, $\alpha_u \approx -2.9$ at high z and $z_{\rm crit} \approx 1.85$ from the peak of the distribution. We use $z_{\rm min} = 0$ and $z_{\rm max} = 3.0$ to generate the FRB redshifts from the power-law $n(z)$ distribution.

- *β-parameter for $DM_{\rm host}$:* As opposed to a constant $DM_{\rm host}$ contribution along all lines of sight, we assume that the free electron density distribution in the host galaxy is similar to that of the Milky Way and can be obtained using the NE2001 model (Cordes & Lazio 2002). We estimate the DM contribution due to the host galaxy ISM along the FRB source line of sight as, $DM_{\rm host} = \beta DM_{\rm NE2001}$, where β is the parameter that accounts for the size of the FRB source host galaxy relative to the MW and $DM_{\rm NE2001}$ is the DM value predicted by the NE2001 model. In this work, we consider $\beta = 0.1$, 1.0 and 10.0 for the non-repeating FRBs. For the repeating FRB 121102, we use $DM_{\rm MW} = 188$ pc cm^{-3} and $DM_{\rm host} = 281$ pc cm^{-3} for all generated FRBs.

  We assume that all bursts are located at the position of the Solar system in the host galaxy and all lines of site are weighted equally, as the location of

the FRB source within its host galaxy is highly uncertain at present. This also eliminates any possible bias from the specific choice of a volumetric function for the distribution of source locations within the host galaxy. As $DM_{\rm tot}$ is expected to be significantly larger compared to $DM_{\rm host}$ (which is constrained by the plasma frequency and further diminished by the cosmological expansion factor), the assumption about the FRB source location is not expected to affect the results significantly.

For our simple analysis here, we ignore the contribution to the DM from free electrons in the halos of any intervening galaxies and assume a diffuse homogeneous structure for both IGM and ISM. Recently, Prochaska & Zheng (2019) have shown that the contribution to $DM_{\rm Ex}$ from $DM_{\rm host}$ is essentially stochastic with the relative scatter in $DM_{\rm Ex}$ values being largest for nearby FRBs due to a larger relative uncertainty involved from $DM_{\rm host}$.

For host galaxies that are similar to the MW, the free electrons in the galactic halo are expected to have a relatively small contribution with $DM_{\rm host} \lesssim 30$ pc cm^{-3} (Dolag et al., 2015). While $DM_{\rm IGM}$ can vary for FRBs at a similar z depending on the density inhomogeneities along the line of sight (McQuinn 2014), the DM variability from cosmic web voids and strong filaments is found to be typically small $\lesssim 10$ pc cm^{-3} (Smith et al., 2011; Shull & Danforth 2018; Ravi 2019).

- *FRB energy density spectral index α:* Instead of using a flat FRB energy density spectrum, we assume that the FRB energy spectrum can be modelled using a power-law, $E_{\nu'} = k\nu'^{\alpha}$, where ν' is the frequency in the source frame

and α is the spectral index. The FRB bolometric luminosity and energy are then given by equation (5.4).

Even though the coherent emission mechanism for FRBs suggests a negative spectral index, the spectral indices for some of the reported bursts vary within a wide range. Macquart et al. (2019) recently obtained the best-fit value $\alpha \approx -1.5$ from the spectra of 23 FRBs detected with ASKAP (Bannister et al., 2017; Shannon et al., 2018), which is similar to that of the Galactic pulsar population. For completeness, here we consider $\alpha = -3.0$, -1.5 and 2.0.

3.2 Monte Carlo code algorithm

At the start of the simulation, we select a specific burst type for the FRB events to be generated. We then draw the intrinsic pulse width $w_{\rm int}$ and luminosity $L_{\rm int}$ of the first event from the corresponding model distributions (W1/W2 for width and L1/L2 for luminosity) and compute the burst energy $E_{\rm int} = w_{\rm int} L_{\rm int}$. Next, we draw $D(z)$ for the burst and evaluate the corresponding z for the chosen FRB spatial density model $n(z)$. Once the distance to the FRB is known, we further estimate $DM_{\rm IGM}(z)$ and $w_{\rm IGM}(z)$ from scattering model 2.

We then draw a random line of sight in the MW and get $DM_{\rm MW}$ from the NE2001 model. For the host galaxy ISM contribution, we choose a random line of sight in the host galaxy to evaluate $DM_{\rm host} = \beta DM_{\rm NE2001}$ for the β value selected. Once the $DM_{\rm MW}$ and $DM_{\rm host}$ contributions are known, we obtain the corresponding pulse width broadening components $w_{\rm ISM,MW}$ and $w_{\rm ISM,host}$. We include the IGM contribution to the DM to estimate $DM_{\rm tot}$ and the pulse dispersive smearing

$w_{\rm DM}$. The observed pulse width $w_{\rm obs}$ is obtained by adding $w_{\rm samp}$ to the previously estimated width components (see equation 2.3).

For a power-law FRB energy density with spectral index α chosen earlier, the peak flux density at the beam center $S_{\rm peak,bc}$ can be obtained from $L_{\rm int}$ for an observation in the frequency band between $\nu_1 = \nu_0 - (1/2)\nu_{\rm bw}$ and $\nu_2 = \nu_0 + (1/2)\nu_{\rm bw}$ as

$$S_{\rm peak,bc} = \frac{L_{\rm int}(1+z)^{\alpha-1}}{4\pi D(z)^2(\nu'^{\alpha+1}_{\rm max} - \nu'^{\alpha+1}_{\rm min})} \frac{w_{\rm int}}{w_{\rm obs}} \left(\frac{\nu_2^{\alpha+1} - \nu_1^{\alpha+1}}{\nu_2 - \nu_1} \right) \tag{3.3}$$

where the factor $w_{\rm int}/w_{\rm obs}$ accounts for the reduction in $L_{\rm int}$ due to pulse scattering and/or dispersive smearing. We assume FRB coherent emission to be in the frequency range between $\nu'_{\rm min} = 600$ MHz and $\nu'_{\rm max} = 8$ GHz, in agreement with the current observations.

However, the observed flux $S_{\rm peak,obs}$ can be significantly smaller compared to $S_{\rm peak,bc}$ due to the finite telescope beam size and for a Gaussian beam profile is given by

$$S_{\rm peak,obs} = S_{\rm peak,bc} \exp\left[-(2\ \ln 2) \frac{r'^2}{r^2_{\rm beam}} \right]. \tag{3.4}$$

While the probability of a particular beam detecting the FRB event is proportional to its area $\sim \pi r^2_{\rm beam}$, the radial distance r' from the beam center is chosen randomly. For pulses detected in single-pulse searches, the search trial width $w_{\rm trial}$ has to be closest to the observed pulse width $w_{\rm obs}$. In our simulation, we generate $w_{\rm trial}$ in powers of two starting from $w_{\rm samp}$ in order to find $w_{\rm trial}$ nearest to $w_{\rm obs}$. Once $w_{\rm trial}$ is determined, the signal-to-noise ratio S/N for optimal detection is obtained from $S_{\rm peak,obs}$ and the other telescope parameters as

$$\frac{S}{N} = \frac{S_{\rm peak,obs}}{T_{\rm sys}\delta} G_{\rm beam} \sqrt{2\nu_{\rm bw} w_{\rm trial}}. \tag{3.5}$$

The FRB event is detected only if the signal-to-noise ratio $S/N \geq 9$ (5) for Parkes MB (Arecibo ALFA).

In addition, we discard all the events for which $DM_{\rm tot} < 500$ pc cm^{-3} is obtained. The simulation continues with the aforementioned algorithm until $N_{\rm det} = 3000$ events have been detected. From $S_{\rm peak,obs}$ of a given FRB, we further obtain the observed fluence $\mathcal{F}_{\rm obs} = S_{\rm peak,obs} w_{\rm obs}$, luminosity $L_{\rm obs} = 4\pi D(z)^2(1+z) S_{\rm peak,obs}(\nu'_{\rm max} - \nu'_{\rm min})$ and energy $E_{\rm obs} = 4\pi D(z)^2(1+z)\mathcal{F}_{\rm peak,obs}(\nu'_{\rm max} - \nu'_{\rm min})$. The observed ($S_{\rm peak,obs}$, $\mathcal{F}_{\rm obs}$, $DM_{\rm tot}$, $w_{\rm obs}$) and inferred (z, $L_{\rm obs}$, $E_{\rm obs}$) properties for every detected burst are stored for comparison with the observed FRB population in order to constrain the input parameters.

3.3 Simulation results and parametric constraints

In the previous sections, we described the MC code algorithm and discussed the input parameters for our code. Here we present the simulation results for the non-repeating FRBs and further compare them with observations in order to constrain the model parameters of the FRB population. We discuss the simulation results of the NE and SFH $n(z)$ distributions for non-repeating FRBs that are detectable with Parkes, and use Kolmogorov-Smirnov (KS) test to compare them with the current observations.

For NE and SFH $n(z)$, we perform MC simulations with all four combinations of the model distributions for $w_{\rm int}$ and $L_{\rm int}$ - we hereby denote them as wiLi, where $i = 1, 2$ corresponds to the specific distribution (see Section 3.1). We identify the parametric spaces (β,α) where the p-value γ obtained from the KS test is maximised for a given spatial density distribution.

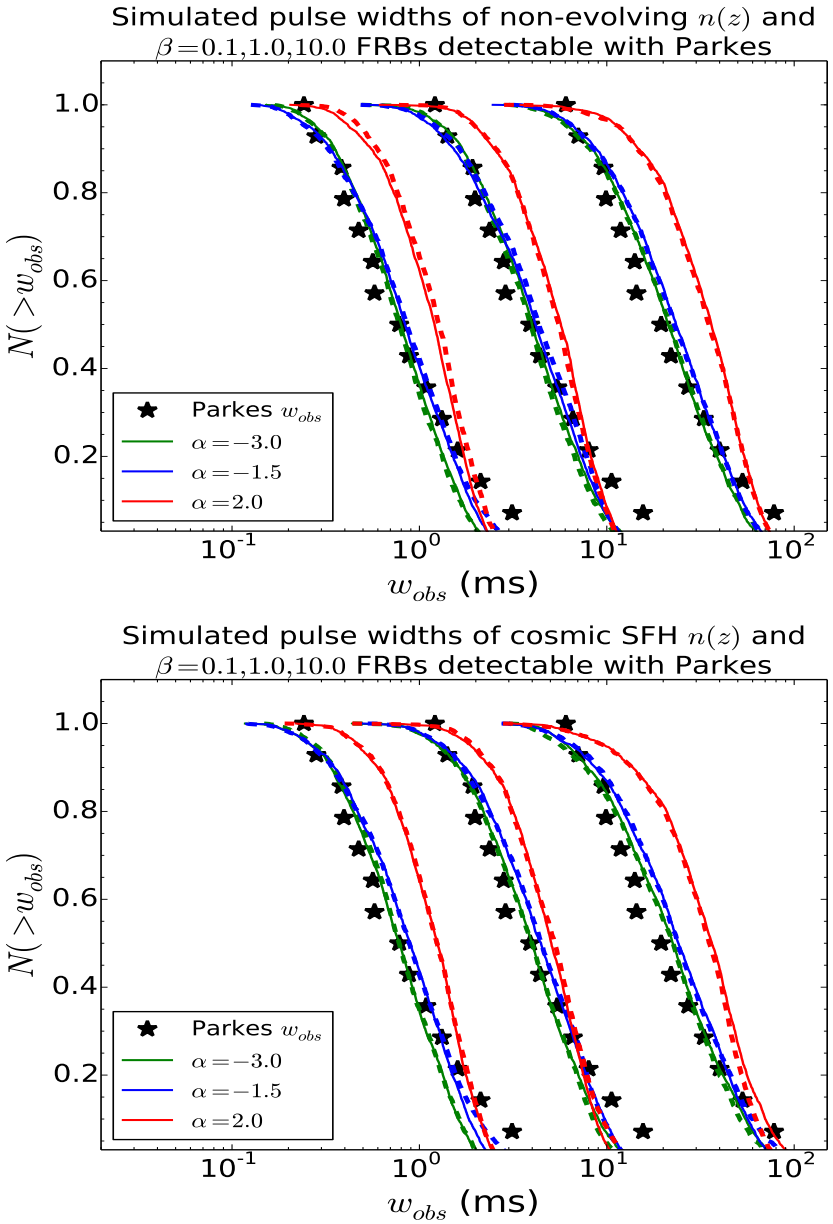

Figure 3.1: *Comparison of* $w_{\rm obs}$ *distributions for simulated NE (top panel) and SFH (bottom panel) FRBs with non-repeating Parkes FRBs:* In each panel, the MC simulation results are shown for $DM_{\rm host}$ parameter $\beta = 0.1, 1.0, 10.0$, spectral index $\alpha = -3.0, -1.5, 2.0$, scattering model 2, and intrinsic models w1L1 and w1L2. The cumulative distributions for intrinsic model w1L1/w1L2 are denoted by the dashed/solid lines. The values for the burst parameters are scaled from their actual values by a factor of 0.2/5.0 for $\beta = 0.1/10.0$ to avoid overlap. *Top panel:* Simulation results for $w_{\rm obs}$ of NE FRBs, *Bottom panel:* Simulation results for $w_{\rm obs}$ of SFH FRBs.

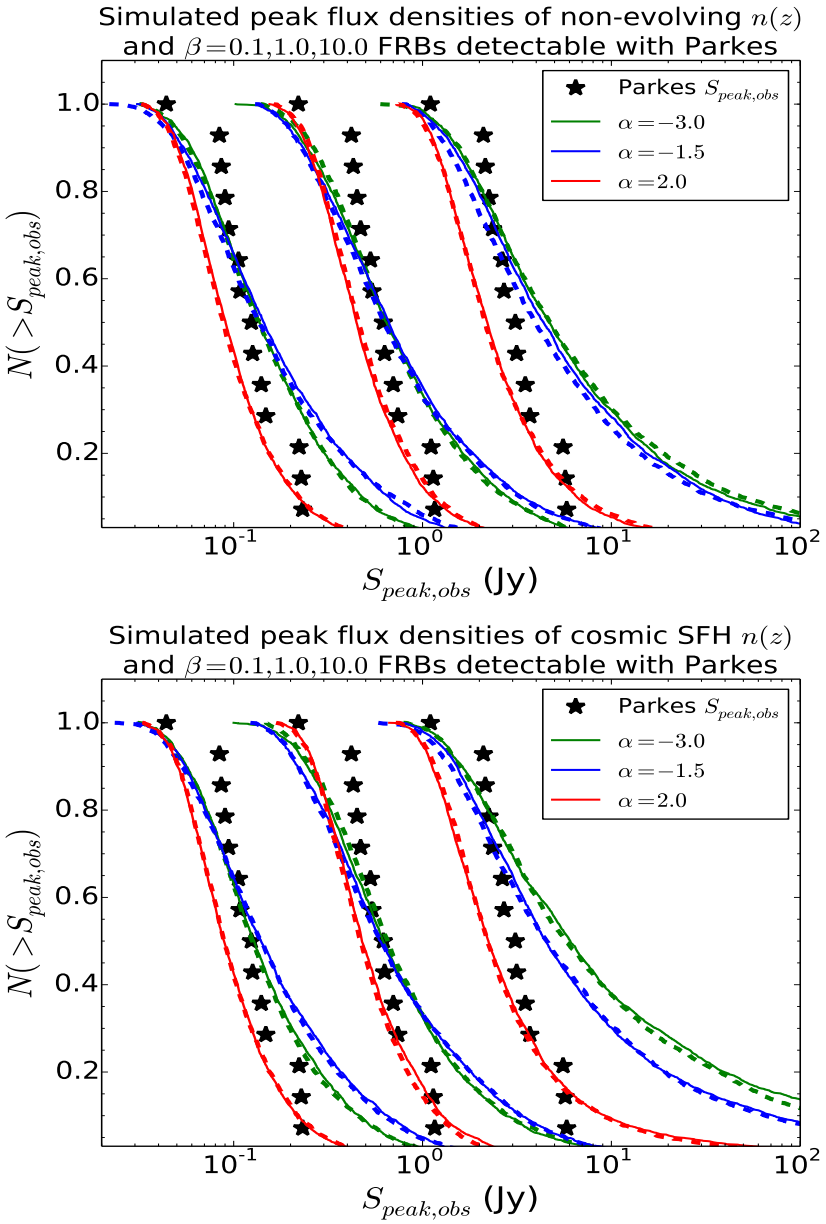

Figure 3.2: *Comparison of $S_{\rm peak,obs}$ distributions for simulated NE (top panel) and SFH (bottom panel) FRBs with non-repeating Parkes FRBs:* In each panel, simulation results are shown for $DM_{\rm host}$ parameter $\beta = 0.1, 1.0, 10.0$, spectral index $\alpha = -3.0, -1.5, 2.0$, scattering model 2, and intrinsic models w1L1 and w1L2. The cumulative distributions for intrinsic model w1L1/w1L2 are denoted by the dashed/solid lines. The values for the burst parameters are scaled from their actual values by a factor of 0.2/5.0 for $\beta = 0.1/10.0$ to avoid overlap. *Top panel:* Simulation results for $S_{\rm peak,obs}$ of NE FRBs, *Bottom panel:* Simulation results for $S_{\rm peak,obs}$ of SFH FRBs.

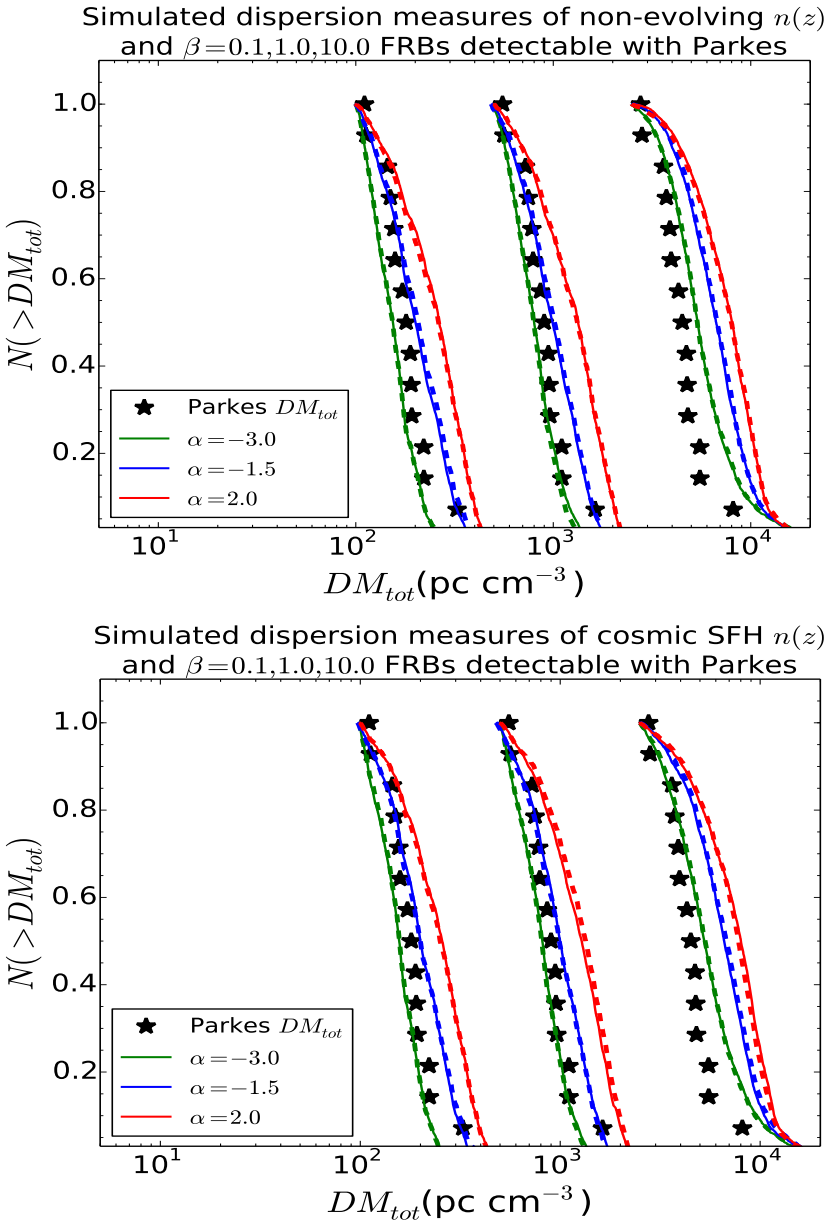

Figure 3.3: *Comparison of $DM_{\rm tot}$ distributions for simulated NE (top panel) and SFH (bottom panel) FRBs with non-repeating Parkes FRBs:* In each panel, the MC simulation results are shown for $DM_{\rm host}$ parameter $\beta = 0.1, 1.0, 10.0$, spectral index $\alpha = -3.0, -1.5, 2.0$, scattering model 2, and intrinsic models w1L1, w1L2. Cumulative parameter distributions for intrinsic model w1L1/w1L2 are denoted by dashed/solid lines. The values for burst parameters are scaled from actual values by a factor of 0.2/5.0 for $\beta = 0.1/10.0$ to avoid overlap. *Top panel:* Simulation results for $DM_{\rm tot}$ of NE FRBs, *Bottom panel:* Simulation results for $DM_{\rm tot}$ of SFH FRBs.

Then, we specifically consider the cases where γ is maximised to further constrain the parameters of the PL $n(z)$ distribution and identify (α_l,α_u,$z_{\rm crit}$) favored by the observations. The p-values obtained from the KS test comparison of the simulated and observed parameter distributions are listed in Tables C.1, C.2 and C.3 of Appendix B for all the cases considered. We perform all KS tests under the null hypothesis that the two samples were drawn from the same distribution unless the p-value $\gamma < 0.05$.

3.3.1 Non-evolving and cosmic star formation history FRB spatial densities

We show the results for the simulated $w_{\rm obs}$, $S_{\rm peak,obs}$ and $DM_{\rm tot}$ distributions of the non-repeating FRBs and compare them with the data from Parkes at $\nu_{\rm obs} =$ 1.4 GHz in Figures 3.1, 3.2 and 3.3. These simulations are performed for NE and SFH $n(z)$ distributions with the intrinsic models w1L1 and w1L2, $DM_{\rm host}$ in the range $\beta \sim 0.1 - 10.0$ and the energy spectral index within range $\alpha \sim -3.0$ to 2.0. We do not show the results for intrinsic width model W2 in these figures as the corresponding simulated distributions are found to be similar to those for model W1 for a given set of FRB parameters.

We consider $w_{\rm obs}$ and $S_{\rm peak,obs}$ to be the independent set of parameters among ($w_{\rm obs}$, $S_{\rm peak,obs}$, $\mathcal{F}_{\rm obs}$) in addition to $DM_{\rm tot}$ in order to evaluate the equivalent p-value $\gamma_{\rm eq} = \sqrt{\gamma^2_{w_{\rm obs}} + \gamma^2_{S_{\rm peak,obs}} + \gamma^2_{DM_{\rm tot}}}$ in each case. The p-values obtained by comparing the simulated parameters for both the NE and SFH $n(z)$ cases with the Parkes observations are listed in Tables C.1 and C.2 in Appendix B.

We find that the four model distributions (w1L1, w1L2, w2L1 and w2L2) considered for the intrinsic widths and luminosities of non-repeating FRBs are

practically indistinguishable for both NE and SFH $n(z)$ populations. This further indicates the weak dependence of the simulated FRB observable properties on the intrinsic source properties for the range of model parameters that we consider here.

We find that for both NE and SFH burst spatial densities, the observed $w_{\rm obs}$ from Parkes are in better agreement with the simulated $w_{\rm obs}$ for a host galaxy DM contribution $DM_{\rm host}$ that is comparable to the Galactic contribution with $\beta \sim 0.1 - 1.0$ as opposed to $\beta \gtrsim 10.0$. Moreover, the observed $w_{\rm obs}$ distribution suggests a large negative spectral index α for the FRB energies as $\gamma_{w_{\rm obs}}$ gradually decreases with increase in α for both $n(z)$ distributions.

In case of $S_{\rm peak,obs}$, we also find that a larger $DM_{\rm host}$ contribution $\beta \gtrsim 10.0$ cannot physically explain the observed flux density distribution for either of the FRB population density distributions. Similar to the observed $w_{\rm obs}$ distribution, the observed $S_{\rm peak,obs}$ from Parkes can be better explained for a power-law FRB energy spectrum with a negative spectral index as $\gamma_{S_{\rm peak,obs}}(\alpha = -3.0) \gtrsim \gamma_{S_{\rm peak,obs}}(\alpha = -1.5) > \gamma_{S_{\rm peak,obs}}(\alpha = 2.0)$ for both $n(z)$ considered.

For both NE and SFH spatial density distributions used here, $DM_{\rm host} \sim DM_{\rm MW}$ is clearly favored from the $DM_{\rm tot}$ detected at Parkes with $\gamma_{DM_{\rm tot}}(\beta \sim 0.1 - 1.0) \gg \gamma_{DM_{\rm tot}}(\beta \sim 10.0)$. The observed $DM_{\rm tot}$ values at Parkes are expected to arise from a relatively steep FRB energy density distribution with $\gamma_{DM_{\rm tot}}(\alpha = -3.0) > \gamma_{DM_{\rm tot}}(\alpha = -1.5) > \gamma_{DM_{\rm tot}}(\alpha = 2.0)$ for both FRB $n(z)$.

From the simulated FRB parameters and the Parkes data, we find that the host galaxy DM contribution is likely to be smaller or comparable to the MW contribution with the likelihood order $\beta = 1.0 \approx \beta = 0.1 > \beta = 10.0$. Furthermore,

a larger negative value of α is favored by the FRB observations in general with the order $\alpha = -3.0 > \alpha = -1.5 \gg \alpha = 2.0$. We find that the non-repeating FRB population observed with Parkes that is considered here is statistically insufficient and a larger observed population is necessary to clearly differentiate between the two FRB spatial density distributions considered in our study.

3.3.2 Power-law FRB spatial density

In order to constrain the parameters of the PL $n(z)$ distribution, we consider specific (β,α) combinations for which the KS test likelihood value is found to be significantly large for either NE or SFH $n(z)$ distributions (see Tables C.1 and C.2). As the choice of the intrinsic width and luminosity model (w1L1/w1L2/w2L1/w2L2) does not influence the likelihood value significantly, we assume the w1L1 model for all our simulations along with:

1. $\beta = 0.1$ and $\alpha = -3.0$,
2. $\beta = 1.0$ and $\alpha = -3.0$,
3. $\beta = 10.0$ and $\alpha = -3.0$,

as the three input cases. We show the simulated $w_{\rm obs}$, $S_{\rm peak,obs}$ and $DM_{\rm tot}$ distributions corresponding to these cases for comparison with the observed non-repeating FRB population detected by Parkes at $\nu_{\rm obs} = 1.4$ GHz in Figures 3.4, 3.5 and 3.6. In order to constrain the parameters (α_l,α_u,$z_{\rm crit}$) of the PL $n(z)$ distribution, we perform the MC simulations with either varying $z_{\rm crit}$ or varying (α_l,α_u) for each of these cases listed above.

We consider $z_{\rm crit}$ = 1.0, 2.0, 3.0 for fixed (α_l,α_u) = (2.7,-2.9), where the values for the PL indices are motivated from the SFH distribution at asymptotically low and high redshifts. For the fixed $z_{\rm crit}$ case, we consider $(\alpha_l, \alpha_u) =$

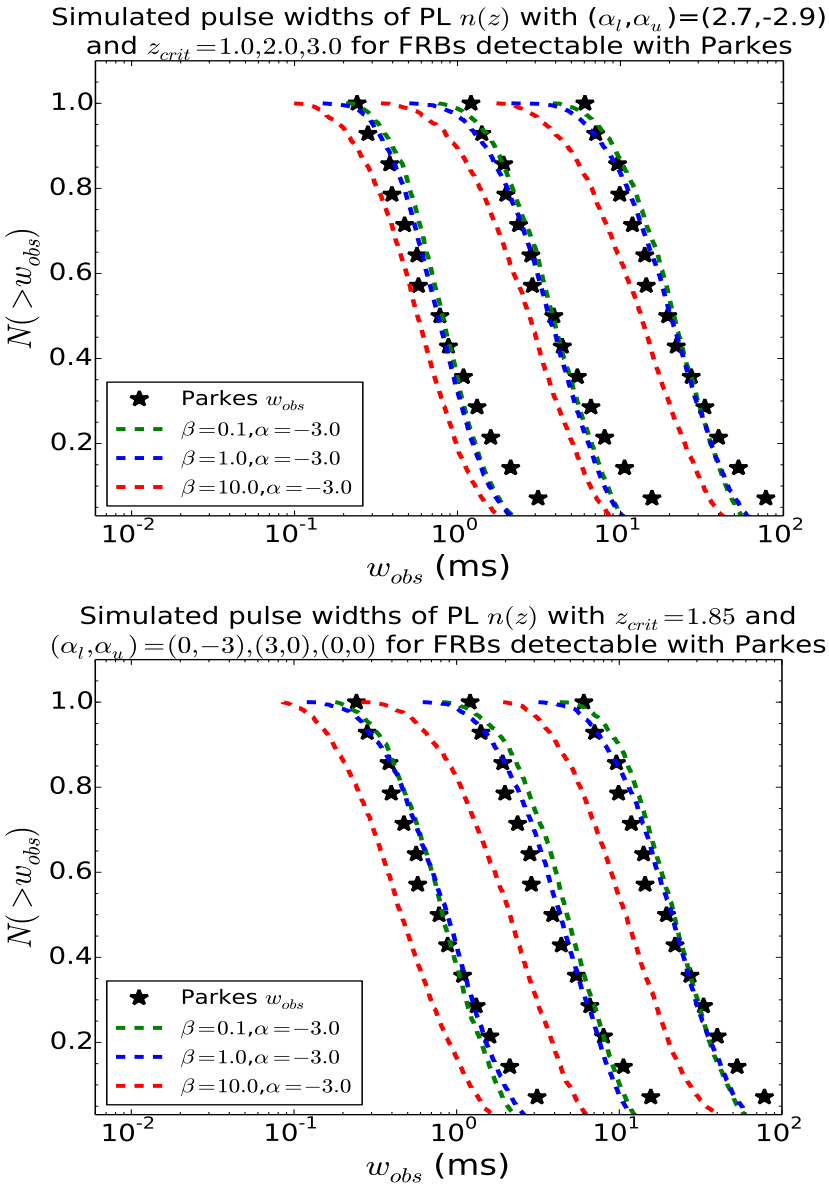

Figure 3.4: *Comparison of non-repeating Parkes FRBs and simulated* $w_{\rm obs}$ *for PL FRBs with varying* $z_{\rm crit}$ *(top panel) or varying* ($\alpha_{\rm l}$,$\alpha_{\rm u}$) *(bottom panel):* The cumulative distributions for the three cases are shown for scattering model 2 and intrinsic model w1L1, and the corresponding p-values are presented in Table C.3. We only show simulation results for intrinsic model w1L1. The FRB parameter values are scaled by a factor 0.2/5.0 for $z_{\rm crit}$ = 1.0/3.0 in the top panel, while the corresponding values are scaled by 0.2/5.0 for ($\alpha_{\rm l}$,$\alpha_{\rm u}$)=(0,-3)/(0,0) in the bottom panel to avoid overlap. *Top panel:* Simulated $w_{\rm obs}$ for fixed ($\alpha_{\rm l}$,$\alpha_{\rm u}$)=(2.7,-2.9) and varying $z_{\rm crit}$=1.0,2.0,3.0, *Bottom panel:* Simulated $w_{\rm obs}$ for fixed $z_{\rm crit}$ = 1.85 and varying ($\alpha_{\rm l}$,$\alpha_{\rm u}$)=(0,-3),(3,0),(0,0).

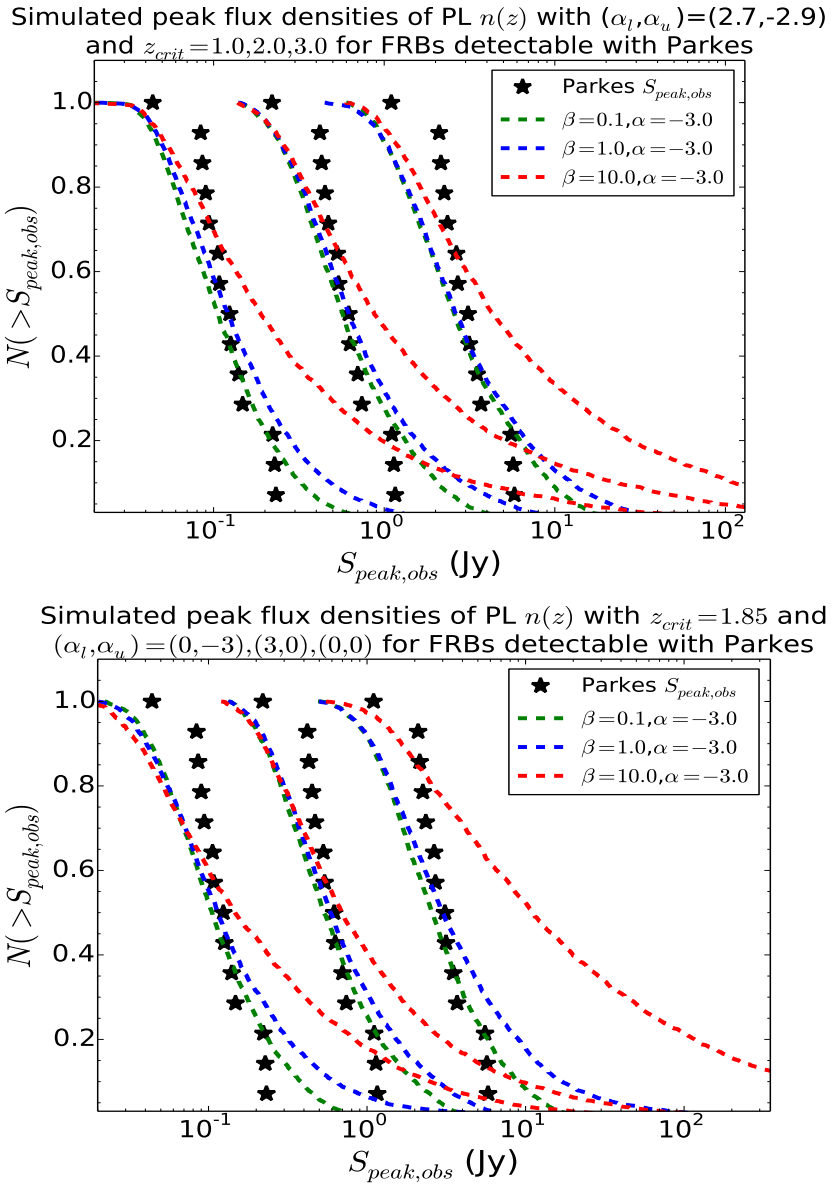

Figure 3.5: *Comparison of non-repeating Parkes FRBs and simulated* $S_{\rm peak,obs}$ *for PL FRBs with varying* $z_{\rm crit}$ *(top panel) or varying* $(\alpha_{\rm l},\alpha_{\rm u})$ *(bottom panel):* The cumulative distributions for the three cases are shown for scattering model 2 and intrinsic model w1L1, and the corresponding p-values are presented in Table C.3. We only show the simulation results for intrinsic model w1L1. The FRB parameter values are scaled by a factor 0.2/5.0 for $z_{\rm crit}$ = 1.0/3.0 in the top panel, while the corresponding values are scaled by 0.2/5.0 for (α_l,α_u)=(0,-3)/(0,0) in the bottom panel to avoid overlap. *Top panel:* Simulated $S_{\rm peak,obs}$ for fixed $(\alpha_{\rm l},\alpha_{\rm u})$ and varying $z_{\rm crit}$, *Bottom panel:* Simulated $S_{\rm peak,obs}$ for fixed $z_{\rm crit}$ and varying $(\alpha_{\rm l},\alpha_{\rm u})$.

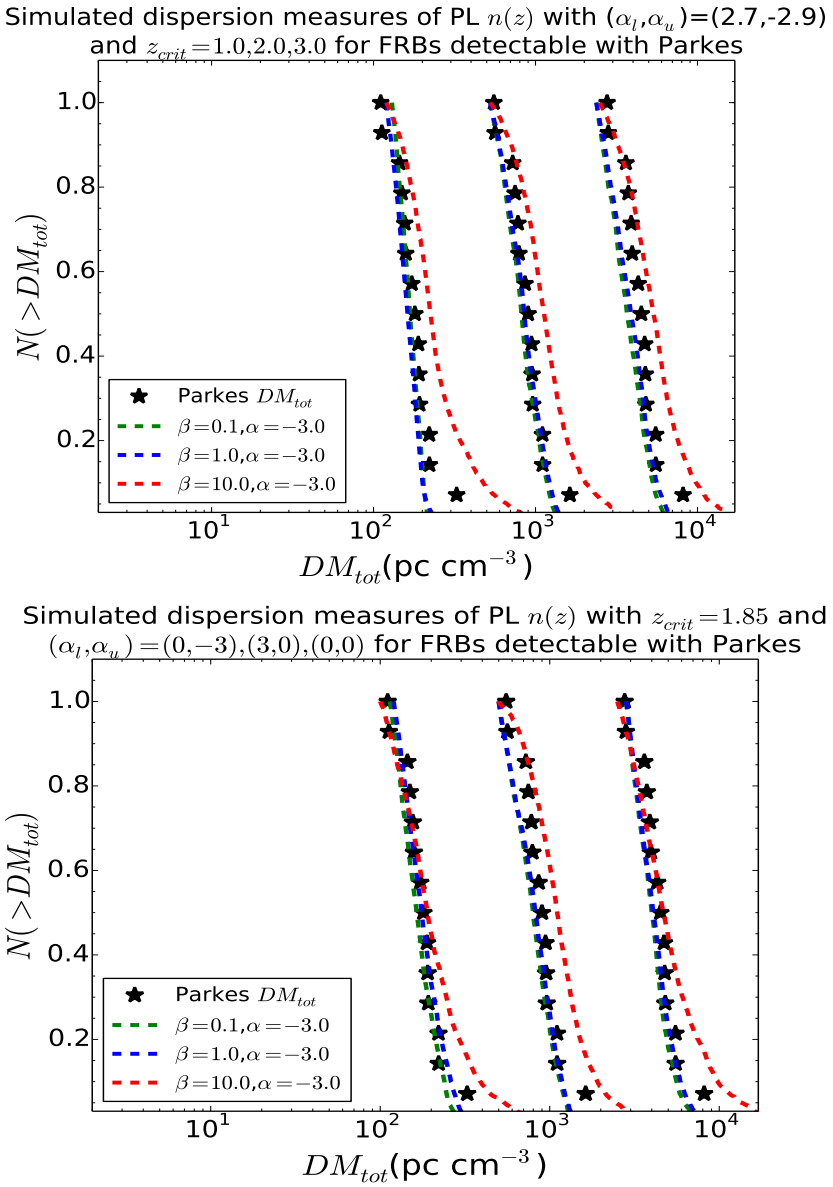

Figure 3.6: *Comparison of non-repeating Parkes FRBs and simulated $DM_{\rm tot}$ for PL FRBs with varying $z_{\rm crit}$ (top panel) or varying ($\alpha_{\rm l}$,$\alpha_{\rm u}$) (bottom panel):* The cumulative distributions for the three cases are shown for scattering model 2 and intrinsic model w1L1, and the corresponding p-values are presented in Table C.3. We only show the simulation results for intrinsic model w1L1. The FRB parameter values are scaled by a factor 0.2/5.0 for $z_{\rm crit}$ = 1.0/3.0 in the top panel, while the corresponding values are scaled by 0.2/5.0 for (α_l,α_u)=(0,-3)/(0,0) in the bottom panel to avoid overlap. *Top panel:* Simulated $DM_{\rm tot}$ for fixed ($\alpha_{\rm l}$,$\alpha_{\rm u}$) and varying $z_{\rm crit}$, *Bottom panel:* Simulated $DM_{\rm tot}$ for fixed $z_{\rm crit}$ and varying ($\alpha_{\rm l}$,$\alpha_{\rm u}$).

$(0, -3)$, $(3, 0)$, $(0, 0)$ and the value of $z_{\rm crit} = 1.85$ is chosen to resemble the redshift at which the cosmic SFH distribution peaks.

Table C.3 in Appendix B lists the p-values $\gamma_{\rm eq}$ obtained by comparing the simulated parameters for both the fixed $z_{\rm crit}$ and fixed (α_l,α_u) cases with the observed FRBs from Parkes. From the fixed (α_l,α_u) and varying $z_{\rm crit}$ case, we find that the agreement of each of the simulated $w_{\rm obs}$, $S_{\rm peak,obs}$ and $DM_{\rm tot}$ distributions with the corresponding observed quantities from Parkes is considerably better for an intermediate value of peak redshift $z_{\rm crit} \approx 2.0$ with $\gamma_i(z_{\rm crit} = 2.0) > \gamma_i(z_{\rm crit} = 1.0) > \gamma_i(z_{\rm crit} = 3.0)$ for $i = w_{\rm obs},\ S_{\rm peak,obs},\ DM_{\rm tot}$ and most of the cases considered. Therefore, the FRB spatial density is expected to peak at a redshift similar to that of the cosmic SFH distribution.

Moreover, for the fixed $z_{\rm crit}$ and varying (α_l,α_u) case, we find that the observed $w_{\rm obs}$ from Parkes can be better explained with a FRB spatial density that gradually decreases with the source distance as $\gamma[(\alpha_l, \alpha_u) = (0, -3)] > \gamma[(\alpha_l, \alpha_u) = (0, 0)] > \gamma[(\alpha_l, \alpha_u) = (3, 0)]$. While $S_{\rm peak,obs}$ does not show a clear dependence on the PL $n(z)$ indices (α_l,α_u) for a fixed $z_{\rm crit}$, a FRB spatial density falling off sharply at large distances is preferred by the current $DM_{\rm tot}$ distribution with the likelihood order for PL indices (α_l,α_u) being $(0, -3) \gtrsim (0, 0) > (3, 0)$.

Combining the results from the fixed (α_l,α_u) and fixed $z_{\rm crit}$ cases for PL $n(z)$ obtained here with those for SFH $n(z)$ in Section 3.3.1, we find that the FRB spatial density is likely to be a PL distribution with a peak around the redshift $z_{\rm crit} \sim 2.0$. The reasonable agreement of the burst parameters with the observed FRB population at Parkes for SFH $n(z)$ also suggests PL indices $\alpha_l \approx 3.0$ and $\alpha_u \approx -3.0$ at asymptotically low and high redshifts, respectively. Here we have

further constrained the decreasing FRB spatial densities at large distances to obtain an upper PL index $\alpha_u \sim -3.0$.

Therefore, it is likely that the PL indices for the FRB spatial density are $\alpha_l \sim 0 - 3$ and $\alpha_u \approx -3$ with the distribution peaking at slightly larger redshifts compared to the cosmic SFH. Similar to the non-repeating FRBs, we also compare the simulated $S_{\rm peak,obs}$ and $\mathcal{F}_{\rm obs}$ distributions of the repeating FRB 121102 sub-bursts with the Arecibo observations. The corresponding results are shown in Figure 3.7 and the p-values listed in Table 3.2 in the next section.

3.3.3 Simulation results for repeating FRB 121102

Here we discuss the simulation results for the sub-bursts of the repeating FRB 121102 in order to better constrain the spectral properties of this source. In Figure 3.7, we show the results for the simulated $S_{\rm peak,obs}$ and $\mathcal{F}_{\rm obs}$ distributions of the repeating bursts and further compare them with the Arecibo observations at $\nu_{\rm obs} = 1.4$ GHz. We fix the host galaxy DM contribution relative to MW β and the spatial density $n(z)$ model for all the simulations as the source redshift and the individual DM components ($DM_{\rm IGM}$, $DM_{\rm MW}$ and $DM_{\rm host}$) along the line of sight are both well known for FRB 121102.

We only show the simulation results for intrinsic model w1L1 in Figure 3.7 as the relative difference between the intrinsic models is found to be statistically negligible (see Section 4). For the power-law model $L_{\rm int}$ distributions of FRB121102, we use $L_{\rm min} = 10^{41}$ erg/s and $L_{\rm min} = 10^{43}$ erg/s. We consider the value of the energy spectral index α to be varying within the range of -5.0 to 3.0, as supported by the current radio observations.

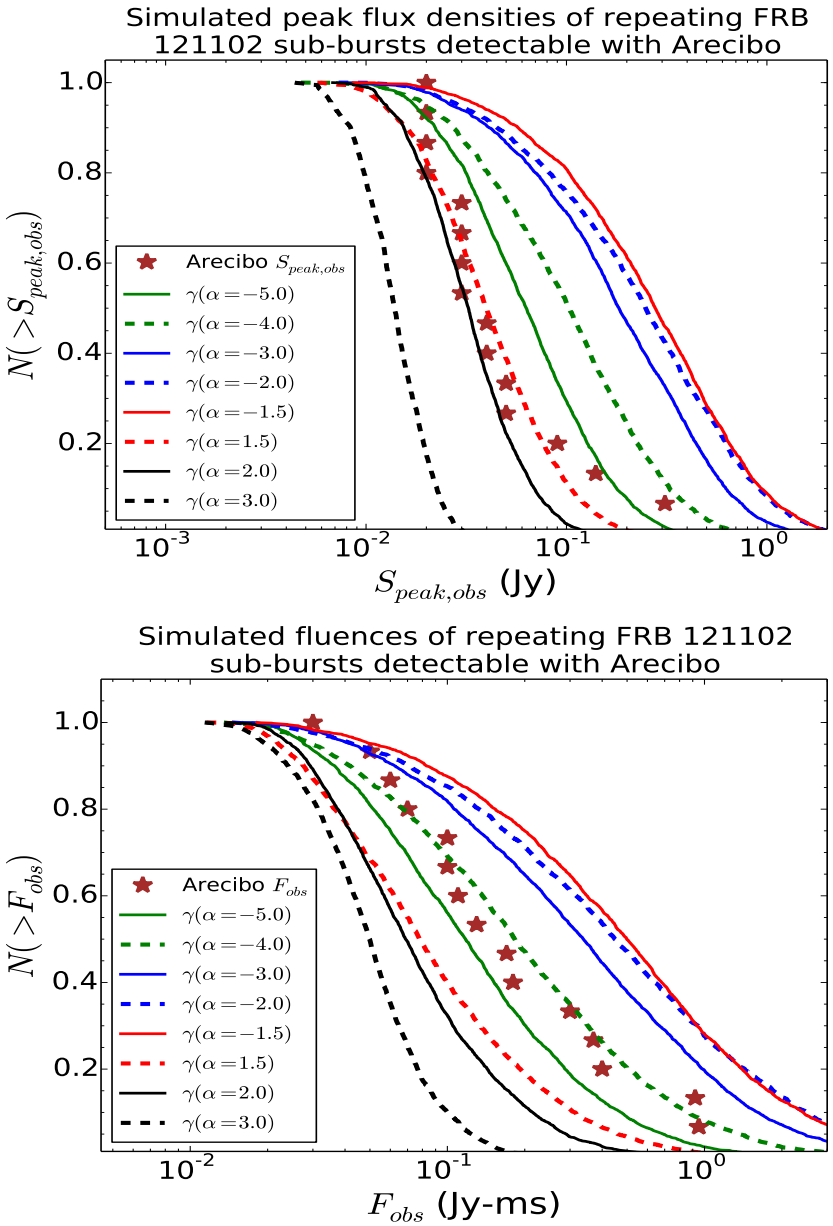

Figure 3.7: Comparison of repeating FRB sub-bursts detected by Arecibo at observing frequency $\nu_{\rm obs} = 1.4$ GHz and simulated $S_{\rm peak,obs}$ and $\mathcal{F}_{\rm obs}$ for FRB 121102 with different spectral indices. In both the panels, the MC simulation results are shown for α values ranging from -5.0 to 3.0. While β and $n(z)$ are fixed for the simulations of repeating FRB 121102, we only show the simulation results for intrinsic width and luminosity model w1L1 and scattering model 2. *Top panel:* Simulation results for $S_{\rm peak,obs}$ and different α, *Bottom panel:* Simulation results for $\mathcal{F}_{\rm obs}$ and different α.

Table 3.2: KS test p-values from the comparison of simulated $S_{\rm peak,obs}$ and $\mathcal{F}_{\rm obs}$ with the observed repeating FRB 121102 sub-bursts detected at Arecibo with $\nu_{\rm obs} = 1.4$ GHz. The p-values are obtained for a fixed β and $n(z)$ with $\gamma_{\rm eq} = \sqrt{\gamma^2_{S_{\rm peak,obs}} + \gamma^2_{\mathcal{F}_{\rm obs}}}$, and are listed for intrinsic width and luminosity models w1L1/w1L2/w2L1/w2L2 for each entry. All simulations are performed for scattering model 2 as the difference between the intrinsic distributions is found to be insignificant between the two scattering models (see Section 2).

α	$\gamma_{S_{\rm peak,obs}}$	$\gamma_{F_{\rm obs}}$	$\gamma_{\rm eq}$
-5.0	0.012/0.010/	0.721/0.573/	0.510/0.405/
	0.016/0.011	0.663/0.628	0.469/0.444
-4.0	$1.697 \times 10^{-4}/1.476 \times 10^{-4}$/	0.683/0.760/	0.483/0.537/
	$3.034 \times 10^{-4}/1.297 \times 10^{-4}$	0.782/0.699	0.553/0.494
-3.0	$1.278 \times 10^{-6}/1.242 \times 10^{-6}$/	0.044/0.053/	0.031/0.037/
	$7.717 \times 10^{-7}/9.317 \times 10^{-7}$	0.055/0.047	0.039/0.033
-2.0	$4.974 \times 10^{-7}/4.620 \times 10^{-7}$/	0.011/0.010/	0.008/0.007/
	$7.388 \times 10^{-7}/5.595 \times 10^{-7}$	0.014/0.011	0.010/0.008
-1.5	$1.281 \times 10^{-7}/1.850 \times 10^{-7}$/	0.004/0.007/	0.003/0.005/
	$1.517 \times 10^{-7}/1.878 \times 10^{-7}$	0.005/0.005	0.004/0.004
1.5	0.625/0.676/	0.056/0.077/	0.444/0.481/
	0.681/0.643	0.042/0.050	0.482/0.456
2.0	0.465/0.391/	0.009/0.007/	0.329/0.277/
	0.483/0.423	0.006/0.007	0.342/0.299
3.0	$6.796 \times 10^{-8}/1.036 \times 10^{-7}$/	$5.075 \times 10^{-6}/5.970 \times 10^{-6}$/	$3.589 \times 10^{-6}/4.222 \times 10^{-6}$/
	$6.112 \times 10^{-8}/8.332 \times 10^{-8}$	$4.251 \times 10^{-6}/6.560 \times 10^{-6}$	$3.006 \times 10^{-6}/4.639 \times 10^{-6}$

As $z = 0.19273$ is fixed for all the FRB 121102 bursts, the distribution for $L_{\rm obs}/E_{\rm obs}$ is essentially the same as that for $S_{\rm peak,obs}/\mathcal{F}_{\rm obs}$ while the $DM_{\rm tot}$ is fixed. This reduces the number of independent parameters among the observed/inferred quantities to only two, and here we consider $S_{\rm peak,obs}$ and $\mathcal{F}_{\rm obs}$ as the independent parameters for our analysis. Table 3.2 lists the p-values from the comparison of the simulated $S_{\rm peak,obs}$ and $\mathcal{F}_{\rm obs}$ with the Arecibo $\nu_{\rm obs} = 1.4$ GHz population for intrinsic model w1L1/w1L2/w2L1/w2L2. The KS test equivalent p-value is obtained from the two observable parameters as $\gamma_{\rm eq} = \sqrt{\gamma^2_{S_{\rm peak,obs}} + \gamma^2_{\mathcal{F}_{\rm obs}}}$.

We find that the observed $S_{\rm peak,obs}$ for FRB 121102 bursts detected by Arecibo agree better with the simulated $S_{\rm peak,obs}$ results for moderately positive energy spectral indices, especially $\alpha \sim 1.0 - 2.0$. However, the observed $\mathcal{F}_{\rm obs}$ for the Arecibo bursts implies an energy density spectrum that decreases sharply with increasing energy for FRB 121102. The $\gamma_{\rm eq}$ values obtained for FRB 121102 suggest either a large negative $\alpha \sim -5.0$ to -4.0 or moderately positive $\alpha \sim 1.0 - 2.0$ for this repeating FRB. As a result, it is very unlikely that the repeating FRB 121102 has a flat energy spectrum across its entire emission range and its spectrum is expected to be better constrained in the future once more bursts are detected by Arecibo at $\nu_{\rm obs} = 1.4$ GHz and their spectral information are available.

Chapter 4

FRB population and repeatability

In the previous Chapter, we constrained the FRB host galaxy dispersion measure, spectral index of the energy density, spatial distribution of the bursts and also the scattering due to turbulence in the intervening IGM and ISM using the observations for non-repeating and repeating bursts from Parkes and Arecibo telescopes, respectively. We showed that the FRB host galaxy DM contribution is expected to be similar to that from the Milky Way for typical sightlines and that a large negative spectral index ~ -2.0 for the FRB energy density is favoured by the current radio observations. Furthermore, the spatial density of FRB sources is expected to be a power-law distribution gradually increasing up to $z \sim 2$ and then falling off significantly at larger distances with an index ~ -3.

Now we use the follow-up data for FRBs in order to investigate whether FRB 121102 is representative of all FRBs repeating with a universal energy distribution function (EDF). The energy distribution for the repeating FRB 121102 sub-bursts does not exhibit any significant overlap with that of the reported non-repeating bursts (see Figure 4.1 for a distribution of energies). In fact, the typical energy output from most non-repeating sources is about 2-3 orders of magnitude greater as compared to the repeating FRB 121102.

Even though most FRBs have been extensively followed up with dedicated surveys ranging from few hours to ~ 1000 hrs, only few of the other FRBs except

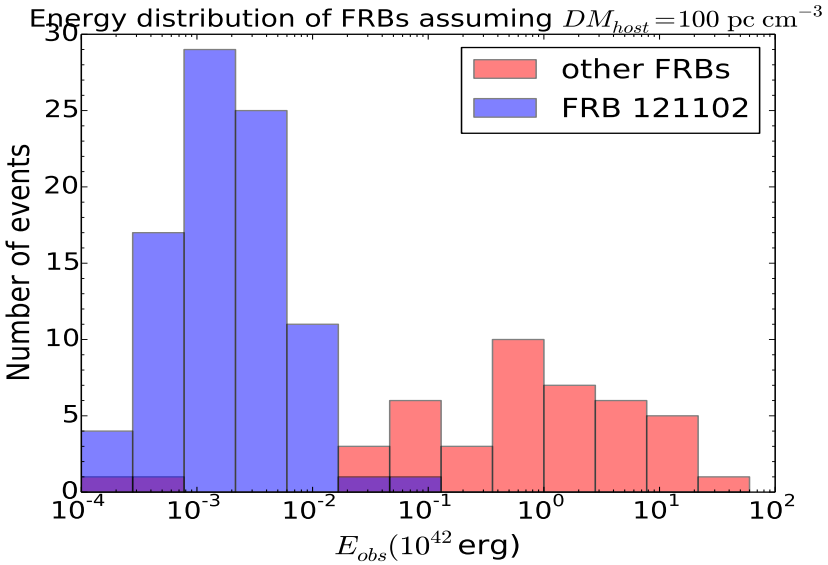

Figure 4.1: The distribution of inferred burst energies for repeating FRB 121102 and other non-repeating FRBs assuming fixed host galaxy DM contribution $DM_{\rm host} = 100$ pc cm^{-3}. The inferred energies of the 121102 sub-bursts are found to be significantly lower compared to the non-repeating FRBs during the active period.

FRB 180814.J0422+73 have been observed to be repeating. Table 4.1 lists the published follow-up observation data for the repeating FRB 121102 and 13 non-repeating Parkes FRBs from Table 6.1.

There can be two possible reasons for the repeating bursts from other FRBs to not get detected in spite of a universal repetitive behaviour for FRBs:

(a) the current observing times $t_{\rm obs}$ are smaller compared to the repeating timescale $t_{\rm rep}$ for the FRBs, or

(b) the repeating bursts from the other FRBs are very dim and cannot be detected with the typical sensitivities of the current telescopes.

4.1 FRB 121102 initial observations

Spitler et al. (2014) discovered the first FRB 121102 burst in a single-pulse search of archival data from the Arecibo PALFA survey and it was the only burst to be detected in a 180 second observation. The initial follow-up observations were carried out for a few hours for FRB 121102 but with no detection. The FRB was then extensively followed-up with Arecibo telescope in 2015 around the best known sky position, resulting in the discovery of ten additional bursts (Spitler et al. 2016) within three hours of observations - confirming it as the first repeating FRB source. Further multi-wavelength follow-up surveys found five bursts with GBT at 2 GHz and one with Arecibo at 1.4 GHz all with the same DM (Scholz et al. 2016), providing strong evidence that the bursts were originating from the same source.

Even though the FRB 121102 bursts appear to be clustered in time, there has not been any underlying periodicity detected yet. The power-law spectral index for the burst spectra is found to be varying within a large range between -10 to +14, suggesting variable properties that may be intrinsic to this particular source and not just propagation effects. The targeted interferometric localisation efforts for FRB 121102 with the Karl Jansky Very Large Array (VLA) and the Arecibo telescope simultaneously over 6 months detected nine additional bursts at 3 GHz and reported the first sub-arcsecond localisation (Chatterjee et al. 2017).

In addition, a persistent variable counterpart with a flux density $\sim$180 Jy was detected (Marcote et al., 2017) within a star-forming dwarf host galaxy at $z = 0.19273$ (Tendulkar et al., 2017). The host galaxy was found to be with low-metallicity and with a stellar mass of $(4-7)\times10^7\ M_\odot$. Thereafter, four additional

bursts were detected with the European very long baseline interferometric (VLBI) network at 5 GHz which showed that the physical separation between the FRB and radio source is less than ∼40 pc, hence confirming their association.

4.2 FRB energy distribution function

The Parkes sensitivity threshold at $\nu_{\rm obs} = 1.4$ GHz for $S/N = 9$ and an arbitrary $w_{\rm obs}$ is $S_{\rm th} = 0.36$ Jy $(w_{\rm obs}/1\ {\rm ms})^{-1/2}$ (Caleb et al., 2016). For pulse widths in the range $w_{\rm obs} \sim 1.00 - 8.00$ ms, $S_{\rm th}$ for Parkes varies within the range $\sim 0.1 - 0.4$ Jy. It should be noted that all the inferred energies in Table 6.1 are based on the lower limits for the fluence due to the uncertainty in the position of the source within a single beam and the assumption of on-axis detection for all bursts.

Since Parkes is less sensitive as compared to Arecibo, we only include the repeating FRB 121102 sub-bursts for which $S_{\rm peak,obs}$ exceeds the Parkes $S_{\rm th}$ for evaluating the repeater cumulative energy distribution (CED). Out of the 88 repeating bursts from FRB 121102 that we consider here, 65/55/46/21 bursts would have been above the Parkes $S_{\rm th} \sim 0.10/0.13/0.20/0.40$ Jy at $\nu_{\rm obs} = 1.4$ GHz. While computing the repeater CED for varying Parkes $S_{\rm th}$ values, we have ignored the effect of different observing frequencies for Parkes as compared to the FRB 121102 observations from Arecibo, GBT and Effelsberg.

The top panel of Figure 4.2 shows the chi-squared PL, exponential and gaussian (with zero mean) fits for the CED of FRB 121102 along with the $\dot{N}(> E_{\rm obs})$ upper limits for the non-repeating FRBs. While the repeating FRB CED is normalized with its total observing time $t_{\rm obs} = 235.7$ hr, the $\dot{N}(> E_{\rm obs,i})$ values

Table 4.1: The follow-up observation information for repeating FRB 121102 and non-repeating Parkes FRBs listed in Table 6.1. The redshift z and burst energy $E_{\rm obs}$ are inferred by assuming a fixed host galaxy DM contribution $DM_{\rm host} = 100$ pc cm^{-3}. None of the 13 listed FRBs were observed to repeat in spite of dedicated follow-up efforts ranging from few hours to ~ 1000 hours with Parkes. The follow-up observational data has been obtained from Keane et al. (2012), Thornton et al. (2013), Ravi et al. (2015), Petroff et al. (2015), Champion et al. (2016), Petroff et al. (2017) and Bhandari et al. (2018).

FRB	Telescope	$S_{\rm peak,obs}$ (Jy)	$\mathcal{F}_{\rm obs}$ (Jy ms)	z	$E_{\rm obs}$ (10^{42} erg)	$t_{\rm obs}$ (hr)
010621	Parkes	0.53	4.24	0.20	0.03	15.5
090625	Parkes	1.14	2.19	1.06	0.53	33.65
110220	Parkes	1.11	7.31	1.12	1.94	1.75
110626	Parkes	0.63	0.89	0.81	0.12	11.25
110703	Parkes	0.45	1.75	1.33	0.65	10.1
120127	Parkes	0.62	0.75	0.61	0.06	5.5
121002	Parkes	0.43	2.34	2.00	1.86	10.25
121102	Arecibo, GBT, Effelsberg †			0.19		235.7
130626	Parkes	0.74	1.47	1.09	0.37	9.5
130729	Parkes	0.22	3.43	1.01	0.75	10
131104	Parkes	1.16	2.75	0.85	0.43	78
140514	Parkes	0.47	1.32	0.62	0.11	19.2
150215	Parkes	0.70	2.02	0.82	0.28	17.5
151230	Parkes	0.42	1.90	1.13	0.52	54.9

† The follow-up data for the repeating FRB 121102 is obtained from Spitler et al. (2016), Scholz et al. (2016), Scholz et al. (2017), Law et al. (2017), Hardy et al. (2017),Michilli et al. (2018), Gajjar et al. (2018) and Spitler et al. (2018).

for the individual non-repeating FRBs are normalized as $\dot{N}(> E_{\rm obs,i}) = 1/t_{\rm obs,i}$, where $t_{\rm obs,i}$ is the observing time corresponding to the i-th burst (see Table 4.1). The best fit distribution for the CED of the repeating FRB is found to be: $\dot{N}_0 \exp(-E_{\rm obs}/E_0)$ with $(\dot{N}_0, E_0) = (0.283\ {\rm hr}^{-1}, 4.0 \times 10^{39}\ {\rm erg})/(0.247\ {\rm hr}^{-1}, 4.0 \times 10^{39}\ {\rm erg})/(0.210\ {\rm hr}^{-1}, 5.0 \times 10^{39}\ {\rm erg})/(0.090\ {\rm hr}^{-1}, 6.0 \times 10^{39}\ {\rm erg})$ for Parkes $S_{\rm th} = 0.10/0.13/0.20/0.40$ Jy.

4.3 Repetition probability

For each FRB, the threshold energy corresponding to a fluence completeness threshold $\mathcal{F}_{\rm th}$ is $E_{\rm th}(z_i) = 4\pi D^2(z_i)\mathcal{F}_{\rm th}(1+z_i)(\nu'_{\rm max} - \nu'_{\rm min})$. The average number of repeating events with energy $E \geq E_{\rm th}(z_i)$ within time $t_{\rm obs,i}$ for a burst at redshift z_i is

$$\begin{aligned}\overline{N}_{\rm rep,i} &= \frac{t_{\rm obs,i}}{(1+z_i)} \int_{E_{\rm th}(z_i)}^{\infty} \frac{\dot{N}_0}{E_0} \exp\left(-\frac{E_{\rm obs}}{E_0}\right) dE_{\rm obs} \\ &= \frac{\dot{N}_0\ t_{\rm obs,i}}{(1+z_i)} \exp\left[-\frac{E_{\rm th}(z_i)}{E_0}\right]. \end{aligned} \tag{4.1}$$

If all other FRBs repeat at the same rate $\dot{N}_0$ as FRB 121102, the probability of observing none of the detected bursts to be repeating for a given value of $\mathcal{F}_{\rm th}$ is

$$\begin{aligned}{\rm P}(\mathcal{F}_{th}) &= \prod_{i=1}^{13} \exp(-\overline{N}_{rep,i}) \\ &= \exp\left[-\sum_{i=1}^{13} \frac{\dot{N}_0\ t_{obs,i}}{(1+z_i)} \exp\left(-\frac{E_{th}(z_i)}{E_0}\right)\right] \end{aligned} \tag{4.2}$$

Here we assume a simplistic case of Poissonian distribution for the arrival times of the detected FRB 121102 sub-bursts. However, Oppermann et al. (2018) have shown earlier that the observed clustering of arrival times for the initial 17

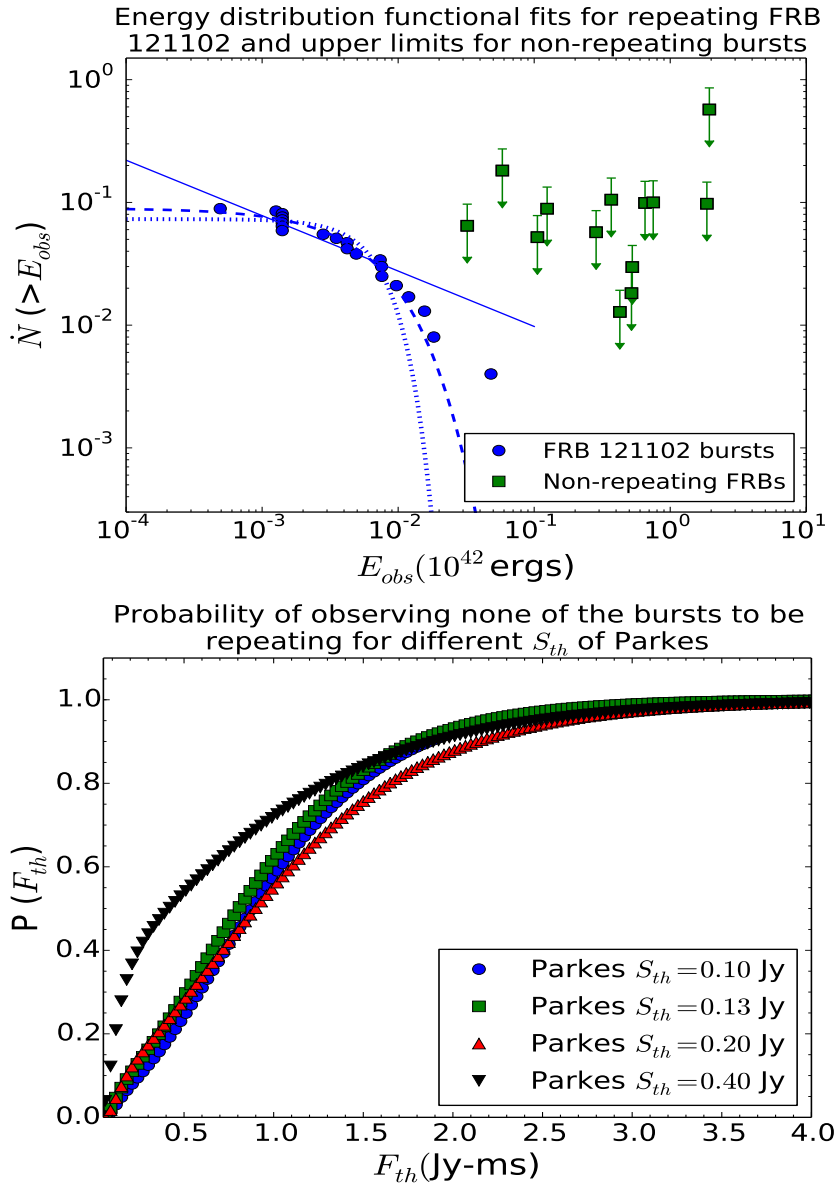

Figure 4.2: *Follow-up observations for the repeating FRB 121102 and the non-repeating FRBs: Top panel:* Power-law, exponential and gaussian fits for the CED of the repeating FRB 121102. The distribution for the repeater is normalized using its follow-up observing time $t_{\rm obs}$ = 235.7 hr. The upper limits for $\dot{N}(> E_{\rm obs})$ of the 13 non-repeating Parkes FRBs are also shown and are normalized using their respective $t_{\rm obs}$ values from Table 4.1, *Bottom panel:* The probability of observing none of the 13 non-repeating Parkes FRBs to be repeating as a function of the fluence threshold $\mathcal{F}_{\rm th}$ (see equation 4.2). The probability is computed for different sensitivities of Parkes $S_{\rm th} = 0.10, 0.13, 0.20, 0.40$ Jy.

sub-bursts from FRB 121102 (Spitler et al. 2016; Scholz et al. 2016) are better modelled with a Weibull distribution.

Although the mean repetition rates obtained from both Poisson and Weibull distributions are found to be similar, the probability of non-detection of bursts is much larger during a continuous observation for Weibull distribution of arrival times due to the clustering behaviour of the bursts. The estimates for the repetition rate are therefore expected to be less certain for the Weibull distribution. As a result, the upper limits on the non-repetition probability $\mathrm{P}(\mathcal{F}_{\rm th})$ are expected to be weaker than what we obtain for a Poissonian distribution here.

In the bottom panel of Figure 4.2, we show the variation of $\mathrm{P}(\mathcal{F}_{\rm th})$ within a range of $\mathcal{F}_{\rm th}$ for the 13 non-repeating FRBs with $t_{\rm obs,i}$ listed in Table 4.1. We evaluate the $\mathrm{P}(\mathcal{F}_{\rm th})$ curves from equation (4.2) for the $(\dot{N}_0, E_0)$ values corresponding to Parkes $S_{\rm th} = 0.10/0.13/0.20/0.40$ Jy. The fluence completeness threshold for the Parkes FRBs was derived to be $\mathcal{F}_{\rm th} \approx 2$ Jy ms by Keane & Petroff (2015). In order to obtain an approximate upper limit on $\mathrm{P}(\mathcal{F}_{\rm th})$, here we assume this fairly optimistic choice of $\mathcal{F}_{\rm th}$ for the non-localized FRBs in Table 4.1.

4.4 Is FRB 121102 representative?

We find that the probability of observing none of the 13 non-repeating FRBs that have been followed up with Parkes so far to be repeating lies within the range $\mathrm{P}(\mathcal{F}_{\rm th}) \approx 0.8 - 0.9$ for $\mathcal{F}_{\rm th} \approx 2$ Jy ms and Parkes $S_{\rm th} \sim 0.1 - 0.4$ Jy. The sensitivity threshold range corresponds to the range of observed FRBs at Parkes with $w_{\rm obs} \sim 1.0 - 8.0$. While the actual experimental thresholds might be somewhat different, the qualitative analysis will not change.

The probability that we obtain for observing none of the Parkes FRBs to be repeating is significantly larger than the probability $\sim 0.05 - 0.3$ obtained by Bhattacharya et al. (2019) for a smaller sample size and further supports repeating FRB as being representative of the entire FRB population. Although the follow-up observing times $t_{\rm obs,i}$ have increased for the non-repeating FRBs now, the exponential EDF for the repeating FRB coupled to the difference in the mean $E_{\rm obs}$ for the non-repeating and repeating FRBs by almost three orders of magnitude (see Figure 4.1) implies that the other FRBs need to be followed up for significantly longer before concluding in favour of distinct FRB populations.

It should however be noted that $t_{\rm obs,i}$ for the FRBs are spread over different telescopes with a range of observing frequencies and sensitivities, and a more rigorous analysis regarding the repeatability of the FRBs would involve using a uniform sample which is possible once more bursts are followed up in the future. In addition to the repetition rate, the complex time-frequency sub-structures found in pulses from both FRB 121102 and FRB 180814.J0422+73 may provide constraints on the source emission mechanism. With the rapid observational progress using the high-resolution CHIME telescope, it will soon be clear whether repeaters originate from a separate class of progenitors as compared to non-repeating FRBs.

Chapter 5

FRB spatial density from observed flux distribution

Although several progenitor models involving both cataclysmic and non-cataclysmic scenarios have already been proposed for FRBs (see Platts et al. (2018), for a recent review), the nature of FRBs and their sources still remains a mystery. This is primarily due to the sparse spatial localisation of several arcminutes for most of the current radio surveys, which makes the identification of the FRB host galaxy and its association with other electromagnetic counterparts challenging. However, the distributions of FRB observables such as the flux density and fluence helps us to statistically constrain the properties of the FRB progenitors as they are linked to the source luminosity function as well as the evolutionary history of the cosmic rate density (Bera et al., 2016; Caleb et al., 2016; Oppermann et al., 2016; Vedantham et al., 2016; Macquart & Ekers 2018; Niino 2018; Bhattacharya 2019).

The distribution of the observed flux density is mainly affected by the pulse temporal broadening due to multipath propagation and the finite temporal resolution of the detection instrument. In this Chapter, we investigate how the statistical properties of the apparent flux density can be used to constrain the luminosity and spatial density distributions of the FRB progenitors for events detected specifically with Parkes. We consider the effects of the telescope beam shape and temporal resolution on the observed flux distribution in addition to the

pulse propagation effects. Due to the rapidly evolving nature of this field, we only consider the FRBs published until February 2019 with resolved intrinsic width and total $DM \geq 500$ pc cm^{-3} for our analysis here (see Table 1 of Bhattacharya et al. 2019 for the data sample). We assume fiducial values for cosmological parameters with $H_0 = 68$ km s^{-1}Mpc^{-1}, $\Omega_m = 0.27$ and $\Omega_\Lambda = 0.73$ (Planck Collaboration et al., 2014).

In Section 5.1, we estimate the FRB distances and flux densities assuming specific host galaxy properties and scattering model for pulse temporal broadening. In Section 5.2, we obtain the flux density distribution for a given FRB spatial density and luminosity distribution to compare it with the current observations. We then perform Monte Carlo (MC) simulations to study the effect of telescope observing biases, source energy density function and host galaxy properties on the observed flux distribution in Section 5.3. We conclude with a summary of our results in Section 5.4.

5.1 FRB distance and flux estimates

The inferred FRB distances are based on the uncertain host galaxy properties and the source location inside it, with a larger uncertainty in z expected for a larger host galaxy DM contribution ($DM_{\rm host}$) to the total DM ($DM_{\rm tot}$). In order to minimize the uncertainty from $DM_{\rm host}$, we place a lower $DM_{\rm tot}$ cutoff on the observed sample considered in this study. The total DM for a given FRB line of sight is

$$DM_{tot} = DM_{\rm MW} + \frac{DM_{\rm host}}{(1+z)} + DM_{\rm IGM,0} \int_0^z \frac{(1+z')dz'}{\sqrt{(1+z')^3 + 2.7}} \qquad (5.1)$$

where $DM_{\rm MW}$ is the Milky Way (MW) ISM contribution obtained from the NE2001 model (Cordes & Lazio 2002) and the IGM DM contribution ($DM_{\rm IGM}$) is given by the integral over z with $DM_{\rm IGM,0} = 1294.9$ pc cm^{-3}. We have assumed the baryonic mass fraction in the IGM $f_{IGM} = 0.83$, free electron number density $n_e(z) = 2.1 \times 10^{-7}(1+z)^3$ cm^{-3} and the ionization fraction $x(z) \approx 7/8$ (Ioka 2003; Inoue 2004; Deng & Zhang 2014).

As the type of the host galaxy, location of the FRB source within its galaxy and our viewing angle relative to the host galaxy are all fairly uncertain, we assume a fixed contribution $DM_{\rm host} \approx 100$ pc cm^{-3} that is comparable to the typical $DM_{\rm MW}$ contribution for most lines of sight. The inferred redshift is then obtained directly from equation (5.1) for a given burst and the corresponding comoving distance to the source is $D(z) = (8.49 \text{ Gpc}) \int_0^z [(1+z')^3 + 2.7]^{-0.5} dz'$. For a typical uncertainty $\Delta DM_{\rm host} \sim DM_{\rm host} \approx 100$ pc cm^{-3} and $DM_{\rm IGM} \approx 750z$ pc cm^{-3}, the corresponding error in the inferred redshift is $\Delta z \approx 0.2/(1+z)$ assuming $\Delta z \sim z \sim 1$ for most FRBs in our sample.

The intrinsic width of a FRB pulse can be written in terms of the observed width $w_{\rm obs}$ and other width components as $w_{\rm int}^2 = [w_{\rm obs}^2 - (w_{\rm DM}^2 + w_{\rm samp}^2 + w_{\rm sc}^2)]/(1+z)^2$. Here, $w_{\rm DM}$ is the dispersive smearing across frequency channels, $w_{\rm samp}$ is the observation sampling time and $w_{\rm sc}^2 = w_{\rm IGM}^2 + w_{\rm ISM,MW}^2 + (1+z)^2 w_{\rm ISM,host}^2$ is the pulse scatter broadening across the diffused IGM and ISM components. The scatter broadening in the host galaxy/MW ISM is given by Krishnakumar et al. (2015) as

$$w_{\rm ISM} = w_{\rm ISM,0} F (1.0 + 1.94 \times 10^{-3} DM_{\rm ISM}^{2.0}) \frac{DM_{\rm ISM}^{2.2}}{\nu_{0,GHz}^{4.4}} \tag{5.2}$$

where $DM_{\rm ISM} = DM_{\rm host/MW}$ is the respective ISM DM component, $w_{\rm ISM,0} =$

4.1×10^{-8} ms, $\nu_{0,GHz} = \nu_0/10^3$ is the central frequency in GHz and $F = 4f(1-f)$ is the geometrical lever-arm factor with $f = 25$ kpc$/[(1+z)D(z)]$ (Williamson 1972; Vandenberg 1976). The pulse broadening due to IGM turbulence from Macquart & Koay (2013) is

$$w_{IGM}(z) = \frac{k_{IGM}}{\nu_{0,GHz}^4 Z_L} \int_0^z dz' d(z') \int_0^z dz' d(z')(1+z')^3 \tag{5.3}$$

where $k_{IGM} = 2.94 \times 10^{12}$ ms MHz^4 is a normalisation factor, $d(z') = [\Omega_m(1+z')^3 + \Omega_\Lambda]^{-1/2}$ and $Z_L = (1+z)^2 \left[(1+z) - \sqrt{z(1+z)}\right]^{-1}$.

As the value of $w_{\rm sc}$ from equations (5.2) and (5.3) is significantly smaller compared to $w_{\rm obs}$ and $w_{\rm DM}$ (see Bhattacharya et al. (2019)), we have $\Delta w_{\rm int}/w_{\rm int} = 0.2/(1+z)^2$. We find the best-fit cumulative $w_{\rm int}$ distribution to be: $N(> w_{\rm int}) = 25.24 \exp(-w_{\rm int}/2.092$ ms). Although the value of $k_{\rm IGM}$ is fixed using the width parameters of a particular FRB, $w_{\rm int}$ has a weak dependence on the constant $k_{\rm IGM}$ as $w_{\rm sc} \lesssim 10^{-2} w_{\rm int}$.

The flux density is reduced due to the pulse broadening from multipath propagation and can be written in terms of the observable fluence $\mathcal{F}_{\rm obs}$ as $S_{\rm peak} = \mathcal{F}_{\rm obs}/w_{\rm int}$. The distribution of observed and intrinsic peak flux density distributions for non-repeating FRBs is shown in Figure 5.1. Moreover, for a Gaussian telescope beam profile the observed flux density is further reduced with $S_{\rm peak,obs} \approx S_{\rm peak} \exp(-r'^2/r_{\rm beam}^2)$, where r' is the radial distance from the center of the beam with radius $r_{\rm beam}$. The bolometric luminosity is obtained for a power-law FRB energy distribution to be (Lorimer et al., 2013)

$$L = \frac{4\pi D^2(z)(\nu'^{\alpha+1}_{\rm max} - \nu'^{\alpha+1}_{\rm min})(\nu_2 - \nu_1)}{(1+z)^{\alpha-1}(\nu_2^{\alpha+1} - \nu_1^{\alpha+1})} S_{\rm peak} \tag{5.4}$$

where α is the spectral index of the energy distribution, (ν'_{min}, ν'_{max}) is frequency range for source emission in the comoving frame and (ν_1, ν_2) is the observing band

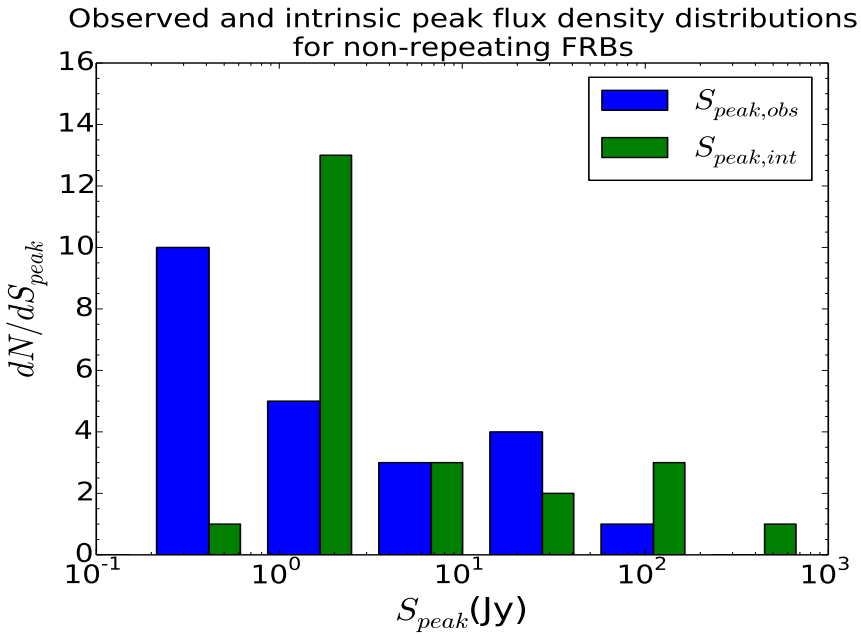

Figure 5.1: Distribution of observed and intrinsic peak flux density distributions for non-repeating FRBs.

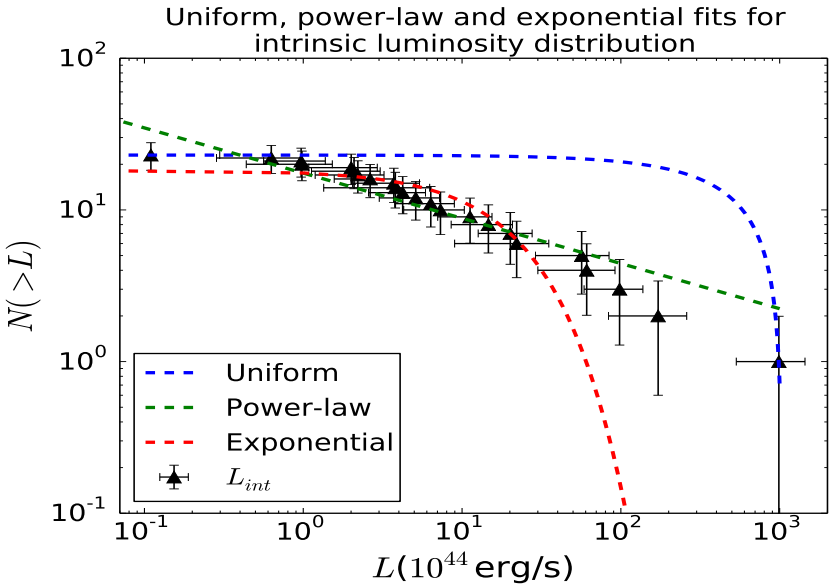

Figure 5.2: *Chi-squared fits for the cumulative distribution of the inferred luminosities:* L values are obtained from equation (5.4) and vary from 1.1×10^{43} erg/s to 1.0×10^{47} erg/s with the best fit: $23.0 - 0.0223\ L$ uniform, $17.489\ L^{-0.298}$ power-law and $18.395\ \exp(-L/20.741 \times 10^{44}$ erg/s) exponential distributions.

frequency range. As the emission spectral indices are poorly constrained from the current observations, we assume $\alpha \approx 0$, $\nu'_{min} = 600$ MHz and $\nu'_{max} = 8$ GHz for our analysis here. As $D(z) \propto z$, the relative uncertainty in the inferred luminosity is $\Delta L/L = \sqrt{(\Delta S_{\rm peak}/S_{\rm peak})^2 + 4(\Delta z/z)^2}$.

Figure 6.1 shows the chi-squared fits for the uniform, power-law and exponential cumulative distributions of the inferred FRB luminosities from equation (5.4). We find that the luminosity varies considerably by almost four orders of magnitude from $\sim 10^{43}$ erg/s to $\sim 10^{47}$ erg/s for our sample. We include the uncertainties ΔL as the x-error bars along with the Poisson fluctuations as errors in the y-coordinate to obtain the chi-squared fits. While we find that both the power-law (PL) distribution $\propto L^{-0.298}$ and the exponential distribution $\propto \exp(-L/L_{\rm c})$ with cutoff $L_{\rm c} \approx 20.741$ erg/s fit the inferred luminosity fairly well, the former explains the relative over-abundance of non-repeating FRBs with very large inferred luminosities $\gtrsim 10^{46}$ erg/s better.

5.2 Observed flux distribution

For a population of FRB sources distributed within a distance $R_{\rm min}$ to $R_{\rm max}$, the number of sources with luminosity L having peak flux density larger than some $S_{\rm peak}$ are

$$\frac{dN}{dL} = \begin{cases} \int_{R_{min}}^{D_L} \dfrac{n(z,L)}{1+z} 4\pi D^2 dD, \;\; R_{\rm min}^2 < L/4\pi S_{\rm peak} < R_{\rm max}^2 \\ \int_{R_{min}}^{R_{max}} \dfrac{n(z,L)}{1+z} 4\pi D^2 dD, \;\; L/4\pi S_{\rm peak} > R_{\rm max}^2 \end{cases} \tag{5.5}$$

where $D_L = \sqrt{L/4\pi S_{\rm peak}}$ and we assume that $n(z, L) = \rho(z)g(L)$ is independent of $w_{\rm int}$. Here $g(L)$ is the luminosity distribution of the FRB source and $\rho(z)$ is

Table 5.1: Polynomial approximations for $N(> S_{\rm peak})$ distributions obtained from equation (5.6) for various distributions of FRB source luminosity function $g(L)$ and spatial density $\rho(z)$. We define $\xi = L_{\rm min}/L_{\rm mid}$, $R_{\rm min} = (1.114\ {\rm Gpc})S_{\rm peak}^{-1/2}$, $R_{\rm mid} = (7.598\ {\rm Gpc})S_{\rm peak}^{-1/2}$, $F_{\rm SFH,PL}(x) = 2.03 + 4.96x - 0.874x^2 + 0.131x^3 - 0.00663x^4$, $F_{\rm SMD,PL}(x) = 6.54 + 0.0155x + 0.950x^2 + 0.143x^3 - 0.0517x^4$.

$\rho(z)$	$g(L) = 1/(L_{\rm mid} - L_{\rm min})$
$\rho_{\rm NE}(z)$	$\propto S_{\rm peak}^{-3/2}(1-\xi^{5/2})$
$\rho_{\rm SFH}(z)$	$\propto [-0.606(1-\xi) + 0.668R_{\rm mid}(1-\xi^{3/2}) - 0.307R_{\rm mid}^2(1-\xi^2)$ $+0.0632R_{\rm mid}^3(1-\xi^{5/2}) - 0.00376R_{\rm mid}^4(1-\xi^3)]$
$\rho_{\rm SMD}(z)$	$\propto [-1.95(1-\xi) + 0.00208R_{\rm mid}(1-\xi^{3/2}) + 0.334R_{\rm mid}^2(1-\xi^2)$ $+0.0688R_{\rm mid}^3(1-\xi^{5/2}) - 0.0293R_{\rm mid}^4(1-\xi^3)]$
$\rho(z)$	$g(L) \propto L^{-1.298}$
$\rho_{\rm NE}(z)$	$\propto S_{\rm peak}^{-0.298}(1 - 0.00406/S_{\rm peak}^{1.202})$
$\rho_{\rm SFH}(z)$	$\propto [S_{\rm peak}^{-0.298}F_{\rm SFH,PL}(R_{\rm max}) - 3.92F_{\rm SFH,PL}(R_{\rm min})]$
$\rho_{\rm SMD}(z)$	$\propto [S_{\rm peak}^{-0.298}F_{\rm SMD,PL}(R_{\rm max}) - 3.92F_{\rm SMD,PL}(R_{\rm min})]$

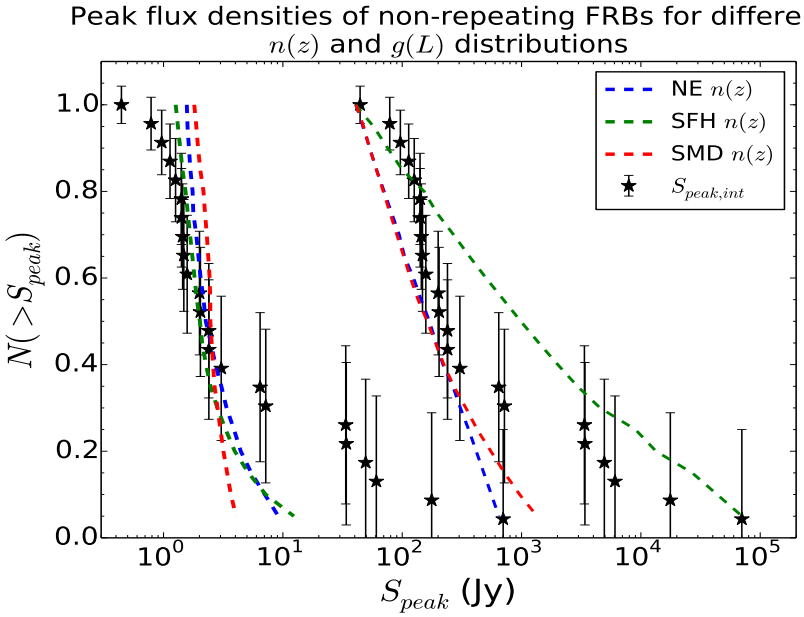

Figure 5.3: *Comparison of intrinsic* $S_{\rm peak} = \mathcal{F}_{\rm obs}/w_{\rm int}$ *distribution with that obtained for different* $g(L)$ *and* $\rho(z)$ *models:* $N(> S_{\rm peak})$ distributions obtained from equation (5.6) for uniform/power-law $g(L)$ and NE/SFH/SMD $\rho(z)$ are shown here. The $S_{\rm peak}$ values for the bursts are scaled up from their actual values by a factor of 100 for the power-law $g(L)$ to avoid overlap.

the spatial density distribution of the FRB progenitors.

As FRBs with relatively small $DM_{\rm tot} \sim 100$ pc cm^{-3} have already been reported, here we set $R_{\rm min} = 0$ and $R_{\rm max} \approx 11$ Gpc such that $R_{\rm max} \geq (L/4\pi S_{\rm peak})^{1/2}$ holds for all the FRBs in our data sample. This further gives the source count to be

$$N(> S_{\rm peak}) = 4\pi \int_0^{4\pi R_{\rm max}^2 S_{\rm peak}} g(L) dL \int_0^{D_L} \frac{\rho(z)}{1+z} D^2 dD \tag{5.6}$$

where $N(> S_{\rm peak})$ is directly determined from the observations with $g(L)$ and $\rho(z)$ decided by the nature of the FRB progenitor.

We consider uniform $g(L) \propto 1/(L_{\rm mid} - L_{\rm min})$ and power-law $g(L) \propto L^{-1.298}$

distributions, where $L_{\rm min} = 1.1 \times 10^{43}$ erg/s and $L_{\rm mid} = 5.1 \times 10^{44}$ erg/s are the minimum and median inferred luminosities from our sample.

For the spatial density $\rho(z)$, we consider three different models:
(a) non-evolving population $\rho_{\rm NE}(z)$ of FRB progenitors,
(b) spatial density tracking the star formation history (SFH) $\rho_{\rm SFH}(z)$,
(c) spatial density tracking the stellar mass density (SMD) $\rho_{\rm SMD}(z)$.
We use the formulations of cosmic SFH and SMD given by Madau & Dickinson (2014),

$$\rho_{\rm SFH}(z) = \psi(z) = \rho_{\rm SFH,0} \frac{(1+z)^{2.7}}{1 + [(1+z)/2.9]^{5.6}} \tag{5.7}$$

$$\rho_{\rm SMD}(z) = \rho_{\rm SMD,0} \int_z^\infty \psi(z') \frac{d(z')dz'}{H_0(1+z')} \tag{5.8}$$

where $\rho_{\rm SFH,0} = 0.015\ M_\odot\ {\rm year}^{-1}\ {\rm Mpc}^{-3}$ and $\rho_{\rm SMD,0} = 0.73$ are the normalisation constants. While $\rho(z)$ is expected to follow $\rho_{\rm SFH}(z)$ if FRBs arise from relatively young population of stars, the spatial density should trace $\rho_{\rm SMD}(z)$ if FRB progenitors were to be older stars.

Table 6.1 lists the closest polynomial approximations for the cumulative flux distributions obtained for the two source luminosity functions and the three FRB spatial density models considered here. In Figure 6.2, we show the comparison of the intrinsic $S_{\rm peak} = \mathcal{F}_{\rm obs}/w_{\rm int}$ obtained in Section 5.1 with that computed from equation (5.6) for the different $g(L)$ and $\rho(z)$ models used here. The p-values from the Kolmogorov Smirnov (KS) test comparison between the distributions are listed in Table B.1. We find that the distribution of intrinsic $S_{\rm peak}$ is better explained by a young population of FRB progenitors with $\rho(z) \propto \rho_{\rm SFH}$, especially

for a uniform $g(L)$. While the $\rho_{\rm NE}$ and $\rho_{\rm SMD}$ spatial densities can be ruled out for uniform $g(L)$, all three $\rho(z)$ distributions explain the flux density values in case of a power-law $g(L)$ fairly well.

5.3 Observing biases

We evaluated $N(> S_{\rm peak})$ for given $g(L)$ and $\rho(z)$ models in Section 5.2, and also obtained the width distribution $N(> w_{\rm int}) = 25.24\ \exp(-w_{\rm int}/2.092\ {\rm ms})$ in Section 5.1. However, the pulse width distribution is directly affected by the temporal resolution of the telescope as a coarse time resolution makes it harder to detect a pulse with smaller $w_{\rm obs}$ due to the instrumental noise. Furthermore, there is an observing bias against bursts that are smeared over larger $w_{\rm obs}$ and/or have larger $w_{\rm int}$, as the instrument sensitivity decreases gradually with increasing $w_{\rm obs}$. In addition to the instrument temporal resolution, the observed flux distribution is also affected by the beam shape of the telescope used for the event detection.

To include the effect of these observing biases on $N(> S_{\rm peak})$, we perform MC simulations to obtain the flux distribution (see Section 3.2 of Bhattacharya et al. (2019) for a detailed code algorithm).

From the known $N(> w_{\rm int})$, $g(L)$ and $\rho(z)$ distributions, we generate a population of 1000 FRBs that can be detected at the Parkes multibeam (MB) receiver with a signal-to-noise ratio $S/N \geq 9$. The Parkes MB receiver has 13 beams with beam radii $r_{beam} = 7.0'$ $(7.05')$ $[7.25']$ and beam center gains $G_{beam} = 0.731$ (0.690) [0.581] K Jy^{-1} for beam 1 (2-7) [8-13] (see Staveley-Smith et al., (1996) for the system parameters).

As the FRB source location within its host galaxy is highly uncertain, we

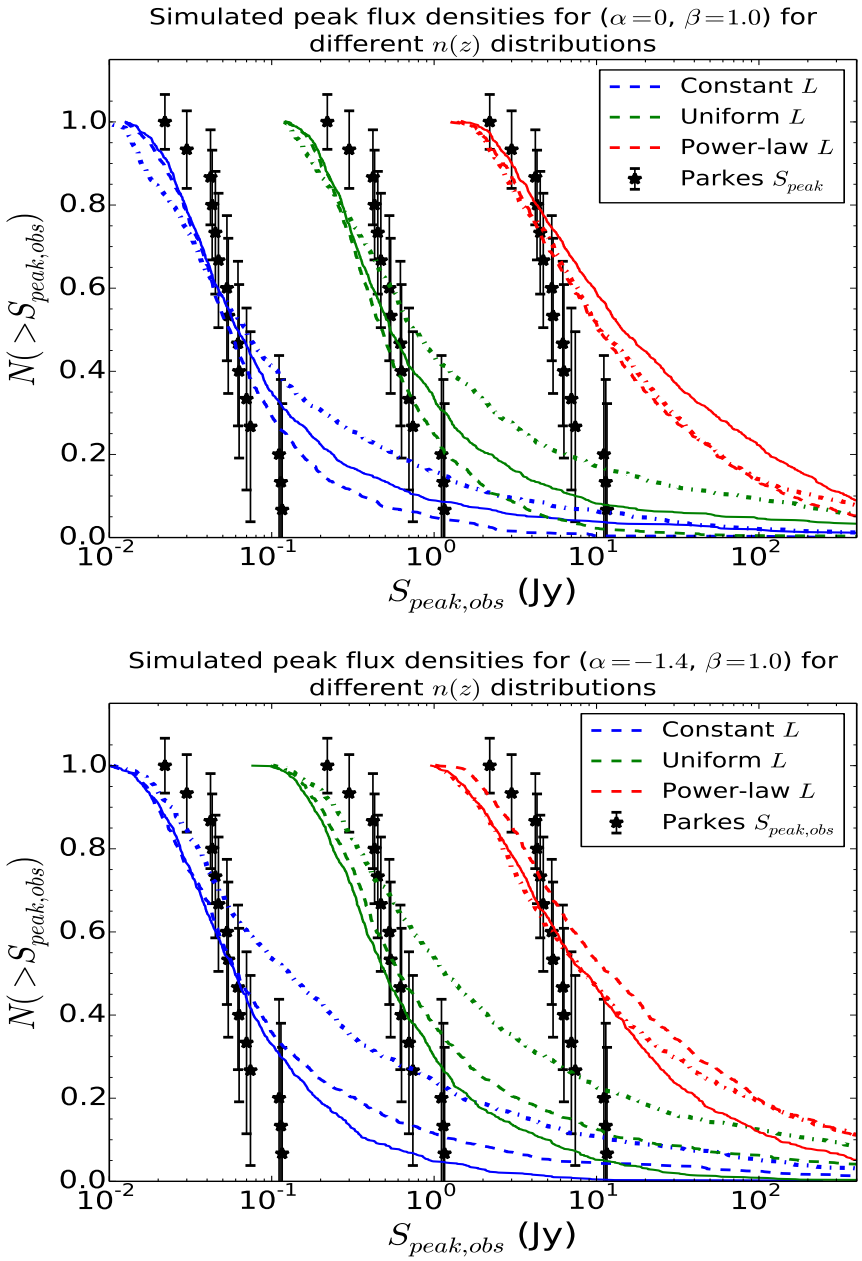

Figure 5.4: *Comparison of observed Parkes $S_{\rm peak}$ with simulated $S_{\rm peak}$ distributions for different $g(L)$ and $\rho(z)$ models, $\alpha = 0, -1.4$ and $\beta = 1.0$:* Simulated $N(> S_{\rm peak,obs})$ distributions for constant/uniform/power-law $g(L)$ and NE/SFH/SMD $\rho(z)$ are shown for $\alpha = 0, -1.4$ and $\beta = 1.0$. We rescale the $S_{\rm peak,obs}$ values by a factor of 0.1/1/10 for the constant/uniform/power-law $g(L)$ in order to avoid overlap with each other. The solid/dotted/dot-dashed lines for each $g(L)$ denote the NE/SFH/SMD $\rho(z)$ distribution.

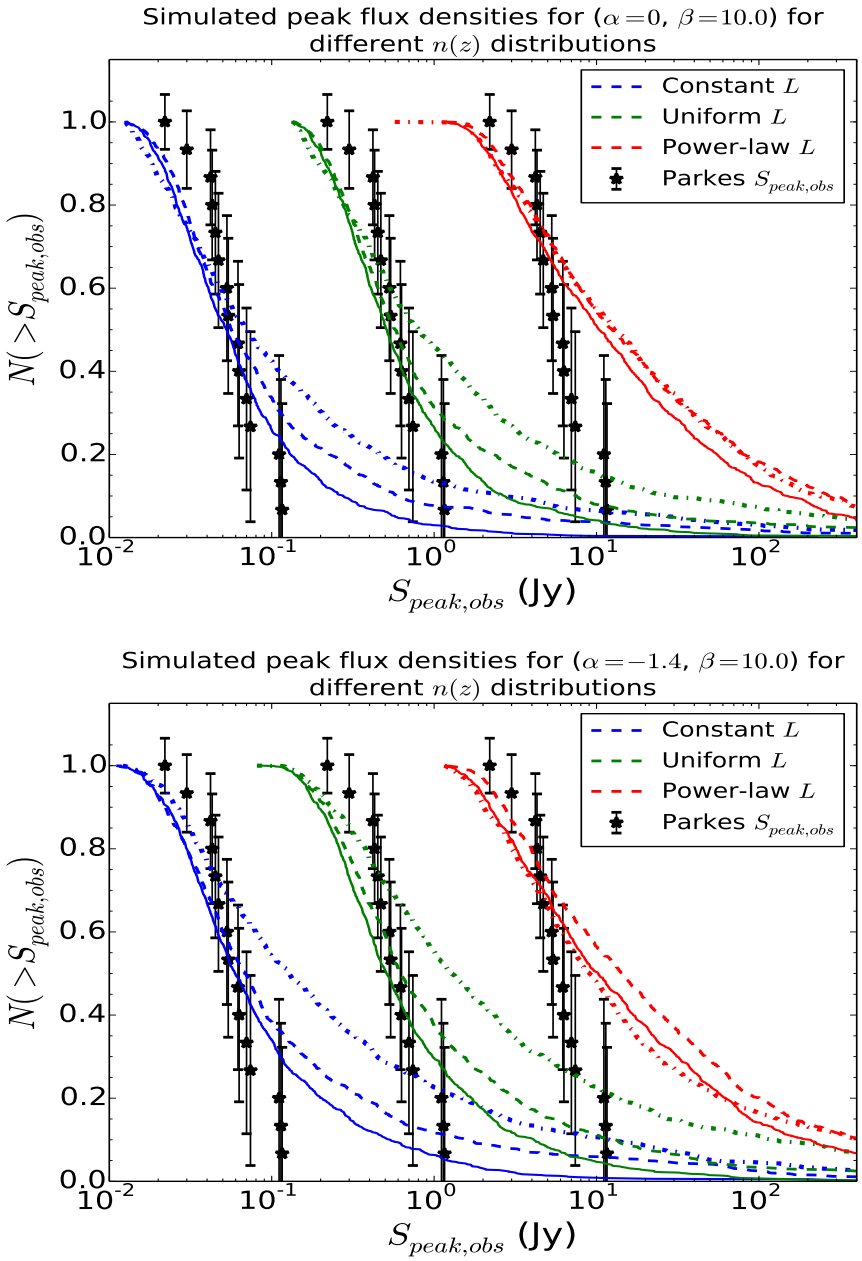

Figure 5.5: *Comparison of observed Parkes* $S_{\rm peak}$ *with simulated* $S_{\rm peak}$ *distributions for different* $g(L)$ *and* $\rho(z)$ *models,* $\alpha = 0, -1.4$ *and* $\beta = 10.0$*:* Simulated $N(> S_{\rm peak,obs})$ distributions for constant/uniform/power-law $g(L)$ and NE/SFH/SMD $\rho(z)$ are shown for $\alpha = 0, -1.4$ and $\beta = 10.0$. We rescale the $S_{\rm peak,obs}$ values by a factor of 0.1/1/10 for the constant/uniform/power-law $g(L)$ in order to avoid overlap with each other. The solid/dotted/dot-dashed lines for each $g(L)$ denote the NE/SFH/SMD $\rho(z)$ distribution.

assume for simplicity that all the detected bursts are located at the position of the Solar system. We estimate the host galaxy DM contribution as $DM_{\rm host} = \beta DM_{\rm NE2001}$, where β is the scaling factor related to the host galaxy size compared to the MW and $DM_{\rm NE2001}$ is predicted by the NE2001 model (Cordes & Lazio 2002). The assumption about the location of the FRB source will not affect our analysis here qualitatively as $DM_{\rm tot} \gg DM_{\rm host}$ for most of the reported bursts.

In Figures 6.3 and 5.5, we show the comparison of the observed $S_{\rm peak}$ at Parkes with that obtained from the simulations for different $g(L)$ and $\rho(z)$ models. We perform these simulations for constant, uniform and power-law $g(L)$ along with NE, SFH and SMD $\rho(z)$ distributions. We also vary the energy density spectral index $\alpha = 0, -1.4$ and the $DM_{\rm host}$ parameter $\beta = 1, 10$. The best-fit value of $\alpha \approx -1.5$ was recently obtained by Macquart et al. (2019) from the spectra of 23 FRBs detected with ASKAP (Bannister et al. 2017; Shannon et al. 2018).

We list the p-values obtained from the KS test comparison for all these cases in Table B.1. We perform all KS tests under the null hypothesis that the two samples were drawn from the same distribution unless the p-value < 0.05.

We find that FRBs most likely do not originate from older stars as $\rho(z) \propto \rho_{\rm SMD}$ is unfavored by the current Parkes observations for all $g(L)$ models and (α, β) combinations. Moreover, power-law $g(L) \propto L^{-1.298}$ over-estimates the occurrence of brighter events for all FRB spatial density distributions. The FRB source luminosity distribution is better modelled with a sharp cutoff around $L_{\rm mid} \approx 5 \times 10^{44}$ erg/s.

For all $g(L)$ distributions and (α, β) combinations, we find that the FRB progenitors are most likely to be younger stars with population density history

Table 5.2: KS test p-values obtained from the comparison of $N(> S_{\rm peak})$ distributions in Figure 6.2 (from equation 5.6) and Figures 6.3 and 5.5 (from MC simulations) with the observed FRB population. We consider constant, uniform and power-law luminosity distributions along with NE (SFH) [SMD] spatial density models.

Case	$g(L) = \delta(L - L_{\rm mid})$
Equation 5.6	
$(\alpha = 0, \beta = 1)$	0.084 (0.247) [0.019]
$(\alpha = -1.4, \beta = 1)$	0.040 (0.070) $[2.49 \times 10^{-4}]$
$(\alpha = 0, \beta = 10)$	0.127 (0.156) [0.015]
$(\alpha = -1.4, \beta = 10)$	0.034 (0.125) $[3.72 \times 10^{-4}]$
Case	$g(L) = 1/(L_{\rm mid} - L_{\rm min})$
Equation 5.6	0.055 (0.402) [0.024]
$(\alpha = 0, \beta = 1)$	0.111 (0.225) [0.009]
$(\alpha = -1.4, \beta = 1)$	0.025 (0.127) $[2.41 \times 10^{-4}]$
$(\alpha = 0, \beta = 10)$	0.159 (0.162) [0.008]
$(\alpha = -1.4, \beta = 10)$	0.047 (0.156) $[3.48 \times 10^{-4}]$
Case	$g(L) \propto L^{-1.298}$
Equation 5.6	0.227 (0.214) [0.306]
$(\alpha = 0, \beta = 1)$	3.05×10^{-4} (3.05×10^{-3}) $[2.03 \times 10^{-3}]$
$(\alpha = -1.4, \beta = 1)$	3.48×10^{-4} (2.49×10^{-3}) $[2.03 \times 10^{-3}]$
$(\alpha = 0, \beta = 10)$	4.69×10^{-4} (1.41×10^{-3}) $[3.05 \times 10^{-4}]$
$(\alpha = -1.4, \beta = 10)$	1.77×10^{-4} (1.64×10^{-3}) $[3.14 \times 10^{-3}]$

tracing the cosmic SFH as the likelihood of $\rho(z) \propto \rho_{\rm SFH}$ is found to be larger compared to $\rho(z) \propto \rho_{\rm NE}$. Lastly, while $\rho(z) \propto \rho_{\rm NE}$ with $\alpha = 0$ and $\beta \sim 1 - 10$ is a likely scenario, $\rho(z) \propto \rho_{\rm SFH}$ is the most favoured possibility from the current observations for $\alpha = 0$ and $\beta \sim 1$. Most events are therefore expected to arise from young stars with a relatively flat energy density distribution and a host galaxy DM contribution similar to that of the MW.

5.4 Summary and conclusions

In this Chapter, we have presented a method to constrain the source luminosity function and spatial density distribution of the FRB progenitors from the statistical properties of the observable flux density. As the sample of the reported FRBs is rapidly growing and largely heterogenous, we restrict our analysis to the Parkes FRBs that were published until February 2019 with $DM_{\rm tot} \geq 500$ pc cm^{-3} and have resolved intrinsic widths. We apply a lower $DM_{\rm tot}$ cutoff to minimize the errors in the distance estimates and subsequently the inferred luminosities that are based on the assumptions about the host galaxy properties and the source location inside it. Here we consider $\rho(z)$ corresponding to a non-evolving population $\rho_{\rm NE}$/young stellar population tracking $\rho_{\rm SFH}$/older stellar population tracking $\rho_{\rm SMD}$ along with constant/uniform/power-law $g(L)$ distributions.

Assuming scattering model for pulse temporal broadening from multipath propagation and a fixed $DM_{\rm host}$ contribution, we derived $N(> S_{\rm peak})$ for a FRB population with given spatial density and luminosity function. We found that the intrinsic $N(> S_{\rm peak})$ distribution for the FRBs observed with Parkes is likely due to a population density of young stars $\propto \rho_{\rm SFH}$ and luminosity function with

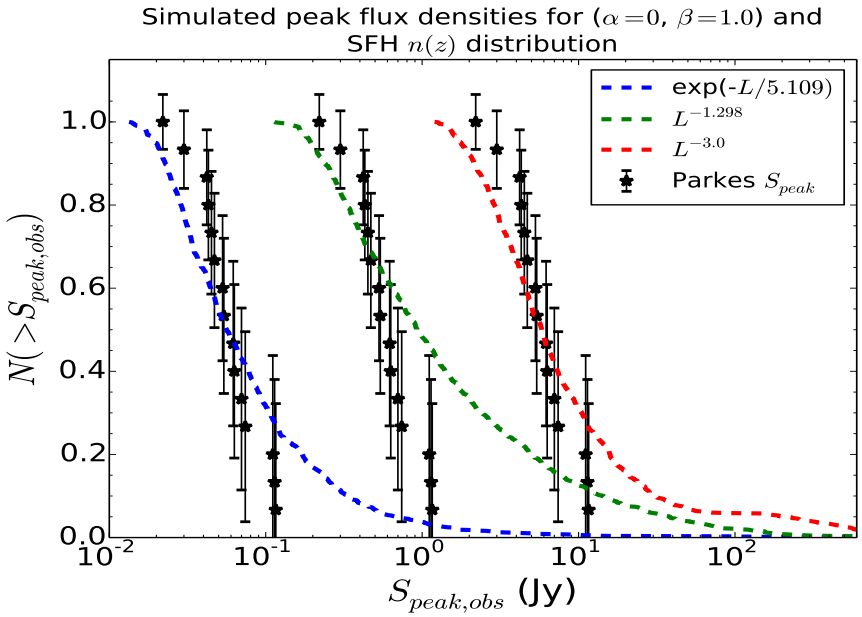

Figure 5.6: *Comparison of observed Parkes $S_{\rm peak}$ with simulated distributions for different $g(L)$ functions:* Simulated $N(>S_{\rm peak})$ distributions for exponential and power-law $g(L)$ with indices -1.298 and -3.0 are shown for $\alpha = 0$, $\beta = 1.0$ and SFH $n(z)$. We rescale the flux values for $\exp(-L/5.1\times10^{44}$ erg/s$)/L^{-1.298}/L^{-3.0}$ by a factor of 0.1/1/10 to avoid overlap. The corresponding p-values are 0.196, 3.05×10^{-3} and 0.213.

a sharp cutoff around $L_{\rm mid} \sim 5.1\times10^{44}$ erg/s. While the inferred power-law $g(L)\propto L^{-1.298}$ can explain the abundance of sources with large luminosities, the spatial density models are found to be practically indistinguishable from the current observations. In addition to the pulse broadening due to propagation effects, the observed flux distribution is also affected by the instrumental effects in the detection equipment such as the telescope beam shape and temporal resolution. While a coarse temporal resolution makes it less likely to detect a pulse with small $w_{\rm obs}$ due to the instrumental noise, there is also an observing bias against events with large $w_{\rm obs}$ due to reduced telescope sensitivity.

We performed MC simulations to understand the effects of telescope observing

biases, FRB energy density function and host galaxy properties on the observed flux distribution. We found that FRBs are unlikely to originate from relatively older stars with $\rho(z) \propto \rho_{\rm SMD}$ and should have a luminosity function that is steeper than the inferred $g(L) \propto L^{-1.298}$ based on the current detection rate of the brighter events with Parkes. Figure 5.6 shows the comparison of observed Parkes $S_{\rm peak}$ with that from simulations for $\alpha = 0$, $\beta = 1.0$ and SFH $\rho(z)$ model. The simulations are carried out for $g(L) \propto \exp(-L/5.1 \times 10^{44}$ erg/s), $g(L) \propto L^{-1.298}$ and $g(L) \propto L^{-3.0}$. We find that the source luminosity function is better modelled with a relatively steeper power-law $g(L)$ with index $\lesssim -3.0$ or an exponential $g(L)$ with luminosity cutoff $L_{\rm c} \sim L_{\rm mid}$.

Based on the current Parkes observations, we have found that the FRB progenitors are most likely to be younger stars with spatial density tracing the cosmic SFH, have a relatively flat source energy density spectrum with $\alpha \approx 0$ and a host galaxy DM contribution $\beta \approx 1$ that is similar to that from the MW. As the observed sample of FRBs further grows with detections made at finer temporal resolutions and with better source localisations across multiple surveys, stronger constraints can be applied using our analysis on the source luminosity function and the evolutionary history of the cosmic rate density from the observed flux distribution.

Chapter 6

Summary and future work

In this thesis, we first presented a method to study the true properties of the observed non-repeating and repeating FRBs, and used detailed Monte Carlo simulations to constrain the properties of the FRB sources, their host galaxies and the intervening turbulent IGM/ISM from the current radio observations. We further investigated whether the repeating FRB 121102 can be used as a representative event for the entire FRB population based on its energy distribution function and the current FRB follow-up observations. We also constrained the spatial density of these energetic FRB sources directly from their observed flux density distributions in order to understand the nature of their progenitors.

Although the physical origin of these events is still a matter of open debate with no concrete information about the progenitor model and/or radiation mechanism known at present, the population modelling of the FRB parameters helps in extracting useful information regarding the physical properties of these radio bursts from their observations. We have only considered FRBs with $DM_{\rm tot}$ exceeding 500 pc cm^{-3} that were published until February 2019 and derived their true properties self-consistently from the observations without assuming any initial distributions for the FRB parameters.

As the sample of reported FRBs will continue to expand rapidly with several broad-band radio surveys becoming operational, the methods presented in

this work can be applied in the near future to study the interplay between underlying source distribution, instrument properties and detection statistics. This will further place tighter constraints on the spectral behaviour, redshift and energy distribution for FRB sources as well as the properties of the host galaxy and burst local environment. In a future work, we plan to extend our analysis to a broader inhomogeneous FRB sample obtained from several wide-field surveys which will allow us to perform a parametric study using detailed maximum likelihood analysis.

6.1 Model assumptions and implications

We estimated the individual burst distances by assuming a fixed host galaxy DM contribution and intrinsic pulse widths from two different scattering models for the temporal broadening due to multipath propagation of the pulse through ionized plasma. While $w_{\rm ISM}$ is suppressed relative to $w_{\rm IGM}$ by the geometrical lever-arm factor $\sim 4f(1-f)$ for both scattering models, $w_{\rm IGM}$ for model 2 is based on a theoretical model for IGM turbulence as opposed to an observationally established empirical fit for model 1.

After computing $S_{\rm peak,int}$ from $w_{\rm int}$ and $\mathcal{F}_{\rm obs}$, we obtained the bolometric luminosity and energy for the bursts for a flat FRB energy spectrum with coherent emission within frequency range $\nu'_{\rm min} = 600$ MHz to $\nu'_{\rm max} = 8$ GHz. In our analysis, we have obtained the best fit cumulative distributions for $w_{\rm int}$ and $L_{\rm int}$ by including the biases due to the relatively uncertain $DM_{\rm host}$ contribution to $DM_{\rm Ex}$, assumptions about the $DM_{\rm IGM/ISM}$ dependence of $w_{\rm IGM/ISM}$ from the scattering models considered and the peak flux density reduction due to the finite beam size

of the telescope.

It should be noted that a larger host galaxy DM contribution would result in a smaller inferred z from equation (5.1) leading to a correspondingly small DM contribution from the IGM. The IGM scatter broadening $w_{\rm IGM}$ will then decrease while $w_{\rm ISM,host}$ from the host galaxy ISM increases. As $w_{\rm ISM,host}$ is suppressed significantly relative to $w_{\rm IGM}$ by the geometrical lever-arm factor, there is a net increase in $w_{\rm int}$ with increase in $DM_{\rm host}$. However, as $w_{\rm IGM}$ is almost two orders of magnitude smaller compared to $w_{\rm int}$ for both populations of FRBs (see Figures 2.1 and 2.2), the resultant increase/decrease in $w_{\rm int}/S_{\rm peak,int}$ is negligible and the reduction in the inferred L and E values from equation (5.4) can be ignored. Therefore, the $w_{\rm int}$ and $L_{\rm int}$ distributions derived for a typical MW-like host galaxy with $DM_{\rm host} \approx 100$ pc cm^{-3} in Section 5.1 will not change appreciably. Similarly, the assumption of a flat FRB energy spectrum with $\alpha \approx 0$ within the frequency range $\nu'_{\rm min} = 600$ MHz to $\nu'_{\rm max} = 8$ GHz does not affect the inferred luminosity values significantly relative to the $\alpha \approx -1.4$ case for the Kolmogorov turbulence spectrum.

In this study, we have used lognormal $w_{\rm int}$ (W1/2: mean $\mu_{1/2} = 0$ and standard deviation $\sigma_{1/2} = 0.25/0.50$) and power-law $L_{\rm int}$ (L1/2: PL index $\alpha_{L,1/2} = -1/-2$) as model input distributions to our MC code in order to constrain the physical properties of the observed FRBs. The distances to the simulated bursts are initially determined from the FRB spatial density (NE/SFH/PL) and the IGM contributions to the DM and width of the pulse are computed using z. The host galaxy DM contribution is obtained by assuming it to be a MW-like galaxy with the FRB source location similar to the Solar system and scaling $DM_{\rm NE2001}$ with

the parameter $\beta \sim 0.1 - 10$.

The telescope beam center flux density is then obtained for a PL FRB energy density $E_{\nu'} = k\nu'^{\alpha}$, observing frequency bandwidth $(\nu_1, \nu_2) = (\nu_0 - 0.5\nu_{\rm bw}, \nu_0 + 0.5\nu_{\rm bw})$ and FRB coherent emission frequency range $(\nu'_{\rm min}, \nu'_{\rm max}) = (600\,{\rm MHz}, 8\,{\rm GHz})$ from equation (3.3). We modelled the flux degradation due to finite telescope beam size using a Gaussian beam profile to obtain the $S_{\rm peak,obs}$ from equation (3.4). The $S_{\rm peak,obs}$ dependent S/N is computed for every simulated burst and the FRB is detected if its flux density exceeds the telescope sensitivity threshold. We only consider simulated FRBs with $DM_{\rm tot} \geq 500$ pc cm^{-3} for comparison with the observed sample to minimize the error in the estimates of the inferred parameters that are obtained by assuming a specific FRB source location and host galaxy structure.

6.2 Summary of main results

We compared the properties of the simulated non-repeating/repeating FRBs with those observed at Parkes/Arecibo in order to constrain the host galaxy DM relative to MW β, PL energy density spectral index α, scattering in the intervening turbulent plasma and the spatial density $n(z)$ of the FRB sources. We also discussed whether repeating FRB 121102 is representative of the entire FRB population based on its repetition rate $\dot{N}_0$ and a universal EDF. Lastly, we investigated the FRB spatial density and progenitor models using the observed flux density distribution.

In the following, we briefly summarise the main results of our analysis that is presented in this thesis:

1. **FRB intrinsic width and luminosity distributions:** The $w_{\rm int}$ for non-repeating (repeating) FRBs varies within a broad range $\sim 0.3 - 10$ ms ($\sim 0.1 - 8$ ms) and the cumulative width distribution is an exponential function with a cutoff $w_{\rm int,c} \sim 2.0$ ms (~ 1.6 ms), while $L_{\rm int}$ varies within $\sim 10^{43} - 10^{47}$ erg/s ($\sim 10^{41} - 10^{43}$ erg/s) with an exponential cumulative distribution and cutoff $L_{\rm int,c} \sim 8.0 \times 10^{44}$ erg/s ($\sim 2.7 \times 10^{42}$ erg/s).

   The ISM contribution to the width broadening is significantly suppressed in comparison to $w_{\rm IGM}$ due to the geometry of the scattering medium along the line of sight to the FRB source with $w_{\rm ISM,MW} \lesssim 10^{-3}$ ms and $w_{\rm ISM,host} \lesssim 10^{-6}$ ms for non-repeating FRBs and $w_{\rm ISM,host/MW} \lesssim 10^{-4}$ ms for repeating FRBs. As a result, the pulse width broadening due to scattering $w_{\rm sc} \approx w_{\rm IGM}$ for both classes of bursts. The scatter broadening of the pulse is found to be the smallest contribution to the $w_{\rm obs}$ with $w_{\rm sc} \lesssim 1$ ms ($w_{\rm sc} \lesssim 2 \times 10^{-2}$ ms) for the non-repeating (repeating) bursts.

   We find that $w_{\rm int}$ is largely scattering model independent for both classes of FRBs, and the average relative temporal broadening $\Delta w_{\rm int}/w_{\rm int} \sim 150\%$ and $\sim 20\%$ for non-repeating and repeating bursts, respectively. While $w_{\rm DM}$ is the dominant contribution to the temporal broadening for non-repeating FRBs with $w_{\rm obs} \sim w_{\rm int} \sim w_{\rm DM} \gg w_{\rm sc}$, the dispersive smearing in case of repeating bursts is significantly smaller with $w_{\rm obs} \approx w_{\rm int} \gg w_{\rm DM} \gg w_{\rm sc}$. Due to the small $z \approx 0.19273$ for FRB 121102, $w_{\rm sc}$ and $w_{\rm DM}$ contributions are found to be almost negligible and a considerable fraction of $w_{\rm obs}$ is expected to come from $w_{\rm int}$.

2. **Population synthesis simulation results and constraints:** For the log-normal $w_{\rm int}$ and the power-law $L_{\rm int}$ distributions that we considered in this work, we find that the simulated observable FRB properties exhibit a relatively weak dependence on the intrinsic model distributions, particularly for the parametric space that we study here. Furthermore, we find that a larger observed sample of Parkes FRBs at $\nu_{\rm obs} = 1.4$ GHz is required in order to clearly distinguish between the FRB spatial density models (NE and SFH) as well as the pulse scatter broadening models due to multipath propagation (model 1 and model 2). The DM contribution from the host galaxy of the FRB source is expected to be roughly comparable to the Galactic contribution with $\beta \sim 0.1 - 1$. The Parkes observations for the non-repeating FRBs favour a large negative value of the FRB energy density spectral index α within the range -3.0 to -1.5.

   We also compared the simulated FRB parameters with the Parkes data to constrain the peak redshift and low/high-z indices of the power-law FRB spatial density model. The spatial density of FRBs is likely to be a PL distribution peaking at slightly larger redshifts $z_{\rm crit} \sim 2.0$ compared to the cosmic SFH. The FRB density is expected to increase up to $z \approx z_{\rm crit}$ with a PL index $\alpha_l \sim 0 - 3$ and then drop considerably at larger distances with $\alpha_u \approx -3$.

3. **FRB 121102 repetition and representability:** We used the published FRB follow-up observing data in order to investigate whether FRB 121102 is representative of the entire population. The CED for the repeating FRB was computed by only including the FRB 121102 bursts for which $S_{\rm peak,obs}$

exceeds the Parkes $S_{\rm th}$. We obtained an exponential CED $\dot{N}_0 \exp(-E_{\rm obs}/E_0)$, with repetition rate $\dot{N}_0 \sim 0.090 - 0.283$ hr^{-1} and cutoff energy $E_0 \sim (4 - 6) \times 10^{39}$ erg for Parkes $S_{\rm th} \sim 0.1 - 0.4$ Jy.

We find that if all FRBs were to repeat at the same rate $\dot{N}_0 \sim 0.090 - 0.283$ hr^{-1} and with a universal EDF, the probability of observing none of them to be repeating will be $\sim 0.8{-}0.9$ for $\mathcal{F}_{\rm th} \approx 2$ Jy $-$ ms and Parkes $S_{\rm th} \sim 0.1{-}0.4$ Jy. As the universal EDF is found to be an exponential distribution with a cutoff energy that is much smaller compared to the typical non-repeating FRB energies, significantly longer FRB follow-up observations are needed to distinguish between the FRB populations.

The complex time-frequency sub-structures that has been found in repeating FRB pulses can provide strong constraints on the source emission mechanism, emission zone and physical parameters. With the rapid observational progress made using the high-resolution CHIME telescope currently, it will be much clearer in the near future whether the repeaters actually originate from a separate class of progenitors as compared to the non-repeating FRBs.

4. **Spatial distribution of FRB sources and progenitor models:** We have constrained the source luminosity function and spatial density distribution of FRB progenitors using the statistical properties of the observed flux density. We considered FRBs to be distributed in space according to: (a) non-evolving population, (b) population similar to younger stars, and (c) population similar to older stars. We found that the intrinsic flux density distribution of Parkes FRBs is explained by a population density that

is similar to that of younger stellar population with a luminosity function that has a sharp exponential cutoff around $\sim 5 \times 10^{44}$ erg/s.

FRBs are found to be highly unlikely to be originating from relatively older stellar population and need to have a steep power-law decay with index $\lesssim -3.0$ for the luminosity distribution, based on the detection rates of brighter events with Parkes. The FRB progenitors are most likely to be younger stars with spatial density that traces the cosmic SFH, have a relatively flat source energy density spectrum and a host galaxy DM contribution that is similar to that from the MW. With the rapidly evolving observed sample of FRBs at finer temporal resolutions and better source localisations, stronger constraints will be applied on FRB progenitors using our analysis in the near future.

6.3 Future work

Here we discuss the scope of future work and the astrophysical implications of the rapid growth in the observed FRB population. The properties of the FRB sources will be explored across a broad range of radio frequencies and dedicated surveys will continue to search for multi-wavelength electromagnetic counterparts in the near future. With further characterisation of the underlying source distributions, we will be able to optimise future searches/follow-ups, identify distinctions/similarities within the observational sub-classes and also gain valuable insights about the FRB progenitors, source environments and host galaxy properties. Below we discuss some exciting directions in the field of FRBs and their wide-ranging applications.

6.3.1 Unified emission mechanism for FRBs

The high FRB brightness temperatures $T_b > 10^{33}$ K coupled with the short $\lesssim$ milliseconds intrinsic burst durations requires coherent emission from a compact region. Considering the shortest duration burst structures with $t \sim 30$ μs detected until date (Michilli et al., 2018; Farah et al., 2018), implies an emission zone with size $\lesssim 10$ km. Understanding the origin of these radio bursts and the associated multi-wavelength emission will give us a better idea of the underlying emission mechanism for these sources.

Two classes of coherent emission mechanisms have been considered in the literature thus far: the maser and the antenna mechanism. Using the observed properties of repeating FRB 121102, Kumar et al. (2017) and Lu & Kumar (2018) have already shown that the maser mechanism cannot satisfactorily explain the high observed luminosities of FRBs unless fine-tuned plasma conditions are invoked. They have shown that antenna curvature emission by the coherent charged bunches is the most favoured mechanism whereby the bursts are powered by the magnetic reconnection events that occur close to the surface of a magnetar with magnetic field $B \gtrsim 10^{14}$ G.

Table 6.1 lists the properties of the recently localised non-repeating FRBs 190523, 180924, 181112 (Bannister et al., 2019; Prochaska et al., 2019b; Ravi et al. 2019b) along with the repeating FRBs 121102 and 180916 (Tendulkar et al., 2017; Marcote et al., 2020). While the repeating FRBs have been localised in spiral/dwarf galaxies with low mass, low metallicity and high star formation rates, the non-repeating sources were found in elliptical galaxies with high mass, high metallicity and low star formation rates. This naturally raises the question

Table 6.1: FRB source and host galaxy properties obtained from the recent localisations of non-repeating FRBs 190523, 180924, 181112 and repeating FRBs 121102, 180916. Here SFR denotes the galactic star formation rate, L_{bol} is the estimate for bolometric luminosity and the offset is from the center of the host galaxy. The data for FRBs 121102, 180916, 190523, 180924 and 181112 are obtained from Tendulkar et al. (2017), Marcote et al. (2020), Ravi et al. (2019b), Bannister et al. (2019) and Prochaska et al. (2019b), respectively.

FRB (Telescope)	Host galaxy	z (D_L/Gpc)	Offset (kpc)	Stellar mass ($M_\odot$)	SFR ($M_\odot$/yr)	L_{bol} (erg/s)
121102 (Arecibo)	Low metallicity irregular dwarf	0.19 (0.90)	0.5-1	$(4-7)\times10^7$	0.4	4×10^{38}
180916 (CHIME)	Massive face-on spiral	0.034 (0.149)	4.7	10^{10}	>0.016	10^{36}
190523 (DSA-10)	Massive galaxy	0.66 (4.08)	29	10^{11}	<1.3	10^{41}
180924 (ASKAP)	Massive lenticular or early-type	0.32 (1.5)	4	2.2×10^{10}	<2	10^{40}
181112 (CHIME)	Faint galaxy	0.475 (2.3)		2.6×10^9	0.6	10^{39}

whether these two classes of bursts originate from fundamentally different types of source environments and host galaxies or they are just bursts arising at different stages of the progenitor evolution. Although the host galaxies of the repeating FRBs 121102 and 180916 are fundamentally different, in both cases the source is located near or within an actively star-forming region of their host galaxy.

Due to their specific locations close to the actively star-forming regions within the host galaxies, young neutron stars born in core-collapse supernovae (CCSNe) have been proposed to be the possible progenitors for repeating FRBs. Furthermore, the association with star-forming region within dwarf galaxy is similar to that found in the host galaxies of super-luminous supernovae (SLSNe) and long-duration GRBs. The large offsets from the host galactic centers along with the low star-formation rates for the localised non-repeaters indicates neutron star progenitors formed by compact mergers (binary neutron stars or black hole-neutron star) with properties similar to that of short-duration GRBs.

Apart from the association of repeating/non-repeating FRB progenitors to neutron stars formed by core-collapse supernovae/compact binary mergers, an alternate scenario is connecting the activity of the source directly to its stellar evolution stage. Bhattacharya (2019) and Kumar et al. (2017) have already shown that FRBs are likely to be episodic outbursts of coherent radiation generated by the forced reconnection of strong magnetic fields near the surfaces of young neutron stars with steep luminosity distributions. With the recent localisations, connecting both FRB sub-classes with a unified radiation mechanism is a worthwhile investigation.

In a likely scenario, the slower variability of the surface magnetic field topology

for an older neutron star can gradually reduce the likelihood for the reconnection events to occur and thereby generate episodic bursts of coherent radiation. This can lead to a gradual transition in the observable FRB properties from repeater-like to non-repeater-like with less frequent and more energetic bursts produced over time. The dependence from the neutron star age can be folded into the star formation rate history as well as the evolution of the magnetar field structure in order to characterise the progenitor properties and guide future observations.

6.3.2 Constraints on source intrinsic variability timescales

The observed pulse width of each FRB is a combination of an intrinsic component and broadening contributions due to propagation and instrumental effects. FRB pulses show various propagation effects such as dispersive delay, scattering, scintillation and Faraday rotation, each of which carry important information about the source local environment and the galactic hosts of FRBs. One should be careful while interpreting the FRB spectral features in order to differentiate the propagation effects from the intrinsic component that is primarily dependent on the FRB source itself.

Propagation effects such as scattering and dispersive delay have strong frequency dependencies and are significantly more prominent at lower radio frequencies. Mapping the evolution of propagation effects across a wide radio frequency range can help to disentangle the intrinsic signal properties from the extrinsic propagation effects. As scattering is the dominant effect at low radio frequencies $\sim$400-800 MHz, the recent observations from CHIME at such frequencies can be utilised in order to study the pulse temporal broadening models due to turbulence in the IGM and ISM for both MW and host galaxy. The rise and fall-off regions

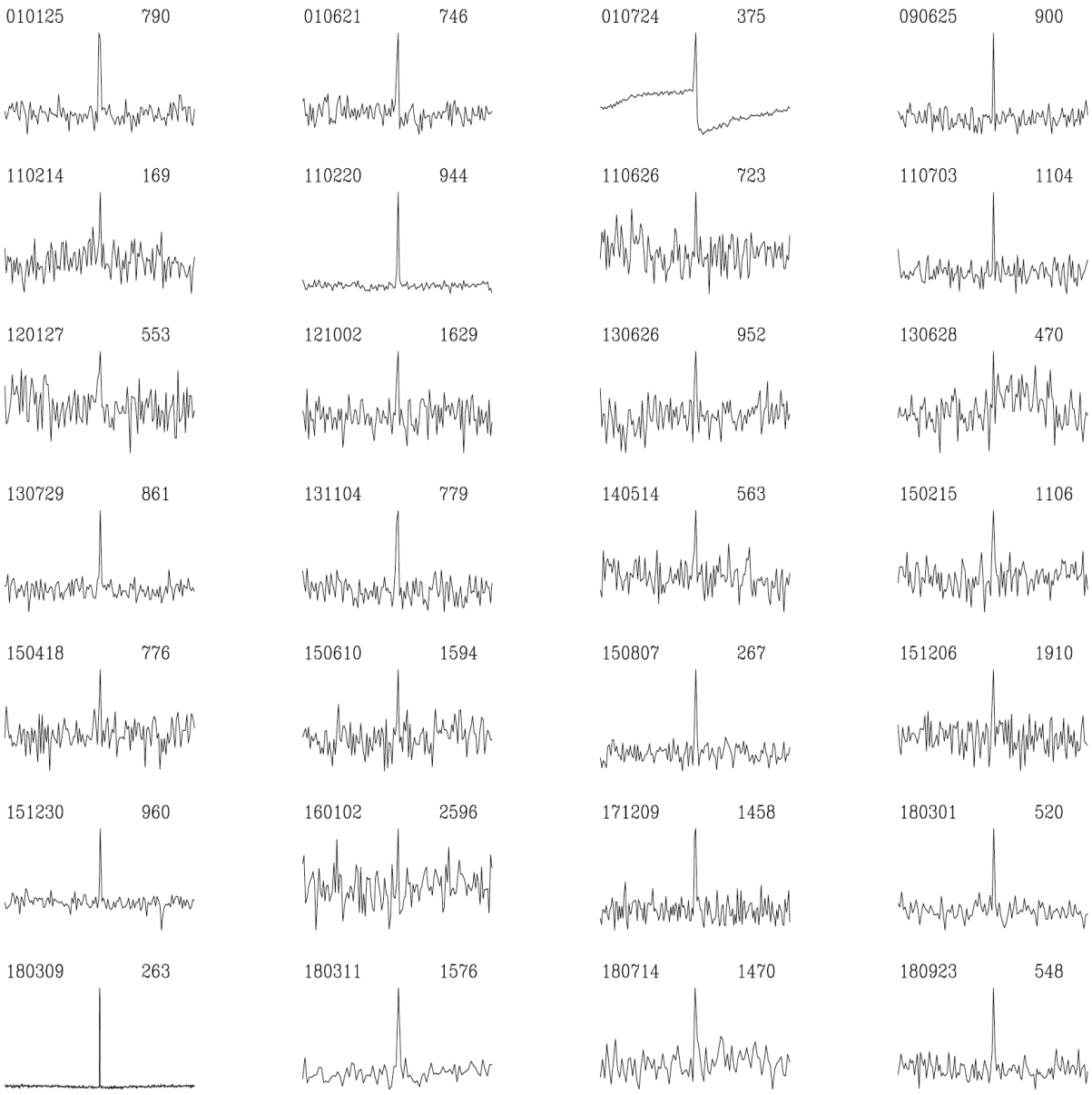

Figure 6.1: The first twenty-eight FRBs discovered with the Parkes telescope, arranged in the order of date. Each light curve shows a 2 second window around the pulse. Listed to the left of each pulse are the FRB identifier and to the right are the observed dispersion measures in units of pc cm^{-3}. Obtained from Petroff et al. (2019).

of the observed FRB light curves can also constrain the scattering contribution to the pulse temporal broadening.

Some FRBs with narrow pulse durations detected with Parkes are still unresolved in width after pulse de-dispersion due to the insufficient time and frequency resolutions and only upper limits can be placed on their intrinsic widths (Ravi 2019). In order to constrain the intrinsic pulse duration and thereby source variability timescales, characterising the sub-millisecond fluctuations in the light curves from high-frequency observations (e.g. VLA 4-8 GHz) can be useful. Searches for finer timescale structures in repeating and non-repeating bursts should be done at high observing frequencies to avoid pulse smearing due to scattering.

As the FRB spectral behaviour will still include intrinsic fluctuations or variabilities as well as effects from post-emission propagation processes, the power spectral density (PSD) of the observed light curves will be useful. For sufficient time and frequency resolutions that is possible with continuous voltage capture systems such as Breakthrough Listen (Gajjar et al., 2018), we can directly probe the sub-millisecond fluctuations related to the source intrinsic variability. These sub-millisecond fluctuations from the source can then be utilised to place constraints on the progenitor models as well as the coherent emission mechanism for FRB sources.

6.3.3 FRBs as independent cosmological probes

Fast radio bursts detectable across cosmological distances are powerful probes to study baryonic density distribution, IGM turbulence and magnetic fields, dark energy equation of state and the reionisation history of the Universe. As FRB

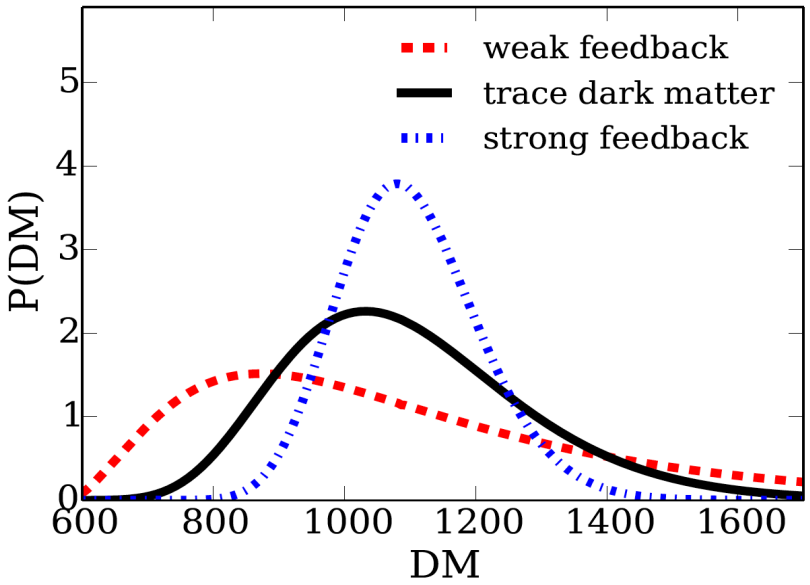

Figure 6.2: DM distributions for FRB sources at $z \approx 1$ depends on how the baryons are distributed around galaxy cluster halos along the line of sight. A more concentrated probability density around the central value indicates more diffuse gas and stronger feedback. Obtained from McQuinn (2014).

scattering widths are directly correlated with the DM contribution from IGM, we can perform detailed studies of the IGM free electron density and turbulence properties, probe the host galaxy DM distribution and establish an empirical relation based on localised FRBs to obtain cosmic proper distance measures.

While we can link FRB DMs to their redshifts assuming a given set of cosmological parameters, we can similarly put direct constraints on the cosmological model parameters once we independently localise FRBs and obtain the redshifts of FRB host galaxies. One immediate application of this is the identification of ionised part of missing baryonic matter in the local Universe. The matter in stars, gas and dust between galaxies is not sufficient in order to account for all the baryon content in the Universe. Approximately 30% baryons reside in the warm

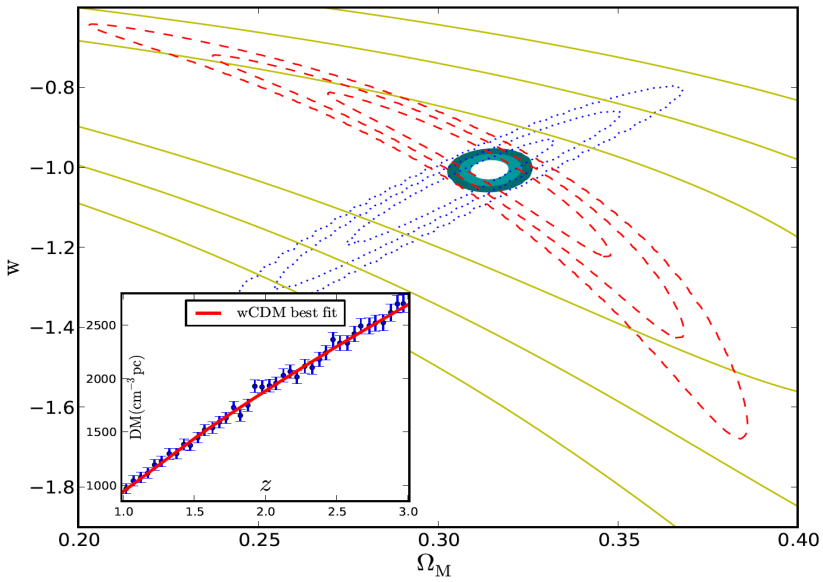

Figure 6.3: Contour lines for constraining w and Ω_M. The solid yellow lines, dashed red lines and dotted blue lines are for SNe Ia, FRBs and BAO data, respectively. The inset shows the $DM - z$ distribution for 1000 simulated FRBs. Obtained from Zhou et al. (2014).

intergalactic phase and 15% in hot gas in the low-redshift Universe, with 5% in the circumgalactic gas in galactic halos, 7% in galaxies and 4% in galaxy clusters. This still leaves a significant fraction ∼30% of baryons that cannot be accounted for and are therefore referred to as the missing baryons.

In order to validate the standard cosmological model, finding these missing baryons is essential. As most of these missing baryons are believed to be residing in the warm-hot IGM with high temperatures and low densities, they are not easily detectable as they do not exhibit any significant absorption or emission. Localising FRBs and measuring their redshifts independently will help us to identify every ionised baryon along the line of sight and could thereby provide direct detection of the missing baryons.

McQuinn (2014) calculated the distributions of FRB DMs with sources at $z \approx 1$ and showed that the DM dispersion strongly depends on the feedback strength. The dispersion in FRB DMs for sources located at the same redshift is shown in Figure 2. We get different FRB DM distributions for sources at same distance dependent on how far the baryons are extending from the halos of the galaxies along sightlines and location of baryons within the halo. Zhou et al. (2014) showed that if sufficient FRBs are detected within a narrow redshift interval, FRBs can be used to constrain the dimensionless parameter w that characterises the equation of state of dark energy. The contour lines constraining the cosmological parameters are shown in Figure 3 where the data for SNe Ia, BAO and FRBs are included.

The primary cosmological applications of a population of localised FRBs in the near future are:

(a) *Detecting missing baryons at low-z:* With sufficiently large number of localised FRBs, we can test whether the baryons are localised within the galactic halo virial radius or out in the intra-halo medium. The DM variation for FRBs placed at similar redshifts and the resultant shape of the distribution depends on the extent of the baryonic distribution around the halos.

(b) *High-redshift cosmic rulers:* From the dependence of DM_{IGM} on the cosmological parameters and therefore the geometry of the Universe, FRBs located at large redshifts will be crucial in order to place constraints on the dark energy EoS parameter $w(z)$ beyond what is currently given by the Type Ia SNe and BAO observations.

(c) *Primordial IGM magnetic fields and turbulence:* The IGM and host galaxy scattering can be distinguished based on the redshift dependence of the scattering

magnitude. Combining the DM information together with scattering, we can reconstruct the structure and turbulent properties of the baryons in the IGM. If FRB emission consists of significantly linearised component, the observed FRB RMs can also be also used to probe the mean IGM magnetic fields.

(d) *Probing He reionisation epoch:* It is expected that H/He are fully ionised for redshifts $z \lesssim 6/z \lesssim 3$, however the exact reionisation epochs are still unknown. With sufficient number of localised FRBs up to large redshifts $z \gtrsim 3$, studying the DM_{IGM} variation will allow us to probe the era of He reionisation directly from the observed variation in the steepness of the $DM_{IGM} - z$ curve.

Appendices

Appendix A

Pulse temporal broadening due to IGM turbulence

Here we derive the expression (equation 5.3) for the pulse temporal smearing due to IGM turbulence for the theoretical model proposed by Macquart & Koay (2013) [henceforth MK13]. Substituting the scattering broadened angular image size $\theta_{\rm sc} = f D_{LS}/D_S k\, r_{\rm diff}$ from equation (13) of MK13, the IGM temporal smearing $w_{\rm IGM}$ from equation (15) of MK13 can be written as

$$w_{\rm IGM} = \frac{D_L D_S \theta_{\rm sc}^2}{c D_{LS}(1+z_L)} = \frac{f^2 \lambda_0^2}{c(1+z_L)} \frac{D_{\rm eff}}{4\pi^2 r_{\rm diff}^2} \tag{A.1}$$

where $D_L/D_S/D_{LS}$ is the angular diameter distance from the observer to the scattering region/observer to the source/scattering region to the source, $z_L/z_S/z_{LS}$ is the corresponding redshift, $D_{\rm eff} = D_L D_{LS}/D_S$ and $\lambda = 2\pi/k$ is the wavelength in the observer frame.

We consider the case when the diffractive length scale $r_{\rm diff}$ is smaller compared to the inner scale of the scattering region l with the constant $f_K = 1.18$ to obtain $r_{\rm diff} = (8.0 \times 10^9 \text{ m})\ \lambda_0^{-1}\ {\rm SM}_{\rm eff,0}^{-1/2}\ l_0^{1/6}$ from equation (10a) of MK13, where $\lambda_0 = \lambda/(1 \text{ m})$, ${\rm SM}_{\rm eff,0} = {\rm SM}_{\rm eff}/(10^{12} \text{ m}^{-17/3})$ and $l_0 = l/(1 \text{ AU})$. The constant f_K is directly associated with the power-law index β_K for Kolmogorov turbulence spectrum with $f_K = 1.18$ corresponding to $\beta_K = 4$ and $r_{\rm diff} < l$.

Substituting equation (20) of MK13 for the density fluctuation amplitude from turbulence into equation (23) of MK13, the z-corrected effective scattering measure can be written as

$$\mathrm{SM}_{\mathrm{eff}}(z) = K_1 \int_0^z (1+z')^3 d_H(z') dz' \tag{A.2}$$

where $d_H(z') = (c/H_0)[\Omega_m(1+z')^3 + \Omega_\Lambda]^{-1/2}$ and $K_1 \approx (9.42 \times 10^{-14}\ \mathrm{m}^{-20/3})$ is constant for the scattering region outer scale $L \sim 1$ pc and Kolmogorov turbulence spectrum.

Further substituting r_{diff} in terms of $\mathrm{SM}_{\mathrm{eff}}$ into equation (A.1) and rewriting $\lambda_0 = c/\nu_0$ gives the temporal smearing timescale (in sec)

$$w_{\mathrm{IGM}}(z) = K_2 \frac{D_{\mathrm{eff}}}{(1+z_L)} \frac{\mathrm{SM}_{\mathrm{eff}}(z)}{\nu_0^4} \tag{A.3}$$

where $K_2 \approx (1.56 \times 10^{-32}\ \mathrm{s})(f_K^2 c^3/4\pi^2)(l_0/1\ \mathrm{AU})^{-1/3}$ is constant and ν_0 is the wave frequency in Hz in the observer frame.

Next in order to simplify $w_{\mathrm{IGM}}(z)$ from equation (A.3) in terms of just the FRB source redshift z, we need to obtain D_{eff} directly from cosmology. It is expected that the pulse temporal smearing will be maximized when the scattering screen is placed symmetrically midway along the source to the observer line of sight (Vandenberg 1976; Lorimer et al., 2013).

Therefore, in order to further simplify the calculations and obtain the maximum expected value of w_{IGM} for a given FRB line of sight, we use $z_L \approx (1/2)z$ with the condition on comoving distances

$$D_L(1+z_L) = D_{LS}(1+z_{LS}) = 0.5 D_S(1+z).$$

Lastly, substituting $D_{\rm eff} = D_L D_{LS}/D_S$ and $SM_{\rm eff}(z)$ from equation (A.2) in equation (A.3) gives

$$w_{\rm IGM}(z) = \frac{k_{\rm IGM}}{\nu_{0,\rm GHz}^4 Z_L} \int_0^z \frac{dz'}{\left[\Omega_m(1+z')^3 + \Omega_\Lambda\right]^{0.5}} \times \int_0^z \frac{(1+z')^3}{\left[\Omega_m(1+z')^3 + \Omega_\Lambda\right]^{0.5}} dz' \tag{A.4}$$

where $k_{\rm IGM}$ is the redshift independent normalisation factor including K_1 and K_2, $\nu_{0,\rm GHz} = \nu_0/10^9$ and $Z_L = 1 + (1/2)z$.

Appendix B

FRB intrinsic parameter distributions

Here we list the best fit distribution parameters for both non-repeating and repeating FRBs.

Table B.1 lists the functional fit parameters with the corresponding chi-squared values for the pulse width and luminosity of the non-repeating FRBs. The repeating FRB width and luminosity distribution fit parameters with the chi-squared values are listed in Table B.2.

For both non-repeating and repeating FRBs, we consider three different distributions: power-law, exponential and gaussian, in order to model the width and luminosity parameters. We also investigate the intrinsic width and luminosity using two scattering models corresponding to "Intrinsic 1" and "Intrinsic 2" (see Chapter 2 for more details on the specific scattering model parameters).

We find that for non-repeating FRBs, the exponential distribution is the best fit for both width and luminosity parameters. The power-law model overestimates the width and luminosity in case of repeating FRB 121102 and exponential distribution is the best bit for both parameters.

Table B.1: Power-law, exponential and gaussian fit parameters for the width and luminosity distributions of non-repeating FRBs

Width	Distribution	Functional fit	Reduced χ^2
Observed	Power-law	$(34.408 \pm 2.147)\ w_{\rm obs}^{-0.913\pm0.052}$	0.295
	Exponential	$(29.928 \pm 1.290)\ e^{-w_{\rm obs}/(4.258\pm0.216)}$	0.113
	Gaussian	$(20.227 \pm 1.232)\ e^{-w_{\rm obs}^2/2(4.143\pm0.268)^2}$	0.434
Intrinsic 1	Power-law	$(13.681 \pm 0.500)\ w_{\rm int1}^{-0.757\pm0.046}$	0.326
Intrinsic 2		$(12.994 \pm 0.500)\ w_{\rm int2}^{-0.716\pm0.045}$	0.356
	Exponential	$(26.048 \pm 1.132)\ e^{-w_{\rm int1}/(2.028\pm0.123)}$	0.145
		$(25.209 \pm 0.988)\ e^{-w_{\rm int2}/(2.081\pm0.118)}$	0.130
	Gaussian	$(19.011 \pm 1.140)\ e^{-w_{\rm int1}^2/2(1.827\pm0.130)^2}$	0.495
		$(18.832 \pm 1.105)\ e^{-w_{\rm int2}^2/2(1.832\pm0.130)^2}$	0.490

Luminosity	Distribution	Functional fit	Reduced χ^2
Observed	Power-law	$(12.736 \pm 0.807)\ L_{\rm obs}^{-0.314\pm0.030}$	0.933
	Exponential	$(16.732 \pm 1.082)\ e^{-L_{\rm obs}/(11.068\pm1.788)}$	0.687
	Gaussian	$(19.067 \pm 1.853)\ e^{-L_{\rm obs}^2/2(2.395\pm0.383)^2}$	1.311
Intrinsic 1	Power-law	$(17.686 \pm 0.583)\ L_{\rm int1}^{-0.205\pm0.024}$	0.199
Intrinsic 2		$(17.804 \pm 0.627)\ L_{\rm int2}^{-0.201\pm0.025}$	0.221
	Exponential	$(22.588 \pm 0.580)\ e^{-L_{\rm int1}/(7.700\pm0.528)}$	0.053
		$(22.938 \pm 0.602)\ e^{-L_{\rm int2}/(7.711\pm0.523)}$	0.052
	Gaussian	$(19.287 \pm 0.806)\ e^{-L_{\rm int1}^2/2(5.272\pm0.464)^2}$	0.222
		$(19.539 \pm 0.826)\ e^{-L_{\rm int2}^2/2(5.243\pm0.453)^2}$	0.215

Table B.2: Power-law, exponential and gaussian fit parameters for the width and luminosity distributions of repeating FRB 121102

Width	Distribution	Functional fit	Reduced χ^2
Observed	Power-law	$(40.114 \pm 1.632)\ w_{\rm obs}^{-0.657\pm0.033}$	5.255
	Exponential	$(93.887 \pm 0.757)\ e^{-w_{\rm obs}/(2.135\pm0.023)}$	0.113
	Gaussian	$(71.173 \pm 1.438)\ e^{-w_{\rm obs}^2/2(1.992\pm0.043)^2}$	0.973
Intrinsic 1	Power-law	$(35.788 \pm 1.389)\ w_{\rm int1}^{-0.629\pm0.030}$	4.355
Intrinsic 2		$(36.731 \pm 1.413)\ w_{\rm int2}^{-0.633\pm0.031}$	4.359
	Exponential	$(94.470 \pm 0.836)\ e^{-w_{\rm int1}/(1.626\pm0.019)}$	0.126
		$(93.264 \pm 0.743)\ e^{-w_{\rm int2}/(1.773\pm0.019)}$	0.108
	Gaussian	$(71.814 \pm 1.489)\ e^{-w_{\rm int1}^2/2(1.483\pm0.033)^2}$	1.012
		$(70.624 \pm 1.464)\ e^{-w_{\rm int2}^2/2(1.651\pm0.037)^2}$	1.026

Luminosity	Distribution	Functional fit	Reduced χ^2
Observed	Power-law	$(2.436 \pm 0.351)\ L_{\rm obs}^{-0.593\pm0.028}$	4.228
	Exponential	$(89.749 \pm 1.013)\ e^{-L_{\rm obs}/(0.020\pm0.001)}$	0.215
	Gaussian	$(70.157 \pm 1.817)\ e^{-L_{\rm obs}^2/2(0.017\pm0.001)^2}$	1.579
Intrinsic 1	Power-law	$(3.363 \pm 0.440)\ L_{\rm int1}^{-0.547\pm0.026}$	4.443
Intrinsic 2		$(3.534 \pm 0.479)\ L_{\rm int2}^{-0.527\pm0.026}$	5.138
	Exponential	$(86.171 \pm 0.987)\ e^{-L_{\rm int1}/(0.027\pm0.001)}$	0.232
		$(86.552 \pm 1.017)\ e^{-L_{\rm int2}/(0.025\pm0.001)}$	0.246
	Gaussian	$(68.485 \pm 1.939)\ e^{-L_{\rm int1}^2/2(0.022\pm0.001)^2}$	1.905
		$(68.203 \pm 1.967)\ e^{-L_{\rm int1}^2/2(0.021\pm0.001)^2}$	1.971

Appendix C

Kolmogorov Smirnov analysis

Here we list the Kolmogorov Smirnov test p-values obtained from the comparison between simulated FRB population and observed bursts at Parkes.

Tables C.1, C.2 and C.3 list the KS test p-values γ obtained from the comparison of the simulated parameters for NE, SFH and PL spatial densities with those from the observed population at Parkes.

All the Monte Carlo population synthesis simulations are performed for:

(a) host galaxy DM contribution $\beta = 0.1, 1.0, 10.0$,

(b) energy density spectral index $\alpha = -3.0, -1.5, 2.0$

(c) scattering model 2.

While we consider four different combinations for the intrinsic width and luminosity models (w1L1, w1L2, w2L1 and w2L2) for NE and SFH $n(z)$, we only consider w1L1 for PL $n(z)$ as the relative difference between the different intrinsic models is found to be negligible.

The observables $w_{\rm obs}$, $S_{\rm peak,obs}$ and $DM_{\rm tot}$ here are the independent parameters. The equivalent p-value $\gamma_{\rm eq} = \sqrt{\gamma^2_{w_{\rm obs}} + \gamma^2_{S_{\rm peak,obs}} + \gamma^2_{DM_{\rm tot}}}$ is used in order to test the agreement of simulated distribution with that obtained from actual observations.

Table C.1: *KS test p-values from the comparison of simulated FRB parameters with the observed Parkes FRBs.* The table lists the values for $w_{\rm obs}$, $S_{\rm peak,obs}$ and $DM_{\rm tot}$ of the NE non-repeating FRB population. The p-values are obtained for different β and α combinations with $\gamma_{\rm eq} = \sqrt{\gamma^2_{w_{\rm obs}} + \gamma^2_{S_{\rm peak,obs}} + \gamma^2_{DM_{\rm tot}}}$. The p-values for intrinsic width and luminosity models w1L1/w1L2/w2L1/w2L2 are listed for each entry.

$n(z)$	β	α	$\gamma_{w_{\rm obs}}$	$\gamma_{S_{\rm peak,obs}}$	$\gamma_{DM_{\rm tot}}$	$\gamma_{\rm eq}$
NE	0.1	-3.0	0.711/0.668/	0.154/0.165/	0.167/0.179/	0.431/0.410/
			0.659/0.689	0.147/0.167	0.189/0.173	0.405/0.421
	(1.0)		(0.810/0.678/	(0.183/0.172/	(0.405/0.394/	(0.533/0.464/
			0.770/0.665)	0.163/0.186)	0.296/0.394)	0.485/0.459)
	[10.0]		[0.569/0.581/	[0.006/0.007/	[0.008/0.010/	[0.329/0.336/
			0.581/0.567]	0.009/0.005]	0.006/0.010]	0.335/0.327]
		-1.5	0.542/0.536/	0.104/0.071/	0.040/0.073/	0.319/0.315/
			0.542/0.561	0.052/0.056	0.068/0.080	0.317/0.329
			(0.549/0.681/	(0.158/0.133/	(0.068/0.085/	(0.332/0.404/
			0.679/0.611)	0.137/0.141)	0.093/0.091)	0.404/0.366)
			[0.383/0.389/	[0.020/0.012/	[$1.60e-5$/$3.32e-5$/	[0.221/0.225/
			0.385/0.456]	0.014/0.014]	$2.16e-5$/$2.90e-5$]	0.222/0.263]
		2.0	0.014/0.021/	0.019/0.028/	$2.08e-4$/$9.20e-5$/	0.014/0.020/
			0.018/0.018	0.015/0.023	$1.27e-4$/$1.17e-4$	0.014/0.017
			(0.039/0.036/	(0.029/0.029/	($1.45e-4$/$1.61e-4$/	(0.028/0.027/
			0.029/0.025)	0.044/0.017)	$9.63e-5$/$5.97e-5$)	0.030/0.017)
			[0.013/0.012/	[0.012/0.014/	[$5.42e-7$/$4.07e-7$/	[0.010/0.011/
			0.013/0.012]	0.008/0.009]	$2.92e-7$/$1.04e-7$]	0.009/0.009]

Table C.2: *KS test p-values from the comparison of simulated FRB parameters with the observed Parkes FRBs.* The table lists the values for $w_{\rm obs}$, $S_{\rm peak,obs}$ and $DM_{\rm tot}$ of the SFH non-repeating FRB population. The p-values are obtained for different β and α combinations with $\gamma_{\rm eq} = \sqrt{\gamma^2_{w_{\rm obs}} + \gamma^2_{S_{\rm peak,obs}} + \gamma^2_{DM_{\rm tot}}}$. The p-values for intrinsic width and luminosity models w1L1/w1L2/w2L1/w2L2 are listed for each entry.

$n(z)$	β	α	$\gamma_{w_{\rm obs}}$	$\gamma_{S_{\rm peak,obs}}$	$\gamma_{DM_{\rm tot}}$	$\gamma_{\rm eq}$
SFH	0.1	-3.0	0.654/0.759/ 0.674/0.738	0.326/0.252/ 0.249/0.249	0.410/0.366/ 0.328/0.336	0.484/0.508/ 0.456/0.490
	(1.0)		(0.794/0.762/ 0.670/0.713)	(0.195/0.188/ 0.164/0.122)	(0.506/0.541/ 0.552/0.593)	(0.555/0.550/ 0.510/0.540)
	[10.0]		[0.583/0.577/ 0.594/0.584]	[0.001/0.001/ 0.001/0.002]	[0.023/0.025/ 0.014/0.016]	[0.337/0.333/ 0.343/0.337]
		-1.5	0.407/0.442/ 0.497/0.434	0.104/0.082/ 0.120/0.095	0.068/0.068/ 0.053/0.047	0.246/0.262/ 0.297/0.258
			(0.449/0.453/ 0.503/0.467)	(0.143/0.147/ 0.169/0.166)	(0.082/0.076/ 0.066/0.063)	(0.276/0.278/ 0.309/0.288)
			[0.320/0.366/ 0.361/0.465]	[0.006/0.008/ 0.010/0.007]	[$2.867e-5$/$3.400e-5$/ $2.599e-5$/$4.878e-5$]	[0.185/0.211/ 0.209/0.268]
		2.0	0.014/0.012/ 0.015/0.017	0.020/0.019/ 0.024/0.019	$3.787e-4$/$2.322e-4$/ $1.573e-4$/$4.214e-4$	0.014/0.013/ 0.016/0.015
			(0.055/0.051/ 0.079/0.076)	(0.051/0.071/ 0.055/0.057)	($7.375e-5$/$2.987e-4$/ $1.405e-4$/$1.538e-4$)	(0.043/0.050/ 0.056/0.055)
			[0.011/0.009/ 0.011/0.014]	[0.015/0.016/ 0.027/0.013]	[$7.295e-7$/$9.005e-7$/ $7.938e-7$/$9.391e-7$]	[0.011/0.011/ 0.017/0.011]

Table C.3: *KS test p-values from the comparison of simulated FRB parameters with the observed Parkes FRBs.* The table lists the p-values for $w_{\rm obs}$, $S_{\rm peak,obs}$ and $DM_{\rm tot}$ for PL population with varying $z_{\rm crit}$ or varying (α_l,α_u). The p-values for the PL population are obtained for cases 1-3. Only w1L1 intrinsic model is considered for the PL spatial density case. We assume scattering model 2 for all MC simulations.

PL $n(z)$	(α_l,α_u)	$z_{\rm crit}$	$\gamma_{w_{\rm obs}}$	$\gamma_{S_{\rm peak,obs}}$	$\gamma_{DM_{\rm tot}}$	$\gamma_{\rm eq}$
Case 1	(2.7,-2.9)	1.00	0.415	0.105	0.585	0.419
		(2.00)	(0.728)	(0.217)	(0.667)	(0.584)
		[3.00]	[0.481]	[0.071]	[0.070]	[0.284]
Case 2			0.730	0.266	0.462	0.522
			(0.909)	(0.216)	(0.830)	(0.722)
			[0.704]	[0.084]	[0.193]	[0.424]
Case 3			0.578	0.005	0.002	0.334
			(0.642)	(0.007)	(0.003)	(0.371)
			[0.516]	[0.007]	[0.015]	[0.298]
Case 1	(0,-3)	1.85	0.524	0.097	0.718	0.516
	{3,0}		{0.221}	{0.099}	{0.380}	{0.260}
	[0,0]		[0.395]	[0.070]	[0.494]	[0.367]
Case 2			0.597	0.128	0.794	0.578
			{0.479}	{0.183}	{0.531}	{0.426}
			[0.588]	[0.162]	[0.573]	[0.483]
Case 3			0.238	5.809×10^{-5}	0.127	0.156
			{0.128}	{0.032}	{0.006}	{0.076}
			[0.138]	$[1.678 \times 10^{-5}]$	[0.154]	[0.119]

Bibliography

[1] K. W. Bannister, R. M. Shannon, J. P. Macquart, C. Flynn, P. G. Edwards, M. O'Neill, S. Osłowski, M. Bailes, B. Zackay, N. Clarke, L. R. D'Addario, R. Dodson, P. J. Hall, A. Jameson, D. Jones, R. Navarro, J. T. Trinh, J. Allison, C. S. Anderson, M. Bell, A. P. Chippendale, J. D. Collier, G. Heald, I. Heywood, A. W. Hotan, K. Lee-Waddell, J. P. Madrid, J. Marvil, D. McConnell, A. Popping, M. A. Voronkov, M. T. Whiting, G. R. Allen, D. C. J. Bock, D. P. Brodrick, F. Cooray, D. R. DeBoer, P. J. Diamond, R. Ekers, R. G. Gough, G. A. Hampson, L. Harvey-Smith, S. G. Hay, D. B. Hayman, C. A. Jackson, S. Johnston, B. S. Koribalski, N. M. McClure-Griffiths, P. Mirtschin, A. Ng, R. P. Norris, S. E. Pearce, C. J. Phillips, D. N. Roxby, E. R. Troup, and T. Westmeier. The Detection of an Extremely Bright Fast Radio Burst in a Phased Array Feed Survey. *ApJL*, 841(1):L12, May 2017.

[2] K. W. Bannister, A. T. Deller, C. Phillips, J. P. Macquart, J. X. Prochaska, N. Tejos, S. D. Ryder, E. M. Sadler, R. M. Shannon, S. Simha, C. K. Day, M. McQuinn, F. O. North-Hickey, S. Bhandari, W. R. Arcus, V. N. Bennert, J. Burchett, M. Bouwhuis, R. Dodson, R. D. Ekers, W. Farah, C. Flynn, C. W. James, M. Kerr, E. Lenc, E. K. Mahony, J. O'Meara, S. Osłowski, H. Qiu, T. Treu, V. U, T. J. Bateman, D. C. J. Bock, R. J. Bolton, A. Brown, J. D. Bunton, A. P. Chippendale, F. R. Cooray, T. Cornwell, N. Gupta, D. B. Hayman, M. Kesteven, B. S. Koribalski, A. MacLeod, N. M. McClure-Griffiths, S. Neuhold, R. P. Norris, M. A. Pilawa, R. Y. Qiao, J. Reynolds,

D. N. Roxby, T. W. Shimwell, M. A. Voronkov, and C. D. Wilson. A single fast radio burst localized to a massive galaxy at cosmological distance. *Science*, 365(6453):565–570, August 2019.

[3] C. G. Bassa, S. P. Tendulkar, E. A. K. Adams, N. Maddox, S. Bogdanov, G. C. Bower, S. Burke-Spolaor, B. J. Butler, S. Chatterjee, J. M. Cordes, J. W. T. Hessels, V. M. Kaspi, C. J. Law, B. Marcote, Z. Paragi, S. M. Ransom, P. Scholz, L. G. Spitler, and H. J. van Langevelde. FRB 121102 Is Coincident with a Star-forming Region in Its Host Galaxy. *ApJL*, 843(1):L8, July 2017.

[4] Apurba Bera, Siddhartha Bhattacharyya, Somnath Bharadwaj, N. D. Ramesh Bhat, and Jayaram N. Chengalur. On modelling the Fast Radio Burst population and event rate predictions. *MNRAS*, 457(3):2530–2539, April 2016.

[5] S. Bhandari, E. F. Keane, E. D. Barr, A. Jameson, E. Petroff, S. Johnston, M. Bailes, N. D. R. Bhat, M. Burgay, S. Burke-Spolaor, M. Caleb, R. P. Eatough, C. Flynn, J. A. Green, F. Jankowski, M. Kramer, V. Venkatraman Krishnan, V. Morello, A. Possenti, B. Stappers, C. Tiburzi, W. van Straten, I. Andreoni, T. Butterley, P. Chand ra, J. Cooke, A. Corongiu, D. M. Coward, V. S. Dhillon, R. Dodson, L. K. Hardy, E. J. Howell, P. Jaroenjittichai, A. Klotz, S. P. Littlefair, T. R. Marsh, M. Mickaliger, T. Muxlow, D. Perrodin, T. Pritchard, U. Sawangwit, T. Terai, N. Tominaga, P. Torne, T. Totani, A. Trois, D. Turpin, Y. Niino, R. W. Wilson, A. Albert, M. André, M. Anghinolfi, G. Anton, M. Ardid, J. J. Aubert, T. Avgitas, B. Baret, J. Barrios-Martí, S. Basa, B. Belhorma, V. Bertin, S. Biagi, R. Bormuth, S. Bourret, M. C. Bouwhuis, H. Brânzaș, R. Bruijn, J. Brunner, J. Busto,

A. Capone, L. Caramete, J. Carr, S. Celli, R. Cherkaoui El Moursli, T. Chiarusi, M. Circella, J. A. B. Coelho, A. Coleiro, R. Coniglione, H. Costantini, P. Coyle, A. Creusot, A. F. Díaz, A. Deschamps, G. De Bonis, C. Distefano, I. Di Palma, A. Domi, C. Donzaud, D. Dornic, D. Drouhin, T. Eberl, I. El Bojaddaini, N. El Khayati, D. Elsässer, A. Enzenhöfer, A. Ettahiri, F. Fassi, I. Felis, L. A. Fusco, P. Gay, V. Giordano, H. Glotin, T. Gregoire, R. Gracia-Ruiz, K. Graf, S. Hallmann, H. van Haren, A. J. Heijboer, Y. Hello, J. J. Hernández-Rey, J. Hößl, J. Hofestädt, C. Hugon, G. Illuminati, C. W. James, M. de Jong, M. Jongen, M. Kadler, O. Kalekin, U. Katz, D. Kießling, A. Kouchner, M. Kreter, I. Kreykenbohm, V. Kulikovskiy, C. Lachaud, R. Lahmann, D. Lefèvre, E. Leonora, S. Loucatos, M. Marcelin, A. Margiotta, A. Marinelli, J. A. Martínez-Mora, R. Mele, K. Melis, T. Michael, P. Migliozzi, A. Moussa, S. Navas, E. Nezri, M. Organokov, G. E. Păvălaș, C. Pellegrino, C. Perrina, P. Piattelli, V. Popa, T. Pradier, L. Quinn, C. Racca, G. Riccobene, A. Sánchez-Losa, M. Saldaña, I. Salvadori, D. F. E. Samtleben, M. Sanguineti, P. Sapienza, F. Schüssler, C. Sieger, M. Spurio, Th Stolarczyk, M. Taiuti, Y. Tayalati, A. Trovato, D. Turpin, C. Tönnis, B. Vallage, V. Van Elewyck, F. Versari, D. Vivolo, A. Vizzocca, J. Wilms, J. D. Zornoza, and J. Zúñiga. The SUrvey for Pulsars and Extragalactic Radio Bursts - II. New FRB discoveries and their follow-up. *MNRAS*, 475(2):1427–1446, April 2018.

[6] N. D. Ramesh Bhat, James M. Cordes, Fernando Camilo, David J. Nice, and Duncan R. Lorimer. Multifrequency Observations of Radio Pulse Broadening and Constraints on Interstellar Electron Density Microstructure. *ApJ*, 605(2):759–783, April 2004.

[7] Mukul Bhattacharya, Pawan Kumar, and Duncan Lorimer. Population modelling of FRBs from intrinsic properties. *arXiv e-prints*, page arXiv:1902.10225, February 2019.

[8] Mukul Bhattacharya. Constraining FRB progenitors from flux distribution. *arXiv e-prints*, page arXiv:1907.11992, July 2019.

[9] M. Caleb, C. Flynn, M. Bailes, E. D. Barr, T. Bateman, S. Bhandari, D. Campbell-Wilson, A. J. Green, R. W. Hunstead, A. Jameson, F. Jankowski, E. F. Keane, V. Ravi, W. van Straten, and V. Venkataraman Krishnan. Fast Radio Transient searches with UTMOST at 843 MHz. *MNRAS*, 458(1):718–725, May 2016.

[10] D. J. Champion, E. Petroff, M. Kramer, M. J. Keith, M. Bailes, E. D. Barr, S. D. Bates, N. D. R. Bhat, M. Burgay, S. Burke-Spolaor, C. M. L. Flynn, A. Jameson, S. Johnston, C. Ng, L. Levin, A. Possenti, B. W. Stappers, W. van Straten, D. Thornton, C. Tiburzi, and A. G. Lyne. Five new fast radio bursts from the HTRU high-latitude survey at Parkes: first evidence for two-component bursts. *MNRAS*, 460(1):L30–L34, July 2016.

[11] S. Chatterjee, C. J. Law, R. S. Wharton, S. Burke-Spolaor, J. W. T. Hessels, G. C. Bower, J. M. Cordes, S. P. Tendulkar, C. G. Bassa, P. Demorest, B. J. Butler, A. Seymour, P. Scholz, M. W. Abruzzo, S. Bogdanov, V. M. Kaspi, A. Keimpema, T. J. W. Lazio, B. Marcote, M. A. McLaughlin, Z. Paragi, S. M. Ransom, M. Rupen, L. G. Spitler, and H. J. van Langevelde. A direct localization of a fast radio burst and its host. *Nature*, 541(7635):58–61, January 2017.

[12] CHIME/FRB Collaboration, M. Amiri, K. Bandura, M. Bhardwaj, P. Boubel, M. M. Boyce, P. J Boyle, C. . Brar, M. Burhanpurkar, T. Cassanelli, P. Chawla, J. F. Cliche, D. Cubranic, M. Deng, N. Denman, M. Dobbs, M. Fandino, E. Fonseca, B. M. Gaensler, A. J. Gilbert, A. Gill, U. Giri, D. C. Good, M. Halpern, D. S. Hanna, A. S. Hill, G. Hinshaw, C. Höfer, A. Josephy, V. M. Kaspi, T. L. Landecker, D. A. Lang, H. H. Lin, K. W. Masui, R. Mckinven, J. Mena-Parra, M. Merryfield, D. Michilli, N. Milutinovic, C. Moatti, A. Naidu, L. B. Newburgh, C. Ng, C. Patel, U. Pen, T. Pinsonneault-Marotte, Z. Pleunis, M. Rafiei-Ravandi, M. Rahman, S. M. Ransom, A. Renard, P. Scholz, J. R. Shaw, S. R. Siegel, K. M. Smith, I. H. Stairs, S. P. Tendulkar, I. Tretyakov, K. Vanderlinde, and P. Yadav. A second source of repeating fast radio bursts. *Nature*, 566(7743):235–238, January 2019.

[13] Liam Connor, Jonathan Sievers, and Ue-Li Pen. Non-cosmological FRBs from young supernova remnant pulsars. *MNRAS*, 458(1):L19–L23, May 2016.

[14] J. M. Cordes, R. S. Wharton, L. G. Spitler, S. Chatterjee, and I. Wasserman. Radio Wave Propagation and the Provenance of Fast Radio Bursts. *arXiv e-prints*, page arXiv:1605.05890, May 2016.

[15] J. M. Cordes and Ira Wasserman. Supergiant pulses from extragalactic neutron stars. *MNRAS*, 457(1):232–257, March 2016.

[16] J. M. Cordes and T. J. W. Lazio. NE2001.I. A New Model for the Galactic Distribution of Free Electrons and its Fluctuations. *arXiv e-prints*, pages

astro–ph/0207156, July 2002.

[17] Wei Deng and Bing Zhang. Cosmological Implications of Fast Radio Burst/Gamma-Ray Burst Associations. *ApJL*, 783(2):L35, March 2014.

[18] K. Dolag, B. M. Gaensler, A. M. Beck, and M. C. Beck. Constraints on the distribution and energetics of fast radio bursts using cosmological hydrodynamic simulations. *MNRAS*, 451(4):4277–4289, August 2015.

[19] Heino Falcke and Luciano Rezzolla. Fast radio bursts: the last sign of supramassive neutron stars. *A&A*, 562:A137, February 2014.

[20] W. Farah, C. Flynn, M. Bailes, A. Jameson, K. W. Bannister, E. D. Barr, T. Bateman, S. Bhand ari, M. Caleb, D. Campbell-Wilson, S. W. Chang, A. Deller, A. J. Green, R. Hunstead, F. Jankowski, E. Keane, J. P. Macquart, A. Möller, C. A. Onken, S. Osłowski, A. Parthasarathy, K. Plant, V. Ravi, R. M. Shannon, B. E. Tucker, V. Venkatraman Krishnan, and C. Wolf. FRB microstructure revealed by the real-time detection of FRB170827. *MNRAS*, 478(1):1209–1217, July 2018.

[21] V. Gajjar, A. P. V. Siemion, D. C. Price, C. J. Law, D. Michilli, J. W. T. Hessels, S. Chatterjee, A. M. Archibald, G. C. Bower, C. Brinkman, S. Burke-Spolaor, J. M. Cordes, S. Croft, J. Emilio Enriquez, G. Foster, N. Gizani, G. Hellbourg, H. Isaacson, V. M. Kaspi, T. J. W. Lazio, M. Lebofsky, R. S. Lynch, D. MacMahon, M. A. McLaughlin, S. M. Ransom, P. Scholz, A. Seymour, L. G. Spitler, S. P. Tendulkar, D. Werthimer, and Y. G. Zhang. Highest Frequency Detection of FRB 121102 at 4-8 GHz Using the Breakthrough

Listen Digital Backend at the Green Bank Telescope. *ApJ*, 863(1):2, August 2018.

[22] He Gao, Zhuo Li, and Bing Zhang. Fast Radio Burst/Gamma-Ray Burst Cosmography. *ApJ*, 788(2):189, June 2014.

[23] L. K. Hardy, V. S. Dhillon, L. G. Spitler, S. P. Littlefair, R. P. Ashley, A. De Cia, M. J. Green, P. Jaroenjittichai, E. F. Keane, P. Kerry, M. Kramer, D. Malesani, T. R. Marsh, S. G. Parsons, A. Possenti, S. Rattanasoon, and D. I. Sahman. A search for optical bursts from the repeating fast radio burst FRB 121102. *MNRAS*, 472(3):2800–2807, December 2017.

[24] T. E. Hassall, E. F. Keane, and R. P. Fender. Detecting highly dispersed bursts with next-generation radio telescopes. *MNRAS*, 436(1):371–379, November 2013.

[25] J. W. T. Hessels, L. G. Spitler, A. D. Seymour, J. M. Cordes, D. Michilli, R. S. Lynch, K. Gourdji, A. M. Archibald, C. G. Bassa, G. C. Bower, S. Chatterjee, L. Connor, F. Crawford, J. S. Deneva, V. Gajjar, V. M. Kaspi, A. Keimpema, C. J. Law, B. Marcote, M. A. McLaughlin, Z. Paragi, E. Petroff, S. M. Ransom, P. Scholz, B. W. Stappers, and S. P. Tendulkar. FRB 121102 Bursts Show Complex Time-Frequency Structure. *ApJL*, 876(2):L23, May 2019.

[26] Susumu Inoue. Probing the cosmic reionization history and local environment of gamma-ray bursts through radio dispersion. *MNRAS*, 348(3):999–1008, March 2004.

[27] Kunihito Ioka. The Cosmic Dispersion Measure from Gamma-Ray Burst Afterglows: Probing the Reionization History and the Burst Environment. *ApJL*, 598(2):L79–L82, December 2003.

[28] Kazumi Kashiyama, Kunihito Ioka, and Peter Mészáros. Cosmological Fast Radio Bursts from Binary White Dwarf Mergers. *ApJL*, 776(2):L39, October 2013.

[29] Kazumi Kashiyama and Kohta Murase. Testing the Young Neutron Star Scenario with Persistent Radio Emission Associated with FRB 121102. *ApJL*, 839(1):L3, April 2017.

[30] J. I. Katz. How Soft Gamma Repeaters Might Make Fast Radio Bursts. *ApJ*, 826(2):226, August 2016.

[31] E. F. Keane, B. W. Stappers, M. Kramer, and A. G. Lyne. On the origin of a highly dispersed coherent radio burst. *MNRAS*, 425(1):L71–L75, September 2012.

[32] E. F. Keane, S. Johnston, S. Bhandari, E. Barr, N. D. R. Bhat, M. Burgay, M. Caleb, C. Flynn, A. Jameson, M. Kramer, E. Petroff, A. Possenti, W. van Straten, M. Bailes, S. Burke-Spolaor, R. P. Eatough, B. W. Stappers, T. Totani, M. Honma, H. Furusawa, T. Hattori, T. Morokuma, Y. Niino, H. Sugai, T. Terai, N. Tominaga, S. Yamasaki, N. Yasuda, R. Allen, J. Cooke, J. Jencson, M. M. Kasliwal, D. L. Kaplan, S. J. Tingay, A. Williams, R. Wayth, P. Chandra, D. Perrodin, M. Berezina, M. Mickaliger, and C. Bassa. The host galaxy of a fast radio burst. *Nature*, 530(7591):453–456, February 2016.

[33] E. F. Keane and E. Petroff. Fast radio bursts: search sensitivities and completeness. *MNRAS*, 447(3):2852–2856, March 2015.

[34] M. A. Krishnakumar, D. Mitra, A. Naidu, B. C. Joshi, and P. K. Manoharan. Scatter Broadening Measurements of 124 Pulsars At 327 Mhz. *ApJ*, 804(1):23, May 2015.

[35] S. R. Kulkarni, E. O. Ofek, J. D. Neill, Z. Zheng, and M. Juric. Giant Sparks at Cosmological Distances? *ApJ*, 797(1):70, December 2014.

[36] Pawan Kumar, Wenbin Lu, and Mukul Bhattacharya. Fast radio burst source properties and curvature radiation model. *MNRAS*, 468(3):2726–2739, July 2017.

[37] C. J. Law, M. W. Abruzzo, C. G. Bassa, G. C. Bower, S. Burke-Spolaor, B. J. Butler, T. Cantwell, S. H. Carey, S. Chatterjee, J. M. Cordes, P. Demorest, J. Dowell, R. Fender, K. Gourdji, K. Grainge, J. W. T. Hessels, J. Hickish, V. M. Kaspi, T. J. W. Lazio, M. A. McLaughlin, D. Michilli, K. Mooley, Y. C. Perrott, S. M. Ransom, N. Razavi-Ghods, M. Rupen, A. Scaife, P. Scott, P. Scholz, A. Seymour, L. G. Spitler, K. Stovall, S. P. Tendulkar, D. Titterington, R. S. Wharton, and P. K. G. Williams. A Multi-telescope Campaign on FRB 121102: Implications for the FRB Population. *ApJ*, 850(1):76, November 2017.

[38] Earl Lawrence, Scott Vander Wiel, Casey Law, Sarah Burke Spolaor, and Geoffrey C. Bower. The Nonhomogeneous Poisson Process for Fast Radio Burst Rates. *AJ*, 154(3):117, September 2017.

[39] A. Loeb, Y. Shvartzvald, and D. Maoz. Fast radio bursts may originate from nearby flaring stars. *MNRAS*, 439:L46–L50, March 2014.

[40] D. R. Lorimer, M. Bailes, M. A. McLaughlin, D. J. Narkevic, and F. Crawford. A Bright Millisecond Radio Burst of Extragalactic Origin. *Science*, 318(5851):777, November 2007.

[41] D. R. Lorimer, A. Karastergiou, M. A. McLaughlin, and S. Johnston. On the detectability of extragalactic fast radio transients. *MNRAS*, 436:L5–L9, November 2013.

[42] Wenbin Lu and Pawan Kumar. On the radiation mechanism of repeating fast radio bursts. *MNRAS*, 477(2):2470–2493, June 2018.

[43] Yu. Lyubarsky. A model for fast extragalactic radio bursts. *MNRAS*, 442:L9–L13, July 2014.

[44] Maxim Lyutikov, Lukasz Burzawa, and Sergei B. Popov. Fast radio bursts as giant pulses from young rapidly rotating pulsars. *MNRAS*, 462(1):941–950, October 2016.

[45] Jean-Pierre Macquart and Jun Yi Koay. Temporal Smearing of Transient Radio Sources by the Intergalactic Medium. *ApJ*, 776(2):125, October 2013.

[46] J. P. Macquart, R. M. Shannon, K. W. Bannister, C. W. James, R. D. Ekers, and J. D. Bunton. The Spectral Properties of the Bright Fast Radio Burst Population. *ApJL*, 872(2):L19, February 2019.

[47] J. P. Macquart and R. D. Ekers. Fast radio burst event rate counts - I. Interpreting the observations. *MNRAS*, 474(2):1900–1908, February 2018.

[48] Piero Madau and Mark Dickinson. Cosmic Star-Formation History. *ARA&A*, 52:415–486, August 2014.

[49] B. Marcote, Z. Paragi, J. W. T. Hessels, A. Keimpema, H. J. van Langevelde, Y. Huang, C. G. Bassa, S. Bogdanov, G. C. Bower, S. Burke-Spolaor, B. J. Butler, R. M. Campbell, S. Chatterjee, J. M. Cordes, P. Demorest, M. A. Garrett, T. Ghosh, V. M. Kaspi, C. J. Law, T. J. W. Lazio, M. A. McLaughlin, S. M. Ransom, C. J. Salter, P. Scholz, A. Seymour, A. Siemion, L. G. Spitler, S. P. Tendulkar, and R. S. Wharton. The Repeating Fast Radio Burst FRB 121102 as Seen on Milliarcsecond Angular Scales. *ApJL*, 834(2):L8, January 2017.

[50] B. Marcote, K. Nimmo, J. W. T. Hessels, S. P. Tendulkar, C. G. Bassa, Z. Paragi, A. Keimpema, M. Bhardwaj, R. Karuppusamy, V. M. Kaspi, C. J. Law, D. Michilli, K. Aggarwal, B. Andersen, A. M. Archibald, K. Bandura, G. C. Bower, P. J. Boyle, C. Brar, S. Burke-Spolaor, B. J. Butler, T. Cassanelli, P. Chawla, P. Demorest, M. Dobbs, E. Fonseca, U. Giri, D. C. Good, K. Gourdji, A. Josephy, A. Yu. Kirichenko, F. Kirsten, T. L. Landecker, D. Lang, T. J. W. Lazio, D. Z. Li, H. H. Lin, J. D. Linford, K. Masui, J. Mena-Parra, A. Naidu, C. Ng, C. Patel, U. L. Pen, Z. Pleunis, M. Rafiei-Ravandi, M. Rahman, A. Renard, P. Scholz, S. R. Siegel, K. M. Smith, I. H. Stairs, K. Vanderlinde, and A. V. Zwaniga. A repeating fast radio burst source localized to a nearby spiral galaxy. *Nature*, 577(7789):190–194, January 2020.

[51] Kiyoshi Masui, Hsiu-Hsien Lin, Jonathan Sievers, Christopher J. Anderson, Tzu-Ching Chang, Xuelei Chen, Apratim Ganguly, Miranda Jarvis, Cheng-

Yu Kuo, Yi-Chao Li, Yu-Wei Liao, Maura McLaughlin, Ue-Li Pen, Jeffrey B. Peterson, Alexander Roman, Peter T. Timbie, Tabitha Voytek, and Jaswant K. Yadav. Dense magnetized plasma associated with a fast radio burst. *Nature*, 528(7583):523–525, December 2015.

[52] Matthew McQuinn. Locating the "Missing" Baryons with Extragalactic Dispersion Measure Estimates. *ApJL*, 780(2):L33, January 2014.

[53] Brian D. Metzger, Edo Berger, and Ben Margalit. Millisecond Magnetar Birth Connects FRB 121102 to Superluminous Supernovae and Long-duration Gamma-Ray Bursts. *ApJ*, 841(1):14, May 2017.

[54] D. Michilli, A. Seymour, J. W. T. Hessels, L. G. Spitler, V. Gajjar, A. M. Archibald, G. C. Bower, S. Chatterjee, J. M. Cordes, K. Gourdji, G. H. Heald, V. M. Kaspi, C. J. Law, C. Sobey, E. A. K. Adams, C. G. Bassa, S. Bogdanov, C. Brinkman, P. Demorest, F. Fernand ez, G. Hellbourg, T. J. W. Lazio, R. S. Lynch, N. Maddox, B. Marcote, M. A. McLaughlin, Z. Paragi, S. M. Ransom, P. Scholz, A. P. V. Siemion, S. P. Tendulkar, P. van Rooy, R. S. Wharton, and D. Whitlow. An extreme magneto-ionic environment associated with the fast radio burst source FRB 121102. *Nature*, 553(7687):182–185, January 2018.

[55] F. Mottez and P. Zarka. Radio emissions from pulsar companions: a refutable explanation for galactic transients and fast radio bursts. *A&A*, 569:A86, September 2014.

[56] Yuu Niino. Fast Radio Bursts' Recipes for the Distributions of Dispersion Measures, Flux Densities, and Fluences. *ApJ*, 858(1):4, May 2018.

[57] Niels Oppermann, Hao-Ran Yu, and Ue-Li Pen. On the non-Poissonian repetition pattern of FRB121102. *MNRAS*, 475(4):5109–5115, April 2018.

[58] E. Petroff, S. Johnston, E. F. Keane, W. van Straten, M. Bailes, E. D. Barr, B. R. Barsdell, S. Burke-Spolaor, M. Caleb, D. J. Champion, C. Flynn, A. Jameson, M. Kramer, C. Ng, A. Possenti, and B. W. Stappers. A survey of FRB fields: limits on repeatability. *MNRAS*, 454(1):457–462, November 2015.

[59] E. Petroff, E. D. Barr, A. Jameson, E. F. Keane, M. Bailes, M. Kramer, V. Morello, D. Tabbara, and W. van Straten. FRBCAT: The Fast Radio Burst Catalogue. *PASA*, 33:e045, September 2016.

[60] E. Petroff, S. Burke-Spolaor, E. F. Keane, M. A. McLaughlin, R. Miller, I. Andreoni, M. Bailes, E. D. Barr, S. R. Bernard, S. Bhandari, N. D. R. Bhat, M. Burgay, M. Caleb, D. Champion, P. Chandra, J. Cooke, V. S. Dhillon, J. S. Farnes, L. K. Hardy, P. Jaroenjittichai, S. Johnston, M. Kasliwal, M. Kramer, S. P. Littlefair, J. P. Macquart, M. Mickaliger, A. Possenti, T. Pritchard, V. Ravi, A. Rest, A. Rowlinson, U. Sawangwit, B. Stappers, M. Sullivan, C. Tiburzi, W. van Straten, ANTARES Collaboration, A. Albert, M. André, M. Anghinolfi, G. Anton, M. Ardid, J. J. Aubert, T. Avgitas, B. Baret, J. Barrios-Martí, S. Basa, V. Bertin, S. Biagi, R. Bormuth, S. Bourret, M. C. Bouwhuis, R. Bruijn, J. Brunner, J. Busto, A. Capone, L. Caramete, J. Carr, S. Celli, T. Chiarusi, M. Circella, J. A. B. Coelho, A. Coleiro, R. Coniglione, H. Costantini, P. Coyle, A. Creusot, A. Deschamps, G. de Bonis, C. Distefano, I. di Palma, C. Donzaud, D. Dornic, D. Drouhin, T. Eberl, I. El Bojaddaini, D. Elsässer, A. Enzenhöfer, I. Felis, L. A. Fusco, S. Galatà,

P. Gay, S. Geißelsöder, K. Geyer, V. Giordano, A. Gleixner, H. Glotin, T. Grégoire, R. Gracia-Ruiz, K. Graf, S. Hallmann, H. van Haren, A. J. Heijboer, Y. Hello, J. J. Hernández-Rey, J. Hößl, J. Hofestädt, C. Hugon, G. Illuminati, C. W. James, M. de Jong, M. Jongen, M. Kadler, O. Kalekin, U. Katz, D. Kießling, A. Kouchner, M. Kreter, I. Kreykenbohm, V. Kulikovskiy, C. Lachaud, R. Lahmann, D. Lefèvre, E. Leonora, M. Lotze, S. Loucatos, M. Marcelin, A. Margiotta, A. Marinelli, J. A. Martínez-Mora, A. Mathieu, R. Mele, K. Melis, T. Michael, P. Migliozzi, A. Moussa, C. Mueller, E. Nezri, G. E. Păvălaș, C. Pellegrino, C. Perrina, P. Piattelli, V. Popa, T. Pradier, L. Quinn, C. Racca, G. Riccobene, K. Roensch, A. Sánchez-Losa, M. Saldaña, I. Salvadori, D. F. E. Samtleben, M. Sanguineti, P. Sapienza, J. Schnabel, T. Seitz, C. Sieger, M. Spurio, Th. Stolarczyk, M. Taiuti, Y. Tayalati, A. Trovato, M. Tselengidou, D. Turpin, C. Tönnis, B. Vallage, C. Vallée, V. van Elewyck, D. Vivolo, A. Vizzoca, S. Wagner, J. Wilms, J. D. Zornoza, J. Zúñiga, H. E. S. S. Collaboration, H. Abdalla, A. Abramowski, F. Aharonian, F. Ait Benkhali, A. G. Akhperjanian, T. Andersson, E. O. Angüner, M. Arrieta, P. Aubert, M. Backes, A. Balzer, M. Barnard, Y. Becherini, J. Becker Tjus, D. Berge, S. Bernhard, K. Bernlöhr, R. Blackwell, M. Böttcher, C. Boisson, J. Bolmont, P. Bordas, J. Bregeon, F. Brun, P. Brun, M. Bryan, T. Bulik, M. Capasso, S. Casanova, M. Cerruti, N. Chakraborty, R. Chalme-Calvet, R. C. G. Chaves, A. Chen, J. Chevalier, M. Chrétien, S. Colafrancesco, G. Cologna, B. Condon, J. Conrad, Y. Cui, I. D. Davids, J. Decock, B. Degrange, C. Deil, J. Devin, P. Dewilt, L. Dirson, A. Djannati-Ataï, W. Domainko, A. Donath, L. O'c. Drury, G. Dubus, K. Dutson, J. Dyks, T. Edwards, K. Egberts, P. Eger, J. P. Ernenwein, S. Eschbach, C. Farnier, S. Fe-

gan, M. V. Fernandes, A. Fiasson, G. Fontaine, A. Förster, S. Funk, M. Füßling, S. Gabici, M. Gajdus, Y. A. Gallant, T. Garrigoux, G. Giavitto, B. Giebels, J. F. Glicenstein, D. Gottschall, A. Goyal, M. H. Grondin, D. Hadasch, J. Hahn, M. Haupt, J. Hawkes, G. Heinzelmann, G. Henri, G. Hermann, O. Hervet, J. A. Hinton, W. Hofmann, C. Hoischen, M. Holler, D. Horns, A. Ivascenko, A. Jacholkowska, M. Jamrozy, M. Janiak, D. Jankowsky, F. Jankowsky, M. Jingo, T. Jogler, L. Jouvin, I. Jung-Richardt, M. A. Kastendieck, K. Katarzyński, D. Kerszberg, B. Khélifi, M. Kieffer, J. King, S. Klepser, D. Klochkov, W. Kluźniak, D. Kolitzus, Nu. Komin, K. Kosack, S. Krakau, M. Kraus, F. Krayzel, P. P. Krüger, H. Laffon, G. Lamanna, J. Lau, J. P. Lees, J. Lefaucheur, V. Lefranc, A. Lemière, M. Lemoine-Goumard, J. P. Lenain, E. Leser, T. Lohse, M. Lorentz, R. Liu, R. López-Coto, I. Lypova, V. Marandon, A. Marcowith, C. Mariaud, R. Marx, G. Maurin, N. Maxted, M. Mayer, P. J. Meintjes, M. Meyer, A. M. W. Mitchell, R. Moderski, M. Mohamed, L. Mohrmann, K. Morâ, E. Moulin, T. Murach, M. de Naurois, F. Niederwanger, J. Niemiec, L. Oakes, P. O'Brien, H. Odaka, S. Öttl, S. Ohm, M. Ostrowski, I. Oya, M. Padovani, M. Panter, R. D. Parsons, N. W. Pekeur, G. Pelletier, C. Perennes, P. O. Petrucci, B. Peyaud, Q. Piel, S. Pita, H. Poon, D. Prokhorov, H. Prokoph, G. Pühlhofer, M. Punch, A. Quirrenbach, S. Raab, A. Reimer, O. Reimer, M. Renaud, R. De Los Reyes, F. Rieger, C. Romoli, S. Rosier-Lees, G. Rowell, B. Rudak, C. B. Rulten, V. Sahakian, D. Salek, D. A. Sanchez, A. Santangelo, M. Sasaki, R. Schlickeiser, A. Schulz, F. Schüssler, U. Schwanke, S. Schwemmer, M. Settimo, A. S. Seyffert, N. Shafi, I. Shilon, R. Simoni, H. Sol, F. Spanier, G. Spengler, F. Spies, Ł. Stawarz, R. Steenkamp, C. Stegmann, F. Stinzing, K. Stycz, I. Sushch, J. P. Tavernet, T. Tavernier, A. M. Tay-

lor, R. Terrier, L. Tibaldo, D. Tiziani, M. Tluczykont, C. Trichard, R. Tuffs, Y. Uchiyama, D. J. Van Der Walt, C. van Eldik, C. van Rensburg, B. van Soelen, G. Vasileiadis, J. Veh, C. Venter, A. Viana, P. Vincent, J. Vink, F. Voisin, H. J. Völk, T. Vuillaume, Z. Wadiasingh, S. J. Wagner, P. Wagner, R. M. Wagner, R. White, A. Wierzcholska, P. Willmann, A. Wörnlein, D. Wouters, R. Yang, V. Zabalza, D. Zaborov, M. Zacharias, R. Zanin, A. A. Zdziarski, A. Zech, F. Zefi, A. Ziegler, and N. Żywucka. A polarized fast radio burst at low Galactic latitude. *MNRAS*, 469(4):4465–4482, August 2017.

[61] E. Petroff, J. W. T. Hessels, and D. R. Lorimer. Fast radio bursts. *A&ARv*, 27(1):4, May 2019.

[62] Anthony L. Piro. Magnetic Interactions in Coalescing Neutron Star Binaries. *ApJ*, 755(1):80, August 2012.

[63] Planck Collaboration, P. A. R. Ade, N. Aghanim, C. Armitage-Caplan, M. Arnaud, M. Ashdown, F. Atrio-Barand ela, J. Aumont, C. Baccigalupi, A. J. Banday, R. B. Barreiro, J. G. Bartlett, E. Battaner, K. Benabed, A. Benoît, A. Benoit-Lévy, J. P. Bernard, M. Bersanelli, P. Bielewicz, J. Bobin, J. J. Bock, A. Bonaldi, J. R. Bond, J. Borrill, F. R. Bouchet, M. Bridges, M. Bucher, C. Burigana, R. C. Butler, E. Calabrese, B. Cappellini, J. F. Cardoso, A. Catalano, A. Challinor, A. Chamballu, R. R. Chary, X. Chen, H. C. Chiang, L. Y. Chiang, P. R. Christensen, S. Church, D. L. Clements, S. Colombi, L. P. L. Colombo, F. Couchot, A. Coulais, B. P. Crill, A. Curto, F. Cuttaia, L. Danese, R. D. Davies, R. J. Davis, P. de Bernardis, A. de Rosa, G. de Zotti, J. Delabrouille, J. M. Delouis, F. X. Désert, C. Dickinson, J. M.

Diego, K. Dolag, H. Dole, S. Donzelli, O. Doré, M. Douspis, J. Dunkley, X. Dupac, G. Efstathiou, F. Elsner, T. A. Enßlin, H. K. Eriksen, F. Finelli, O. Forni, M. Frailis, A. A. Fraisse, E. Franceschi, T. C. Gaier, S. Galeotta, S. Galli, K. Ganga, M. Giard, G. Giardino, Y. Giraud-Héraud, E. Gjerløw, J. González-Nuevo, K. M. Górski, S. Gratton, A. Gregorio, A. Gruppuso, J. E. Gudmundsson, J. Haissinski, J. Hamann, F. K. Hansen, D. Hanson, D. Harrison, S. Henrot-Versillé, C. Hernández-Monteagudo, D. Herranz, S. R. Hildebrand t, E. Hivon, M. Hobson, W. A. Holmes, A. Hornstrup, Z. Hou, W. Hovest, K. M. Huffenberger, A. H. Jaffe, T. R. Jaffe, J. Jewell, W. C. Jones, M. Juvela, E. Keihänen, R. Keskitalo, T. S. Kisner, R. Kneissl, J. Knoche, L. Knox, M. Kunz, H. Kurki-Suonio, G. Lagache, A. Lähteenmäki, J. M. Lamarre, A. Lasenby, M. Lattanzi, R. J. Laureijs, C. R. Lawrence, S. Leach, J. P. Leahy, R. Leonardi, J. León-Tavares, J. Lesgourgues, A. Lewis, M. Liguori, P. B. Lilje, M. Linden-Vørnle, M. López-Caniego, P. M. Lubin, J. F. Macías-Pérez, B. Maffei, D. Maino, N. Mand olesi, M. Maris, D. J. Marshall, P. G. Martin, E. Martínez-González, S. Masi, M. Massardi, S. Matarrese, F. Matthai, P. Mazzotta, P. R. Meinhold, A. Melchiorri, J. B. Melin, L. Mendes, E. Menegoni, A. Mennella, M. Migliaccio, M. Millea, S. Mitra, M. A. Miville-Deschênes, A. Moneti, L. Montier, G. Morgante, D. Mortlock, A. Moss, D. Munshi, J. A. Murphy, P. Naselsky, F. Nati, P. Natoli, C. B. Netterfield, H. U. Nørgaard-Nielsen, F. Noviello, D. Novikov, I. Novikov, I. J. O'Dwyer, S. Osborne, C. A. Oxborrow, F. Paci, L. Pagano, F. Pajot, R. Paladini, D. Paoletti, B. Partridge, F. Pasian, G. Patanchon, D. Pearson, T. J. Pearson, H. V. Peiris, O. Perdereau, L. Perotto, F. Perrotta, V. Pettorino, F. Piacentini, M. Piat, E. Pierpaoli, D. Pietrobon, S. Plaszczynski, P. Platania, E. Pointecouteau,

G. Polenta, N. Ponthieu, L. Popa, T. Poutanen, G. W. Pratt, G. Prézeau, S. Prunet, J. L. Puget, J. P. Rachen, W. T. Reach, R. Rebolo, M. Reinecke, M. Remazeilles, C. Renault, S. Ricciardi, T. Riller, I. Ristorcelli, G. Rocha, C. Rosset, G. Roudier, M. Rowan-Robinson, J. A. Rubiño-Martín, B. Rusholme, M. Sandri, D. Santos, M. Savelainen, G. Savini, D. Scott, M. D. Seiffert, E. P. S. Shellard, L. D. Spencer, J. L. Starck, V. Stolyarov, R. Stompor, R. Sudiwala, R. Sunyaev, F. Sureau, D. Sutton, A. S. Suur-Uski, J. F. Sygnet, J. A. Tauber, D. Tavagnacco, L. Terenzi, L. Toffolatti, M. Tomasi, M. Tristram, M. Tucci, J. Tuovinen, M. Türler, G. Umana, L. Valenziano, J. Valiviita, B. Van Tent, P. Vielva, F. Villa, N. Vittorio, L. A. Wade, B. D. Wandelt, I. K. Wehus, M. White, S. D. M. White, A. Wilkinson, D. Yvon, A. Zacchei, and A. Zonca. Planck 2013 results. XVI. Cosmological parameters. *A&A*, 571:A16, November 2014.

[64] E. Platts, A. Weltman, A. Walters, S. P. Tendulkar, J. E. B. Gordin, and S. Kandhai. A living theory catalogue for fast radio bursts. *Physics Reports*, 821:1–27, August 2019.

[65] Sergey B. Popov and K. A. Postnov. Hyperflares of SGRs as an engine for millisecond extragalactic radio bursts. In H. A. Harutyunian, A. M. Mickaelian, and Y. Terzian, editors, *Evolution of Cosmic Objects through their Physical Activity*, pages 129–132, November 2010.

[66] J. Xavier Prochaska and Yong Zheng. Probing Galactic haloes with fast radio bursts. *MNRAS*, 485(1):648–665, May 2019.

[67] J. Xavier Prochaska, Jean-Pierre Macquart, Matthew McQuinn, Sunil Simha,

Ryan M. Shannon, Cherie K. Day, Lachlan Marnoch, Stuart Ryder, Adam Deller, Keith W. Bannister, Shivani Bhandari, Rongmon Bordoloi, John Bunton, Hyerin Cho, Chris Flynn, Elizabeth K. Mahony, Chris Phillips, Hao Qiu, and Nicolas Tejos. The low density and magnetization of a massive galaxy halo exposed by a fast radio burst. *Science*, 366(6462):231–234, October 2019.

[68] A. Rane, D. R. Lorimer, S. D. Bates, N. McMann, M. A. McLaughlin, and K. Rajwade. A search for rotating radio transients and fast radio bursts in the Parkes high-latitude pulsar survey. *MNRAS*, 455(2):2207–2215, January 2016.

[69] V. Ravi, R. M. Shannon, and A. Jameson. A Fast Radio Burst in the Direction of the Carina Dwarf Spheroidal Galaxy. *ApJL*, 799(1):L5, January 2015.

[70] Vikram Ravi and Abraham Loeb. Explaining the Statistical Properties of Fast Radio Bursts with Suppressed Low-frequency Emission. *ApJ*, 874(1):72, March 2019.

[71] V. Ravi, M. Catha, L. D'Addario, S. G. Djorgovski, G. Hallinan, R. Hobbs, J. Kocz, S. R. Kulkarni, J. Shi, H. K. Vedantham, S. Weinreb, and D. P. Woody. A fast radio burst localised to a massive galaxy. *arXiv e-prints*, page arXiv:1907.01542, July 2019.

[72] P. Scholz, L. G. Spitler, J. W. T. Hessels, S. Chatterjee, J. M. Cordes, V. M. Kaspi, R. S. Wharton, C. G. Bassa, S. Bogdanov, F. Camilo, F. Crawford, J. Deneva, J. van Leeuwen, R. Lynch, E. C. Madsen, M. A. McLaughlin,

M. Mickaliger, E. Parent, C. Patel, S. M. Ransom, A. Seymour, I. H. Stairs, B. W. Stappers, and S. P. Tendulkar. The Repeating Fast Radio Burst FRB 121102: Multi-wavelength Observations and Additional Bursts. *ApJ*, 833(2):177, December 2016.

[73] P. Scholz, S. Bogdanov, J. W. T. Hessels, R. S. Lynch, L. G. Spitler, C. G. Bassa, G. C. Bower, S. Burke-Spolaor, B. J. Butler, S. Chatterjee, J. M. Cordes, K. Gourdji, V. M. Kaspi, C. J. Law, B. Marcote, M. A. McLaughlin, D. Michilli, Z. Paragi, S. M. Ransom, A. Seymour, S. P. Tendulkar, and R. S. Wharton. Simultaneous X-Ray, Gamma-Ray, and Radio Observations of the Repeating Fast Radio Burst FRB 121102. *ApJ*, 846(1):80, September 2017.

[74] R. M. Shannon, J. P. Macquart, K. W. Bannister, R. D. Ekers, C. W. James, S. Osłowski, H. Qiu, M. Sammons, A. W. Hotan, M. A. Voronkov, R. J. Beresford, M. Brothers, A. J. Brown, J. D. Bunton, A. P. Chippendale, C. Haskins, M. Leach, M. Marquarding, D. McConnell, M. A. Pilawa, E. M. Sadler, E. R. Troup, J. Tuthill, M. T. Whiting, J. R. Allison, C. S. Anderson, M. E. Bell, J. D. Collier, G. Gürkan, G. Heald, and C. J. Riseley. The dispersion-brightness relation for fast radio bursts from a wide-field survey. *Nature*, 562(7727):386–390, October 2018.

[75] J. Michael Shull and Charles W. Danforth. The Dispersion of Fast Radio Bursts from a Structured Intergalactic Medium at Redshifts z < 1.5. *ApJL*, 852(1):L11, January 2018.

[76] Britton D. Smith, Eric J. Hallman, J. Michael Shull, and Brian W. O'Shea. The Nature of the Warm/Hot Intergalactic Medium. I. Numerical Methods,

Convergence, and O VI Absorption. *ApJ*, 731(1):6, April 2011.

[77] L. G. Spitler, J. M. Cordes, J. W. T. Hessels, D. R. Lorimer, M. A. McLaughlin, S. Chatterjee, F. Crawford, J. S. Deneva, V. M. Kaspi, R. S. Wharton, B. Allen, S. Bogdanov, A. Brazier, F. Camilo, P. C. C. Freire, F. A. Jenet, C. Karako-Argaman, B. Knispel, P. Lazarus, K. J. Lee, J. van Leeuwen, R. Lynch, S. M. Ransom, P. Scholz, X. Siemens, I. H. Stairs, K. Stovall, J. K. Swiggum, A. Venkataraman, W. W. Zhu, C. Aulbert, and H. Fehrmann. Fast Radio Burst Discovered in the Arecibo Pulsar ALFA Survey. *ApJ*, 790(2):101, August 2014.

[78] L. G. Spitler, P. Scholz, J. W. T. Hessels, S. Bogdanov, A. Brazier, F. Camilo, S. Chatterjee, J. M. Cordes, F. Crawford, J. Deneva, R. D. Ferdman, P. C. C. Freire, V. M. Kaspi, P. Lazarus, R. Lynch, E. C. Madsen, M. A. McLaughlin, C. Patel, S. M. Ransom, A. Seymour, I. H. Stairs, B. W. Stappers, J. van Leeuwen, and W. W. Zhu. A repeating fast radio burst. *Nature*, 531(7593):202–205, March 2016.

[79] L. G. Spitler, W. Herrmann, G. C. Bower, S. Chatterjee, J. M. Cordes, J. W. T. Hessels, M. Kramer, D. Michilli, P. Scholz, A. Seymour, and A. P. V. Siemion. Detection of Bursts from FRB 121102 with the Effelsberg 100 m Radio Telescope at 5 GHz and the Role of Scintillation. *ApJ*, 863(2):150, August 2018.

[80] L. Staveley-Smith, W. E. Wilson, T. S. Bird, M. J. Disney, R. D. Ekers, K. C. Freeman, R. F. Haynes, M. W. Sinclair, R. A. Vaile, R. L. Webster,

and A. E. Wright. The Parkes 21 CM multibeam receiver. *PASA*, 13(3):243–248, November 1996.

[81] S. P. Tendulkar, C. G. Bassa, J. M. Cordes, G. C. Bower, C. J. Law, S. Chatterjee, E. A. K. Adams, S. Bogdanov, S. Burke-Spolaor, B. J. Butler, P. Demorest, J. W. T. Hessels, V. M. Kaspi, T. J. W. Lazio, N. Maddox, B. Marcote, M. A. McLaughlin, Z. Paragi, S. M. Ransom, P. Scholz, A. Seymour, L. G. Spitler, H. J. van Langevelde, and R. S. Wharton. The Host Galaxy and Redshift of the Repeating Fast Radio Burst FRB 121102. *ApJL*, 834(2):L7, January 2017.

[82] D. Thornton, B. Stappers, M. Bailes, B. Barsdell, S. Bates, N. D. R. Bhat, M. Burgay, S. Burke-Spolaor, D. J. Champion, P. Coster, N. D'Amico, A. Jameson, S. Johnston, M. Keith, M. Kramer, L. Levin, S. Milia, C. Ng, A. Possenti, and W. van Straten. A Population of Fast Radio Bursts at Cosmological Distances. *Science*, 341(6141):53–56, July 2013.

[83] Tomonori Totani. Cosmological Fast Radio Bursts from Binary Neutron Star Mergers. *PASJ*, 65:L12, October 2013.

[84] N. R. Vandenberg. Meter-wavelength VLBI. IV. Temporal and spatial scattering of the Crab nebula pulsar's radiation. *ApJ*, 209:578–583, October 1976.

[85] H. K. Vedantham, V. Ravi, G. Hallinan, and R. M. Shannon. The Fluence and Distance Distributions of Fast Radio Bursts. *ApJ*, 830(2):75, October 2016.

[86] Ian P. Williamson. Pulse broadening due to multiple scattering in the interstellarmedium. *MNRAS*, 157:55, January 1972.

[87] Bing Zhang. A Possible Connection between Fast Radio Bursts and Gamma-Ray Bursts. *ApJL*, 780(2):L21, January 2014.

[88] Bing Zhang. A "Cosmic Comb" Model of Fast Radio Bursts. *ApJL*, 836(2):L32, February 2017.

[89] Z. Zheng, E. O. Ofek, S. R. Kulkarni, J. D. Neill, and M. Juric. Probing the Intergalactic Medium with Fast Radio Bursts. *ApJ*, 797(1):71, December 2014.

[90] Bei Zhou, Xiang Li, Tao Wang, Yi-Zhong Fan, and Da-Ming Wei. Fast radio bursts as a cosmic probe? *Phys. Rev. D*, 89(10):107303, May 2014.

Vita

Mukul Bhattacharya was born in Bilaspur, Chhattisgarh, India on December 9, 1993. He grew up in Kharagpur, West Bengal and completed his school education from Kendriya Vidyalaya, IIT, Kharagpur in May 2011. He received Bachelor of Science degree with Physics as major and Maths as minor concentration from the Indian Institute of Science (IISc), Bangalore in May 2015. After graduating among the first batch of undergraduate students from IISc with first-class honours and distinction, he joined the graduate program in the Physics department at the University of Texas at Austin in August 2015. Since then, he has been working under the supervision of Pawan Kumar to understand the physics involved in high-energy astrophysical transient phenomena including fast radio bursts, gamma-ray bursts, and compact mergers of binary neutron stars/black holes.

Address: mukulbhattacharya1993@gmail.com

This dissertation was typeset with LaTeXby the author.